NATIONAL TECHNICAL UNIVERSITY OF ATHENS
SCHOOL OF NAVAL ARCHITECTURE AND MARINE ENGINEERING
DIVISION OF SHIP AND MARINE HYDRODYNAMICS

Effects of chordwise flexibility on

Flapping-foil thruster performance

Diploma Thesis

July 2017

Author : A.K. Priovolos
Supervisor : K.A. Belibassakis, Associate Professor, NTUA
Committee : G.K. Politis, Professor, NTUA
G. Triantafyllou, Professor, NTUA

Acknowledgements

The present Diploma Thesis is the last chapter of my studies at the School of Naval Architecture and Marine Engineering of National Technical University of Athens as an undergraduate student. Thus, I grab the chance to express my gratitude to the people who, in one way or another, assisted me in this effort.

First of all, I would like to thank my supervisor and mentor Associate Professor K. Belibassakis for his guidance and support and immeasurable patience during the preparation of this thesis. He was the best mentor someone could possible ever have. Also I would like to thank N. Lamprinidis for devising these wonderful sentences. I was also lucky to have E. Filippas whose knowledge of unsteady hydrodynamics and computational tools was of significant help indeed, and shaped this work in a large degree.

During these last years at NTUA I have met many people with whom I have shared many hours of discussion, information and knowledge. This list is in no way exhaustive, but notable entries are A. Charampopoulos, D. Iliopoulos, S. Konstantinidis, N. Lamprinidis , A. Lamprou, G. Politis, C. Sardelis (best PR guy ever).

I cannot in any way do *Muri* justice and compensate for her unconditional support and tolerance in times when I wasn't the most entertaining company she could afford to have. Finally, I want to thank all those friends who still haven't stopped being the *douchebags* they have always been. You know who you are.

Contents

Abstract

In this thesis a numerical model is devised to treat the problem of flapping foil propulors with chordwise flexibility. Recent research and development concerning flapping-wing propulsors has shown that such systems are able to achieve high levels of efficiency. Moreover, it has been demonstrated that chordwise flexibility further enhances their propulsive performance. Flapping foil biomimetic systems are also appropriate for other applications such as augmentation of ship overall propulsion by wave energy extraction and exploitation of wave and current renewable energy resources. In the present thesis a hydroelastic model based on a Discrete Vortex Method (DVM) for the hydrodynamics, in conjunction with Kirchhoff plate theory equation for the flexural deflection, is used to study the effect of chordwise flexibility on the performance of flapping hydrofoil. The foil response is actuated by harmonic heaving motion and pitching about its leading edge. As a first approximation we assume that the thickness and transverse deflections are small compared to the chord length. Numerical results are presented concerning the thrust coefficient and the efficiency of the system over a range of design and operation parameters, including Strouhal number, heaving and pitching amplitudes, and flexural rigidity, indicating that chordwise flexibility can improve propulsive efficiency. The present method can serve as a useful tool for assessment and the preliminary design and control of such biomimetic systems for marine propulsion.

Περίληψη

Στα πλαίσια αυτής της διπλωματικής εργασίας αναπτύσσεται μια μέθοδος επίλυσης του προβλήματος παλλόμενης υδροτομής με ικανότητα παραμόρφωσης υπό τις υδροδυναμικές πιέσεις κατά τη διάσταση της χορδής. Πρόσφατες έρευνες έχουν δείξει ότι προωστήρες που βασίζουν την αρχή λειτουργία τους σε παλλόμενα πτερύγια μπορούν να επιτύχουν μεγάλους βαθμούς απόδοσης. Η προσθήκη ευκαμψίας περαιτέρω βελτιώνει την απόδοσή τους. Βιομιμητικά συστήματα παλλόμενων πτερυγίων είναι επίσης κατάλληλα για εφαρμογές όπως η υποβοήθηση πρόωσης πλοίου μέσω απορρόφησης ενέργειας από το θαλάσσιο περιβάλλον και τα κύματα, καθώς κι απομάστευση ενέργειας ως ανανεώσιμη πηγή ενέργειας. Στην παρούσα εργασία αναλύεται ένα υδροελαστικό μοντέλο που βασίζεται στην μέθοδο

πεπερασμένων δινών (DVM) για την επίλυση του υδροδυναμικού προβλήματος, σε σύζευξη με τη θεωρία πλακών Kirchhoff για την επίλυση του προβλήματος της ελαστικής παραμόρφωσης της υδροτομής. Σκοπός είναι η διερεύνηση της επίδρασης της ελαστικότητας σε σύστημα παλλόμενων πτερυγίων. Η απόκριση της υδροτομής προκαλείται από αρμονική διέγερση σε κατακόρυφη κίνηση (heaving) και στροφή (pitching) περί το χείλος πρόσπτωσης. Σε πρώτη προσέγγιση υποθέτουμε ότι το πάχος της υδροτομής είναι αμελητέο, καθώς κι ότι οι ελαστικές παραμορφώσεις είναι μικρές. Αριθμητικά αποτελέσματα παρουσιάζονται για το συντελεστή ώσης και το βαθμό απόδοσης του συστήματος σε ένα εύρος παραμέτρων λειτουργίας και σχεδίασης, όπως αριθμός Strouhal, πλάτος κατακόρυφης κίνησης, πλάτος στροφής, καμπτική δυσκαμψία. Οι ενδείξεις είναι προς την πλευρά αυξημένου βαθμού απόδοσης λόγω της προστιθέμενης ευκαμψίας της υδροτομής. Το παρόν αριθμητικό μοντέλο μπορεί να επεκταθεί εύκολα ώστε να χρησιμοποιηθεί ως εργαλείο για σχεδιασμού κι ελέγχου βιομιμητικών συστημάτων σε εφαρμογές πρόωσης.

Chapter 1
Introduction to the Study of Flapping Foils

The current thesis begins with a historic review on the study of flapping foils as promising alternatives to conventional screw propellers as main propulsive devices, as well as their study as auxiliary thrusters. Our emphasis is of course on the study of chordwise flexibility in flapping foils, the study of which is the prominent goal of this work. However, for completeness purposes we will refer to other uses of flapping foils where attention has been given by researchers, such as manoeuvring.

The main motivation for the study of flapping foils as thrust – producing devices stems from the observation that it is in the heart of the very complex thrust mechanisms occurring in nature, both in aquatic and flying animals. The study of aquatic animals can be traced back to the time of Aristotle, who in his works considered their anatomy and locomotion (Sparenberg, 2002). However, the mechanics of swimming took many centuries until researchers began to systematically study them and make actual progress. In 1490, Leonardo Da Vinci attempted to explain and implement the mechanism of thrust generation by a flapping foil.

In the last decades of the 17^{th} century, the invention of the mercury barometer gave a boost to scientific research concerning fish locomotion. Later, the invention of film and photography allowed the recording of the fish movements, as well as pressure – measuring devices that had already been developed rendered the study easier.

According to biologists, aquatic animals can be split into three main categories based on the swimming mechanism they use to propel themselves (Lighthill, 1975); i) anguliform, where the thrust is produced by an undulatory motion throughout the whole animal body, which is largely flexible ii) carangiform, where the undulations are constrained to the posterior part of the body and iii) thunniform, where the undulation is confined at the relatively stiff caudal fin, performing flapping motion, a combination of heaving and pitching motion. The thunniform mode is the most efficient, according to Lighthill. Its efficiency has been demonstrated by the RoboTuna developed at MIT, which has achieved efficiencies up to 91% (Sfakiotakis et al, 1999).

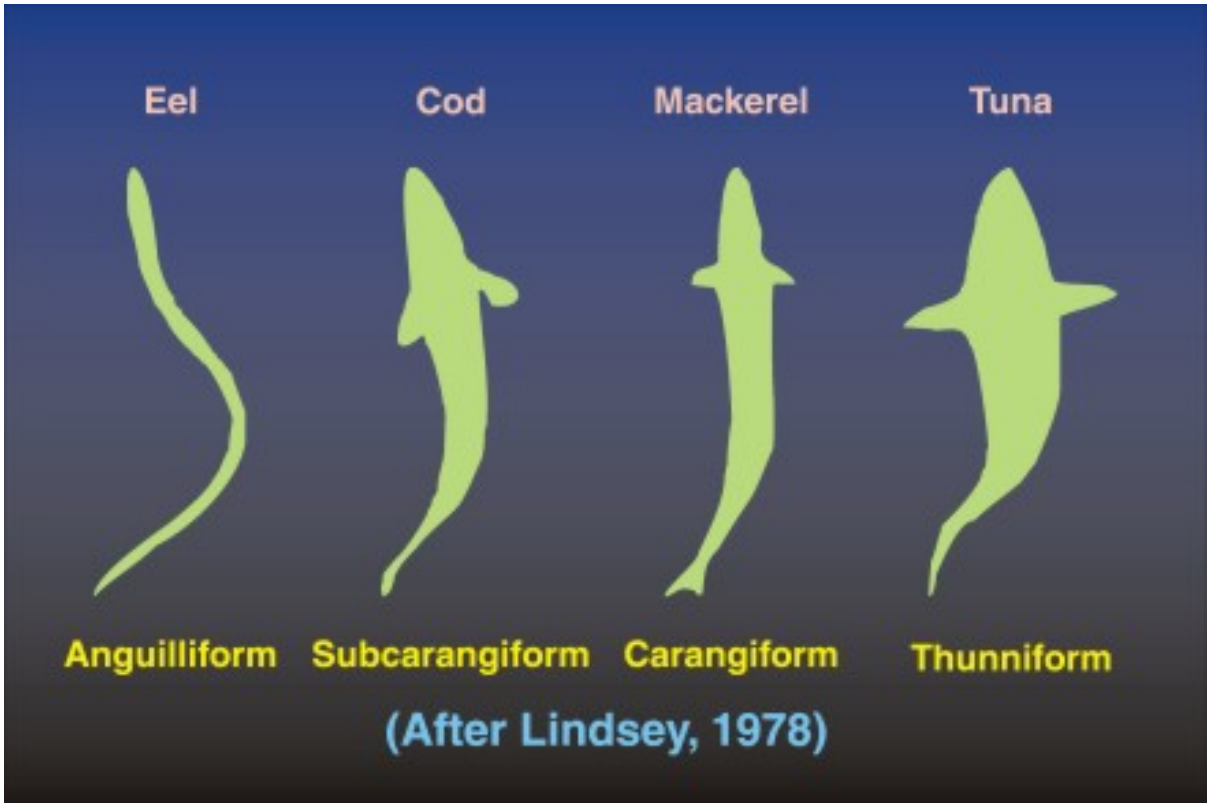

Figure 1.1: Swimming Modes (Lindsey, 1978)

The basic swimming mechanism is the transfer of momentum from the fish body to the fluid. The transfer mechanisms are lift, drag and acceleration reaction forces. The drag forces are a result of friction and pressure drag, a result of the body form. Most fast – cruising fish have evolved so as to have a body shape that largely eliminates this drag component. Finally, the fins on fish bodies form vortices when generating lift and/or thrust, a result that is predicted theoretically. This drag component largely depends on the fin shape.

The largest leap forward came in the beginning of the 20th century. This era saw the introduction of the fish locomotion study into the realm of fluid mechanics. Engineers were a significant help to zoologists in the field and their collaboration has been fruitful. Experiments were performed with dead fish or wooden models in order to measure drag and power needed to propel the specimen. This series of experiments revealed many of the mechanics of fish locomotion, most notably the famous Gray's paradox; it was found that the muscular power capacity of a dolphin is inadequate for the typical cruising speed observed in the species; the power needed to propel it was calculated to be seven times larger than that its muscles are able to produce. One of the most popular explanations of this peculiar fact is that

dolphins can extract energy from wavy, non – uniform flows (Rozhdestvensky & Ryzhov, 2003).

Before we further explore the studies conducted in the field of flapping foils, we present the main points that have been established after extensive research of swimming mechanisms in fish and cetaceans. In particular, the following points are explicitly stated (Rozhdestvensky & Ryzhov, 2003): i) Large Reynolds numbers of order 10^7 are interesting for technical applications. ii) The rear part performs simultaneous heaving and pitching motion, with phase shift close to π/2. iii) Strouhal number, defined as $St = fA/U$ is between 0.25 – 0.40, where A is the characteristic length travelled by the transverse motion of the fin (a foil, from a fluid mechanics point of view), $f = \omega/2\pi f$ is the motion frequency (in Hz) and U the cruising speed. Another important frequency parameter is the reduced frequency, usually defined as $k = \omega c/2U$. The latter is a non – dimensional parameter based on the time it takes for the system to travel its characteristic length (usually the chord length). iv) The mass and flexural rigidity of fins (foils) varies, both in the chordwise and the spanwise directions. v) Fins are also used for manoeuvring purposes, besides thrust production. vi) Aquatic animals can detect wave – induced flows and adjust their motion so that the take advantage of the energy associated with them. These observations have served as guidelines towards the study of flapping foils as biomimetic systems, the ultimate goal being the design of efficient propulsors and manoeuvring devices based on flapping foils.

The beginning of the 20th century marked the advance in theoretical aero – and hydro – dynamics which provided theories enabling the thorough analysis of the various swimming and flying mechanisms occurring in nature, facilitating also in the design of biomimetic thrust and manoeuvring devices. We note here that the first unsteady aerodynamic theories were developed due to the interest in aircraft flutter problems. (Bisplingshoff & Ashley, 1955) Of great importance are the theories developed concerning the flow past rigid 2D foils in oscillating (flapping) motion. In 1922 Prandtl formulated the problem of the unsteady motion of a wing in incompressible flow, noting that vortices have to be shed from the trailing edge. He theorized that the shed vortices carry momentum that is opposite to the foil motion, hence thrust is produced. Indeed, a characteristic property of flapping motion is that the vortices shed from the trailing edge (or caudal fin in aquatic animals) form a reverse Karman vortex sheet, resulting in a jet – like flow behind the wing (or tail). Theodorsen's thin airfoil theory was used by Garrick (1936) to calculate the thrust forces of a harmonically oscillating flat plate in incompressible flow. The Prandtl theory predicted that the shed vortices form a

trailing wake which has a geometry that is unknown a priori, due to the complex interactions of foil body and wake. Birnbaum (1924) assumed small amplitudes and confined the trailing wake to emanate from the trailing edge with the free – stream flow, enabling him to obtain results. The problem of flapping foils has also been studied by a number of Eastern European scientists, such as Keldysh, Lavrentiev, Khaskind and Nekrasov (Rozhdestvensky & Ryzhov, 2003).

The main categories of theoretical models attempting to explain the mechanisms of swimming are resistive and reactive models. Taylor (1951) developed a resistive theory suitable appropriate for the swimming of snakes and marine worms, where a bending wave is assumed to travel with constant speed along the animal's body. In this model, the inertia is neglected, and it is proven that this travelling bending wave leads to motion through the fluid. The largest part of theories developed, however, fall into the reactive theory. They assume large Reynolds numbers so that the thin boundary layer around the body is neglected and the inertial effects dominate over the viscous. Probably the most ground-breaking theory is that of the «elongated body» developed by Lighthill (1960). It allows the calculation of the thrust produced by anguilliform and carangiform swimmers by basic momentum considerations.
After Lighthill the field of theoretical treatments of swimming experienced a large boost. Wu (1961, 1971) studied the hydromechanics of swimming propulsion assuming a 2D flat plate with a prescribed lateral motion wave travelling in the chordwise direction. He also studied the feasibility of energy extraction from waves, the answer to which was affirmative for non – uniform flows.

After those seminal works, the study of the unsteady hydrodynamics and aerodynamics intensified, both for oscillating fins and artificial flapping foils. For clarity purposes, the following references will be presented in two separate categories; experimental and numerical (potential flow and CFD) studies. First we will present the work done on rigid foils and we will conclude with the work done on flexible foils, which is the main direction of the present work.

1.1 Studies of Rigid Flapping Foils

1.1.1 Experimental Works

An important aspect of flapping foil motion is the trailing wake formation behind the oscillating foil that produces the jet flow with momentum with the opposite direction of the foil's motion. Koochesfahani (1989) studied the vortical patterns in the wake of an oscillating foil. It was concluded that the amplitude, frequency and waveform of the oscillating greatly affected the structure of the airfoil's wake, enabling vortex – vortex interactions that directly affect the thrust producing capabilities of the airfoil. Triantafyllou and Triantafyllou (1991) studied the wake formation behind an oscillating foil created by the shed vorticity owing to the flow unsteadiness. They concluded that the wake dynamics play a dominant role, thus the Strouhal number is the most important parameter and that optimal thrust production occurs at Strouhal numbers in the range 0.25 – 0.35 that correspond to maximum wake spatial amplification. The latter observation can be interpreted as maximization of the jet flow channel width that is caused by the reverse Karman vortex sheet. Gopalkrishnan et al (1994) studied a foil behind a cylinder's wake. It was found that for specific parametric values interaction patterns emerged between the cylinder and foil – shed vortices, adjusting accordingly the wake to either a regular or reverse Karman vortex sheet.

Extensive experimental studies on rigid flapping foils have been performed by Triantafyllou and collaborators at MIT. Anderson et al (1998) performed systematic runs over a range of Strouhal numbers and motion amplitudes and established high efficiencies, up to 87%, associated with optimal wake formations. The corresponding angles of attack were moderately large, while the formed leading edge vortices were kept mild. DPIV measurements revealed the complex interactions between leading edge and trailing edge shed vortices. Read et al (2003) studied a flapping foil pitching around 1/3 of its chord length, with AR = 6. Endplates were used at the tips suppressing 3D flow effects and increasing the effective aspect ratio. In the experiments normalized heaving amplitude (with respect to the chord length) ranging from 0.75 and 1 are used. Under specific conditions, corresponding to optimal wake formation, good rates of efficiency were observed, reaching 71.5%. More important is the fact that large areas of high efficiency coincided with satisfactory levels of thrust, indicating the possible exploitation in flapping foils as biomimetic propulsive devices.

They reported that high values of efficiency were associated with effective angles of attack of the order of 15^o – 25^o. They reported high levels of achievable efficiency, of order 80%. These values of the geometric angle of attack are considerably larger than the angle of attack that leading edge flow separation occurs in steady flows around hydrofoils, indicating that partial separation and dynamic stall phenomena under certain flapping motion parameters does not lead to thrust breakdown; see, e.g., Belibassakis et al (1997) and Politis & Belibassakis (1999).

Moreover, very large angles of attack lead to decreased thrust attributes, as was the case for very small values, too. The effects of phase difference between oscillatory motions were also investigated, concluding in the fact that optimal thrust production is usually associated with phase difference close to $\pi/2$, which is observed in hydrobionts. Furthermore, Read et al (2003) report that higher – order harmonics added to the heaving motion profile were able to alleviate the negative effects of multi – peaked effective angle of attack profiles and improve thrust production. Hover et al (2003) studied the different effective angle of attack profiles that come up in flapping foil motion, due to the non – linear effects associated with increased flapping frequency corresponding to higher Strouhal numbers, even for purely geometric quantities such as the effective angle of attack. They concluded that sawtooth profiles, with multiple peaks in a flapping period, leads to increased thrust, while the more rounded profiles lead to better efficiency. Schouveiler et al (2005) studied a flapping foil, adding a bias angle to the pitching motion. This mechanism is able to produce both thrust and non – zero mean lift, rendering it appropriate for manoeuvring purposes.

There are many more aspects of flapping foil motion that have been considered by experimental studies. The formation of leading edge vortices shed to the surrounding flow has been studied by Dickinson (1994), Maxworthy (1979), Ellington (1984), Gursul & Ho (1992). Those studies are mainly concerned with insects' flying. Delayed stall and significant lift forces have been attributed to the formation of leading edge vortices. It is noted however that large leading edge vortices increase drag and reduce the efficiency of the flapping foil as a thrust – producing device.

1.1.2 Inviscid (potential theory) models

Potential theory of incompressible fluid has been extensively used to simulate the unsteady flow around flapping foils. The advances in computer science in conjunction with

high – speed computers allowed for numerical BEM simulations overcoming restrictions imposed by previous analytic models (e.g. small oscillation amplitudes). Bose (1992) used a potential flow BEM for the calculation of the dynamic response of a flapping foil. The results agreed well with analytic theory in the case of small amplitudes. In the latter work chordwise flexibility has been included in the study, although it was not considered as a result of the fluid – structure interaction, but rather as a prescribed deformation, analogous to earlier research by Wu (1961, 1971). Bose & Yamaguchi (1994) continued the previous investigation, with application to the propulsion of a 200,000ton DWT tanker ship with a flapping foil with prescribed deformation added to its rear (trailing edge) part. It was found that the efficiency of the examined flapping thruster was 5% higher than that of a conventional propeller with the same thrust output.

La Mantia & Dabnichki (2009) have devised a code to treat the problem of flapping foils and throughout the last decade have studied several aspects of the problem, such as the thickness effect on thrust (Mantia & Dabnichki 2010), the effect of the wake model (Mantia & Dabnichki 2010) and the added mass effect (Mantia & Dabnichki 2012).

In order to investigate 3D effects, Belibassakis et al (1997) applied the Vortex Lattice Method to study the thrust producing capabilities of a pair of oscillating wings and compared against against experimental data by Triantafyllou et al (1993).

Politis & Tsarsitalidis (2009) simulated the unsteady flow around 3D flapping wings using a BEM time stepping algorithm; see also Politis (2011). They performed systematic simulations of fish –like foils possessing skewback angles equal to 25^o and 45^o and established the high efficiency associated with them. They validated the fact that the reverse Karman vortex sheet is the main mechanism of thrust production by displaying the vortex patterns of the trailing wake. They also tested a 2 – foil configuration, where two wings are placed one on top of the other and perform flapping motion with phase shift equal to π.

Pan et al (2012) used a potential BEM in conjunction with heuristic pressure arguments to predict the performance of flapping foils in the case where significant vortices are shed near the leading edge, as well as from the trailing edge. The results of their method were compared with the experimental of Read et al (2003) and the agreement was very good, indicating the significance of leading edge separation for flapping foils.

Turning into more specific applications in the context of ship hydrodynamics, Belibassakis & Politis (2013) studied the performance of flapping foils beneath a ship's hull as thrust augmentation devices, absorbing energy by the heaving and pitching motion of the

ship in waves. In this case the heaving foil motion is offered by the ship responses in waves while the pitching motion is enforced. An active pitch control strategy was proposed that attempts to restrain the phase difference between heaving and pitching motions in the vicinity of $\pi/2$, where it has been repeatedly recorded to lead to increased efficiency. They considered both horizontally and vertically placed wings towards the fore of the ship. Apart from the thrust production, the placement of wings beneath the ship's hull was able to substantially reduce the ship's responses in heaving, pitching, swaying and rolling.

Filippas & Belibassakis (2014) used a BEM code to simulate the flow around a flapping foil that operates beneath the free surface in the presence of waves. It was found that the thrust of such an arrangement could be increased by 20% compared to the thrust obtained in an infinite domain, under proper selection of the parameters involved. Results have been extended to incident wave spectra by Belibassakis & Filippas (2015).

Politis & Tsarsitalidis (2014) have presented a design methodology for flapping wings as ship propulsors. They developed a systematic series based on 3D unsteady BEM. In total, they produced results in the form of open water performance charts for a wing with zero skewback and a NACA 0012 foil section for 24 geometric and motion configurations. They considered the cases of three ships and compared the efficiency of a flapping – wing based propulsor against conventional propellers. In all three cases it was found that the flapping wing leads to reduced shaft horsepower.

1.1.3 CFD Studies of Flapping Wings

The problem of flapping foils has been tackled with CFD methods using Navier – Stokes equations for the flow around the oscillating body. Viscous effects that cannot be captured by potential-flow methods are simulated by CFD methods, shedding further aspects of the complicated unsteady flows into light, and a brief review is presented below.

Videv et al (1993) used 2D RANSE solver to study the flapping motion of a symmetric foil. They reported that heaving motion, although able to achieve relatively high levels of thrust, does so at very low efficiency values, rendering it virtually useless for propulsion applications. The basic flow features were found to depend mainly on the motion parameters instead of the foil geometry. An important point of their work was that slight alterations in the motion parameters could lead to large efficiency losses.

Tuncer & Platzer (1999) used a Navier – Stokes solver with the incorporation of particle traces. They tested a flapping foil at moderate heaving amplitudes (of order 1) and varied the pitching amplitude and reduced frequency. They observed that increased efficiencies were associated with attached flow, which occurred at even large angles of attack.

Zhang & Zhou (2010) performed numerical investigation of a heaving 2D airfoil at $Re = 10^4$ varying the time the foil motion spends at the upstroke and the downstroke. They found that non – symmetry of heaving can lead to interaction between leading and trailing edge vortices that increase both thrust and efficiency.

1.2 Studies of Chordwise Flexible Foils

We proceed to the introduction of the main body of the present work, which is the study of the chordwise flexibility addition in flapping foils. Flexibility has long been established as a main feature of aquatic animals' propulsion mechanisms, either when it is active (controlled by the animal with pressure variations as feedback) or passive (induced by surrounding fluid pressure and inertial effects).

The coupled system of a flapping foil that passively deforms is analysed in this work. The bibliography of this field is far more limited than this of rigid foils performing unsteady motions, although experiments and some numerical methods that couple the flow with the flexible dynamics have revealed some of the aspects of propulsion devices possessing chordwise flexibility.

1.2.1 Experimental Studies

Experimental studies in the field are relatively recent. They usually consist of a flat plate made of a flexible material (e.g. PDMS) that is subject to heaving or pitching, sometimes considering only one of those oscillatory motions.

Heathcote et al (2004) studied the thrust – producing capabilities of a flapping foil with a thin flat plate attached to it downstream in $Re = 0$ (i.e. no free – stream velocity

present). They observed that some degree of chordwise flexibility improved the thrust for heaving motion. Extreme flexibility was able to outperform the flexible and absolutely rigid foils only for very low Strouhal numbers. Heathcote et al (2007) went on to study the thrust capabilities in low Reynolds numbers. They reported both thrust and efficiency increase for certain degrees of flexibility. Finally, Heathcote et al (2008) studied the effect of spanwise flexibility on flapping wing propulsion. They found that a degree of spanwise flexibility increases both thrust and propulsive efficiency. Increased spanwise flexibility was shown to significantly deteriorate the hydrodynamic aspects of the wing, leading to reduced thrust – producing capability.

Alben et al (2012) studied the self – propulsion of freely swimming thin flexible foils. They established the power laws associating the swimming speed with the bending rigidity and the foil length. It is consistently reported that the swimming speed displays peaks as the above parameters are varied.

Barranyk et al (2012) performed experiments with flat plates in flapping motion of varying rigid to flexible ratio and reported that increasing flexibility increased both thrust and efficiency in the parameter range tested. They also studied the effect of depth of submergence, and found that the hydrodynamic aspects of the foil improved when it was placed in proximity to the channel bottom.

Prempraneerach et al (2013) performed experiments with chordwise flexible flapping foils in towing tanks. Propulsive efficiencies as high as 87%, up to 36% higher than those of rigid foils were recorded.

Dewey et al (2013) considered chordwise flexible wings in pitching motion and achieved improvements in both thrust and efficiency of the order 100%. The peaks observed in efficiency were associated with the simultaneous satisfaction of the Strouhal number lying in the optimal range ($0.25 < St < 0.35$) (Triantafyllou et al, 1993) and the forcing motion frequency is tuned to a structural resonant frequency of the system of foil and surrounding fluid. Moreover, scaling laws were proposed for the thrust force and propulsive efficiency based on characteristic elastic forces, instead of characteristic fluid forces often used in the study of rigid flapping – wing propulsors, which seem to correctly collapse their experimentally acquired data.

Quinn et al (2014) considered chordwise flexible panels in heaving motion, as opposed to Dewey et al (2013). They reported that although the thrust produced is mainly a function of Strouhal number, local peaks were found associated with the structural resonance

of the panels. Their results are reported to scale with characteristic parameters derived from the Euler-Bernoulli beam equation. Conditions of zero-net thrust were considered, corresponding to freely swimming panels. It is shown that increased flexibility and reduced swimming speeds correspond to higher efficiency under these conditions.

Cleaver et al (2014) considered rigid heaving 0012 NACA section foils with a flexible flat plate attached downstream to the foil, with its length varying from 10% to 30% of the foil's chord length. Their aim was to study the effect of chordwise flexibility to the drag reduction associated with heaving motion in uniform flow. The added flexibility provided improvements up to 20% higher compared to the rigid foil.

Paraz et al (2015) experimentally studied the response of a flexible heaving foil in harmonic forcing in a uniform flow. The effects of motion amplitude, Reynolds number and flexural rigidity were studied by systematically varying the corresponding values. It was revealed that the response of the panel was non – linear with respect to the forcing amplitude. Scaling the obtained results with the first resonant frequency of the foil in the surrounding fluid, the results collapsed well. The only parameter that greatly affected the plate's response was that of the forcing amplitude, indicating that the response is non-linear with respect to the heaving motion amplitude.

Quinn et al (2015) used experimental gradient – based optimization to maximize the efficiency of a flexible panel actuated at its leading edge by both heaving and pitching motions. They concluded that optimality is achieved when the following conditions are simultaneously met: i) The Strouhal number lies in the range 0.26 – 0.33 for flapping motion, so that both the wake vortex sheet is packed and coherent and the flow does not separate when passing over peaks and troughs of the oscillating panel ii) The flexural rigidity of the panel is chosen such that the motion frequency corresponds to a resonant frequency of the fluid & panel system iii) The heaving amplitude is as high as possible, as long as the boundary layer stays attached along the panel body iv) The maximum angle of attack is minimum, so that leading edge separation is suppressed v) The phase lag between heaving and pitching lies near 90deg.

Richards & Oshkai (2015) studied the thrust capability and efficiency associated with flexible flapping foils by also varying their inertia and stiffness characteristics. They report that optimum propulsion is achieved when the frequency of the oscillation is tuned to a resonant frequency of the fluid & foil coupled system and is a result of both increased trailing edge amplitude (increasing the effective swept area) and of beneficiary phase difference

between leading edge and trailing edge, corresponding to about 90deg. trailing edge lag. The combination of heaving and pitching is found to lead to increased thrust although reducing thrust compared to the heaving – only case.

1.2.2 Inviscid (potential theory) models

The first (to our knowledge) theoretical work attempting to couple the potential flow around a thin foil with its passive elastic deformation due to added chordwise flexibility is that of Katz & Weihs (1978). Using the velocity potential and assuming a massless foil, they obtained results for the thrust force and efficiency associated with flapping configurations. They predicted that flexibility increases efficiency and reduces thrust capability. This is attributed to the fact that the passive deformation aligns the foil with the incoming flow, thus reducing the lift force produced, however its orientation is nearer the direction of advance, thus increasing efficiency.

Zhu (2007) used BEM fully coupled with thin – plate theory to simulate the flow around a 3D wing with both chordwise and spanwise flexibility. Attention was given to two separate cases: low density fluid (e.g. air) and high density fluid (e.g. water). It was found that the response of the wing in the first case is mainly inertial, while in the second case it is dominantly fluid – driven. In the inertia – driven response, the wing response causes its effective angle of attack to rise, thus deteriorating performance. On the other hand, fluid – driven response causes the feathering of the foil, aligning it with the flow in such a way that while the thrust reduces, the efficiency is increased.

The efforts to tackle the problem have substantially increased in number in recent years. Alben (2008) proposed a potential flow theory coupled with a massless and inextensible elastic sheet formulation to tackle the problem of flexible thin 2D panels pitching around their leading edge. The thrust displayed peaks as the non-dimensional rigidity was varied, corresponding to resonant frequencies of the coupled system, while the efficiency dropped smoothly from unity in the limit of zero rigidity to the value predicted by potential flow theory for rigid oscillating foils. The optimum rigidity for thrust production decreased as the pitching frequency increased.

Michelin & Smith (2009) considered the potential flow around heaving flexible foils and assumed inextensibility of the panel under its passive deformation due to the hydrodynamic pressures formed around it. They reported peaks in both the thrust and

efficiency when the flexural rigidity was varied, corresponding to resonance frequencies of the system. The efficiency compared to the rigid case was found to be even three times larger under optimal conditions. The increased thrust and propulsive capabilities that occurred with chordwise flexibility addition were associated with amplification of the reverse Karman vortex street formed downstream of the foil.

Paraz et al (2016), following the experimental results of Paraz et al (2015), developed an analytical model based on Euler – Bernoulli beam theory to study the effect of chordwise flexibility in heaving flexible plates. Peaks in thrust were associated with both peaks in trailing edge amplitude and its phase difference with respect to the leading edge excitation, occurring in the region of the coupled system resonance. The trailing edge response was found to decrease with increasing the heaving amplitude in Paraz et al (2015), an effect that is captured by the analytical model developed.

Kancharala & Philen (2016) performed numerical simulations based on 2D BEM coupled with non – linear Euler Bernoulli beam theory and performed an optimization procedure to determine the optimal chordwise stiffness profiles in flapping foil motion of self – propelled fins. The stiffness profiles that lead to minimum cost of transport are consistently characterized by abruptly reduced stiffness in the vicinity of the trailing edge, as observed in hydrobionts.

1.2.3 CFD Studies of Flexible Flapping Wings

The literature in the treatment of flexible flapping foils with CFD solvers is more limited than the inviscid methods'. In addition, most works in this area are concerned with animal flight, which is not the main object of interest in the present work. However, we shall present some works in this field.

Connel (2006) submitted a PhD thesis concerned with the interaction of a flexible panel in flapping motion with the ambient flow. The research consists of the coupling of a Navier – Stokes solver with geometrically non – linear thin –body structural solver. Stability issues are thoroughly discussed.

Luo et al (2010) developed a high – fidelity 3D numerical method to treat the problem of the flow – structure interaction in flapping flight. Their hydrodynamics solver consists of a Navier – Stokes solver based on immersed boundary method, while their structural solver is a

non – linear FEM. They used the proposed method to simulate the flow around the wing of a dragonfly, revealing the various aspects of the complicated phenomenon.

De Sousa & Allen (2011) considered a flat plate clamped on its leading edge, performing forced pitching oscillations. They used a numerical scheme to solve the Navier – Stokes for the hydrodynamics part and coupled it with a finite difference structural dynamic solver. They concluded that flexibility leads to efficiency increase, which is further improved by increasing the structural mass.

In this work, the case of a 2D flapping foil with chordwise flexibility is considered. Our point of interest is the thrust – production capability and efficiency of such a system, compared to the rigid flapping foil case. More specifically, in Chapter 2 we present in detail the inviscid Discrete Vortex Method (DVM) for the solution of the flow around the body, which is assumed to be of small thickness compared to its chord length, and of infinite span such that spanwise flow effects can be ignores. In Chapter 3 extensive simulations are conducted to validate the DVM and present the basic aspects of flapping foils. In Chapter 4 the DVM is coupled with a thin plate dynamic structural solver based in Kirchhoff plate theory and the effect of chordwise flexibility is investigated. Finally, in Chapter 5 conclusions are drawn and suggestions for further work are made. Details of the structural solver are thoroughly presented in the Appendix.

Chapter 2: Discrete Vortex Method for the Unsteady Flapping Foil Problem

In this Chapter the unsteady lifting-flow problem of a flapping foil is presented, and its numerical solution obtained by the discrete vortex method (DVM, Katz & Plotkin, 1991). Details concerning the latter numerical method are also provided, as well as its application to similar problems of unsteady hydrofoil theory.

2.1 Basic Nomenclature

We consider a foil, corresponding to symmetric wing of infinite span, travelling at a constant velocity and experiencing heaving and pitching motions. a sketch of the geometry is shown in Fig. 2.1. The thickness of the wing is assumed to be small compared to its chord length. The surrounding fluid is assumed to be inviscid, and the resulting unsteady flow is irrotational. These assumptions make the use of unsteady 2D thin foil theory acceptable.

The domain considered is $D \subseteq I\!R^2$, with boundary $\partial D = \partial D_B \cup \partial D_W$, which is considered to be smooth everywhere except the trailing edge. The boundary represents the foil's surface ∂D_B and the resulting trailing wake ∂D_W which ensures the conservation of circulation in the fluid domain, according to Kelvin's theorem. The trailing wake is a product of the flow unsteadiness. It is noted here that the boundaries $\partial D_B, \partial D_W$ are actually time – dependent; it holds that $\partial D_B = \partial D_B(t), \partial D_W = \partial D_W(t)$. Generally, in the sequel the time dependency will be omitted when the time instant that we refer to is obvious.

The problem of a foil travelling with a constant speed $-\mathbf{V}_\infty$ (the minus sign stresses the fact that it travels towards negative values of the horizontal axis) is treated by considering the equivalent problem of a foil with zero speed subject to a free – stream velocity $\mathbf{V}_\infty$. With this in mind, we consider two reference frames; one fixed at the foil's mean position and hence is inertial, and one that is body – fixed, i.e. fixed on the foil's leading edge and having

an inclination relative to the horizontal axis equal to the foil's pitch angle. The corresponding reference frames are denoted x, y (inertial) and x', y' (body – fixed).

The flow consists of two main components; a steady parallel flow $\mathbf{V}_\infty$ due to the constant travelling speed of the foil and an unsteady flow which, according to the assumptions stated above, is modelled by a scalar potential $\Phi(x, y, t)$. The unsteady velocities in the flow field are then given by $\nabla\Phi(x, y, t)$.

It is possible to include a rotational background unsteady flow component such as a velocity gust denoted by $\mathbf{V}_G$, provided that the vorticity contents are small.

Due to the unsteadiness of the flow around the foil, a trailing wake is formed downstream. Also, due to the generation of lifting flow and circulation around the foil an appropriate Kutta condition is satisfied at the trailing edge. The positions of point $A \in \partial D_B$ is defined by $\mathbf{r}(s;t)=[x(s;t), y(s;t)]^{\mathrm{T}}$ and their velocity in the inertia reference frame are given by $\mathbf{V}_\mathbf{A}(s, t) = \partial_t \mathbf{r}(s;t)$, where s is a curvilinear coordinate on the body's surface.

Although initially we consider simple symmetric wings, more general camber geometries can also be included, defined by $\eta(x', t)$ on the body – fixed reference frame. This extra consideration is made so that in the course of this work we will attempt to couple the hydrodynamic formulation developed in the chapter with the foil's deflection thanks to its chordwise flexibility.

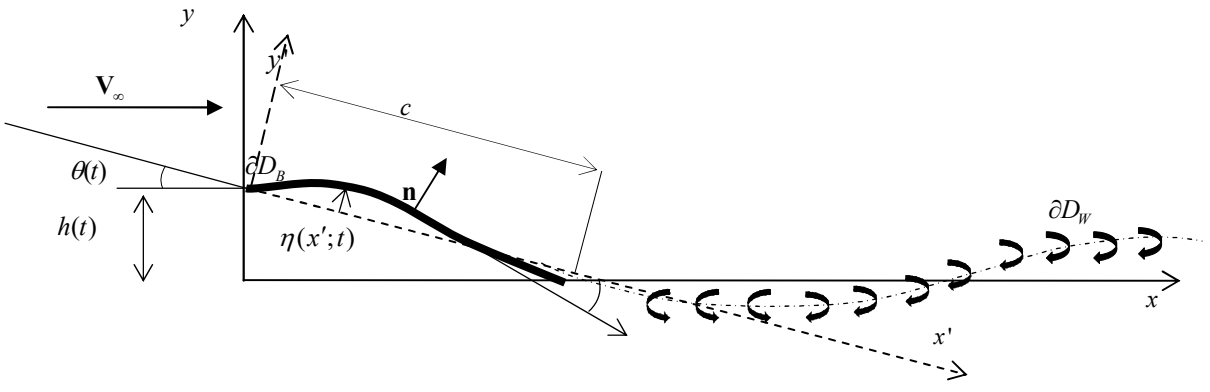

Figure 2.1: Foil and motion parameters sketch. The moving inertial and body fixed frames are denoted by x, y (solid lines) and x', y' (dashed lines), respectively. The trailing wake is drawn in dash – dot line and wake point vortices are denoted by curved arrows.

The field equation that the flow potential must satisfy is Laplace's equation

$$\nabla^2\Phi(x,y,t)=0, \tag{2.1}$$

i.e. the equation of mass conservation (under the irrotationality assumption of the disturbance flow component). On the solid body's surface ∂D_B the no-entrance Neumann condition must hold

$$\nabla\Phi\cdot\mathbf{n}=(\mathbf{V_A}-\mathbf{V}_\infty-\mathbf{V_G})\cdot\mathbf{n}, \tag{2.2}$$

where **n** denotes the unit normal vector on the body's surface.

The problem formulation is completed with the addition of a relation analogous to (2.2) which describes the physical constraints of the trailing wake. This additional information is inserted via the Kutta condition, which is discussed further in this chapter.

2.1 Solution of the lifting problem around the foil

The flow around the foil is solved by the representation theorem the potential at every point in the domain D can be expressed as a function of the potential values of its boundary ∂D. The potential is expressed by vorticity distributions $\gamma_B(s;t)$ and $\gamma_W(s;t)$ in the body and trailing wake surface, respectively. These vorticity distributions are defined by the relations

$$\gamma(\mathrm{s;t})=u_U(\mathrm{s;t})-u_L(s;t)=\nabla(\varphi_U-\varphi_L)\cdot\boldsymbol{\tau}=\nabla[\![\varphi]\!]\cdot\boldsymbol{\tau}, \tag{2.1.1}$$

where $u(s;t)$ u denotes the tangential perturbation velocity and $\boldsymbol{\tau}$ denotes the unit tangent vector on the surfaces ∂D_B, ∂D_W. The subscripts L, U denote the lower and upper sides of the surfaces, respectively. The potential values on the surfaces are denoted by

$$\varphi\big(x(s),y(s);t\big)=\varphi\big(\mathbf{r},t\big), \tag{2.1.2}$$

to stress the fact that they actually correspond to traces of the potential. The $[\![\cdot]\!]$ operator denotes the difference of quantities between the upper and lower side of the surfaces and will be used extensively in the course of this work. Since the body is assumed to have zero thickness no source distributions are considered. By default, Eq. (2.1.1) implies

$$\int_{\partial D_B} \gamma_B(s;t)ds = \Gamma(t) = [\![\Phi]\!]_{TE}, \tag{2.1.3}$$

that is, the integral of the bound vorticity is equal to the circulation around the foil, equivalent with the potential difference at the trailing edge.

The value of the potential gradient $\nabla\Phi$ when the potential satisfies Laplace's equation can be directly represented by its values on the boundaries $\partial D = \partial D_B \cup \partial D_W$. Applying the representation theorem in the 2D case we have

$$\begin{aligned}\nabla\Phi(s;t) = &-\frac{1}{2\pi}\int_{\partial D_B}\frac{\gamma_B(\xi;t)}{\left|\mathbf{r}(\xi\,|\,\mathrm{s};\mathrm{t})\right|^2}\left\{\mathbf{k}\times\mathbf{r}(\xi\,|\,s;t)\right\}d\xi + \\ &-\frac{1}{2\pi}\int_{\partial D_W}\frac{\gamma_W(\xi;t)}{\left|\mathbf{r}(\xi\,|\,\mathrm{s};\mathrm{t})\right|^2}\left\{\mathbf{k}\times\mathbf{r}(\xi\,|\,s;t)\right\}d\xi,\end{aligned} \tag{2.1.4}$$

where **k** denotes the unit vector normal to the x – y plane, according to the right – hand rule, and **r**($\xi|s;t$) denotes relative distance of points on the surface ∂D. In particular **r**($s;t$) is the point where the no – entrance boundary condition is applied and **r**($\xi;t$) denotes the integration points on the vorticity surface. Replacing the LHS of Eq.(2.1.4) from Eq. (2.2) we have

$$\begin{aligned}\left(\mathbf{V_A}-\mathbf{V}_\infty-\mathbf{V_G}\right)\cdot\mathbf{n} = &-\frac{\mathbf{n}}{2\pi}\int_{\partial D_B}\frac{\gamma_B(\xi;t)}{\left|\mathbf{r}(\xi\,|\,\mathrm{s};\mathrm{t})\right|^2}\left\{\mathbf{k}\times\mathbf{r}(\xi\,|\,s;t)\right\}d\xi + \\ &-\frac{\mathbf{n}}{2\pi}\int_{\partial D_W}\frac{\gamma_W(\xi;t)}{\left|\mathbf{r}(\xi\,|\,\mathrm{s};\mathrm{t})\right|^2}\left\{\mathbf{k}\times\mathbf{r}(\xi\,|\,s;t)\right\}d\xi.\end{aligned} \tag{2.1.5}$$

Eq. (2.1.5) is the integral equation to be solved for the distribution of the bound vorticity $\gamma_B(s;t), \mathbf{r}(s,t)\in\partial D_B$. The solution is obtained numerically via a discretization scheme, including a wake model for the trailing wake vorticity described below.

2.2 Kutta Condition – Trailing wake model

The unsteadiness of the flow creates a trailing vortex wake behind the foil, as has already been stated. Vorticity is continuously shed from the trailing edge and its strength is connected with the rate of change in of circulation around the foil, as obtained from application of Kelvin's theorem concerning the conservation of circulation around closed material circuits.

.

In this work a wake model is used for the trailing vortex sheet and its geometry is given by the trajectory of the trailing edge of the foil. This assumption corresponds to a prescribed wake geometry which simplifies the problem. The vorticity in the trailing wake is associated with the vorticity at the trailing edge using results from the analytic theory (e.g. Newman 1977). Assuming small perturbations so that the foil's geometry always coincides with a cut on the x – axis (coinciding with the interval $[0, c]$, where c is the chord length), we try to establish the evolution of the vortex wake in time and space. From linear theory, the pressure difference on the vortex wake can be calculated from the Bernoulli's equation

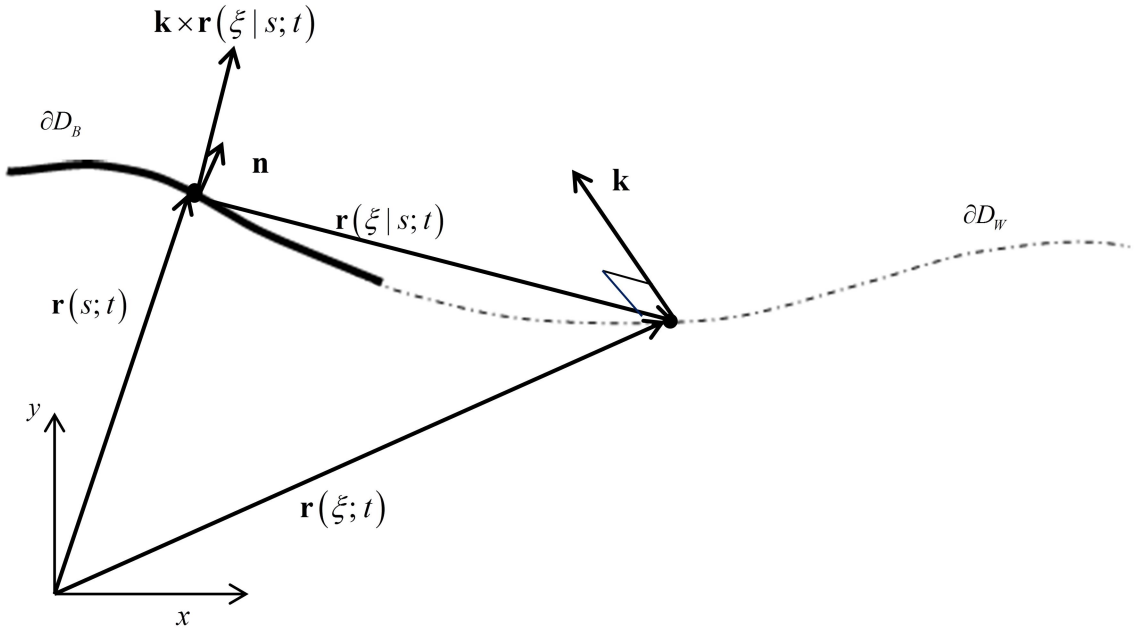

Figure 2.2: Relative positions of control point on body surface and integration points, here shown in the wake surface for clarity

$$\left[\!\left[p\left(x;t\right)\right]\!\right]_{\partial D_W} = \rho \frac{\partial \left[\!\left[\Phi\left(x;t\right)\right]\!\right]_{\partial D_W}}{\partial t} + \rho U \gamma_W (x;t),\ \ x > c, \tag{2.2.1}$$

where $U = \left|\mathbf{V}_\infty\right|$. The potential difference $\left[\!\left[\Phi\right]\!\right]$ on the wake surface is, extending (2.1.3) to apply for the trailing wake

$$\left[\!\left[\Phi\left(x;t\right)\right]\!\right]_{\partial D_W} = \int\limits_{\partial D_B} \gamma_B\left(\xi;t\right) d\xi + \int\limits_{c}^{x} \gamma_W\left(\sigma;t\right) d\sigma. \tag{2.2.2}$$

Using Eq. (2.2.2) Bernoulli's equation (2.2.1) becomes

$$\left[\!\left[p\left(x;t\right)\right]\!\right]_{\partial D_W} = \rho \frac{\partial}{\partial t}\left(\Gamma(t) + \int\limits_{c}^{x} \gamma_W\left(\sigma;t\right) d\sigma \right) + \rho U \gamma_W (x;t). \tag{2.2.3}$$

Applying a pressure – type Kutta condition at the trailing edge demanding that the pressure difference between the foil's surface sides becomes zero is straightforward. Actually, by setting $x = c$ in (2.2.3) we have

$$\rho U \gamma_W (c;t) + \rho \frac{\partial \Gamma(t)}{\partial t} = 0 \ \Rightarrow\ \gamma_W (c;t) = -\frac{1}{U}\frac{d\Gamma(t)}{dt}. \tag{2.2.4}$$

Eq. (2.2.4) relates the vorticity at the trailing edge with the rate of circulation change around the foil. The kinematic boundary condition of the vortex wake requires that the pressure difference between the upper and lower sides of the wake boundary be equal to zero for $x > c$. Since we have established that the pressure difference is zero at the trailing edge, this means that

$$\partial_x \left[\!\left[p(x;t)\right]\!\right] = 0,\ \ x > c \tag{2.2.5}$$

Differentiating the Bernoulli equation (2.2.3) with respect to x and applying Eq.(2.2.5) we obtain

$$\rho U \frac{\partial \gamma_W(x;t)}{\partial x} + \rho \frac{\partial}{\partial x}\left(\frac{\partial \Gamma(t)}{\partial t} + \frac{\partial}{\partial t}\int_c^x \gamma_W(\sigma;t)d\sigma \right) = 0 \tag{2.2.6}$$

By virtue of Eq.(2.2.4) and differentiating under the integral sign, we have

$$\rho U \frac{\partial \gamma_W(x;t)}{\partial x} + \rho \frac{\partial \gamma_W(x;t)}{\partial t} = 0 \Rightarrow \frac{\partial \gamma_W(x;t)}{\partial t} + U \frac{\partial \gamma_W(x;t)}{\partial x} = 0. \tag{2.2.7}$$

The solution to this homogenous partial differential equation is

$$\gamma_W(x;t) = \gamma_W(x - Ut), \tag{2.2.8}$$

corresponding to a wave – like function. This equation implies that the vorticity is convected downstream with the free – stream velocity, which is an approximate result that complies with Kelvin's theorem. Hence, the vorticity at $x>c$ in time t is the same as the vorticity at the trailing edge in time $t - t_{TE} = t - U^{-1}(x - c), x > c$. This allows the calculation of the vortex wake vorticity from the derivative of the circulation around the foil at each time step, calculated by means of the DVM. Formally,

$$\gamma_W(x;t) = \gamma_W(c; t - t_{TE}). \tag{2.2.9}$$

The above equation, in conjunction with the simplified wake model, describes the trailing wake vorticity effects. In particular, the RHS term of Eq.(2.2.9) is known from Eq. (2.2.4), as obtained from the solution of the lifting problem around the foil, wherefrom the bound vorticity distribution $\gamma_B(s; t - t_{TE})$ is calculated at each time step.

The analysis thus far is exact for the linearized case, where the foil's unsteady motion amplitudes are considered small (with respect to the chord concerning heave motion and small with respect to unity concerning pitch). Application of Eq. (2.2.9) in the present method requires a proper extension. Since the motion amplitudes are not constrained in any way, the wake cannot be described just with its x – coordinate; rather, its points are described by a vector $\mathbf{r}(s;t) \in \partial D_W$. Considering the position of the trailing edge, it is seen that it does not coincide with the vector $[c,0]^T$. In the present model it is described by the more complicated

vector $\mathbf{r}(s_{TE};t) = \partial D_B \cap \partial D_W$. Thus the wake evolution equation (2.2.9) is recast in the more complex form

$$\gamma_W(s;t) = \gamma_W\left(s_{TE};t-t_{TE}\right)\ , \tag{2.2.10}$$

such that $\mathbf{r}(s;t) \in \partial D_W(t)$ and $\mathbf{r}(s_{TE};t-t_{TE}) = \partial D_B \cap \partial D_W(t-t_{TE})$. In Eq.(2.2.10) $t_{TE} = U^{-1}\left|r(s \mid s_{TE};t)\right|$ where $\mathbf{r}(s \mid s_{TE};t)$ denotes the relative position of the wake point $\mathbf{r}$(s; t) with respect to the trailing edge position at a past time $\mathbf{r}(s_{TE};t-t_{TE})$. In essence, t_{TE} is the time that a material point needs to travel from the trailing edge to the wake point $\mathbf{r}$(s; t) with the free – stream velocity (i.e ignoring the vorticity interaction effects); see Fig.2.3. It is evident that this extension of the linearized Kutta condition Eq.(2.2.9) retains approximately the material conservation of the vorticity. Using Eq. (2.2.10) in the no – entrance boundary condition (2.1.5) we have

$$\begin{aligned}\left(\mathbf{V_A}-\mathbf{V}_\infty-\mathbf{V_G}\right)\cdot\mathbf{n} = &\frac{1}{2\pi}\int_{\partial D_B}\frac{\gamma_B(\xi;t)}{\left|\mathbf{r}\left(\xi \mid \mathrm{s};\mathrm{t}\right)\right|^2}\left\{\hat{\mathbf{k}}\times\mathbf{r}\left(\xi \mid s;t\right)\right\}\cdot\mathbf{n}d\xi \\ &\frac{1}{2\pi}\int_{\partial D_W}\frac{\gamma_W(\xi \mid \xi_{TE};t-t_{TE})}{\left|\mathbf{r}\left(\xi \mid \mathrm{s};\mathrm{t}\right)\right|^2}\left\{\hat{\mathbf{k}}\times\mathbf{r}\left(\xi \mid s;t\right)\right\}\cdot\mathbf{n}d\xi.\end{aligned} \tag{2.2.11}$$

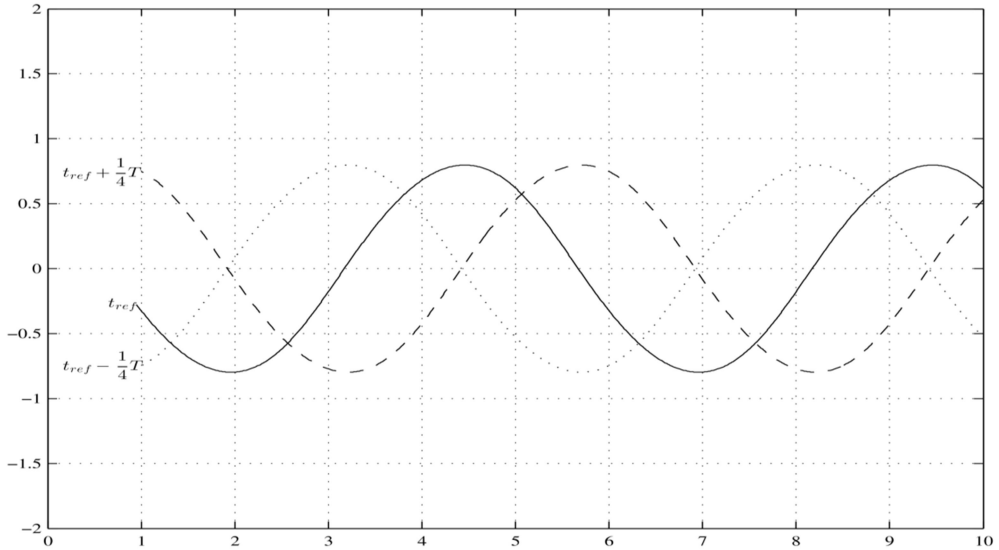

Figure 2.3: Successive plots of the trailing wake geometry ∂D_W for harmonic motion of foil with period T. The geometry is visualized for an arbitrary time value t_{ref} (solid line), a previous one $t_{ref} - T/4$ (dotted line) and a future one $t_{ref} + T/4$ (dashed line). The leftmost point of each curve coincides with the trailing edge position at the corresponding time

The only unknown in the integral equation (2.2.11) is the bound vorticity distribution $\gamma_B(s;t)$.

2.3 Pressure and Forces Calculation

Since the wing is assumed to be equivalent to a thin foil, only differences in pressure are of interest. The pressure difference coefficient on the foil is defined as

$$\Delta C_P = \frac{[\![p]\!]}{\frac{1}{2}\rho U^2} \tag{2.3.1}$$

To calculate the pressure difference coefficient, we employ an unsteady version of Bernoulli's equation by integration of Euler's equations (Filippas, 2013). The resulting expression is

$$\frac{\partial \Phi}{\partial t} + \frac{1}{2}(\nabla\Phi)^2 + \frac{p - p_\infty}{\rho} - \nabla\Phi \cdot (\mathbf{V}_\infty + \mathbf{V}_\mathbf{G}) = 0. \tag{2.3.2}$$

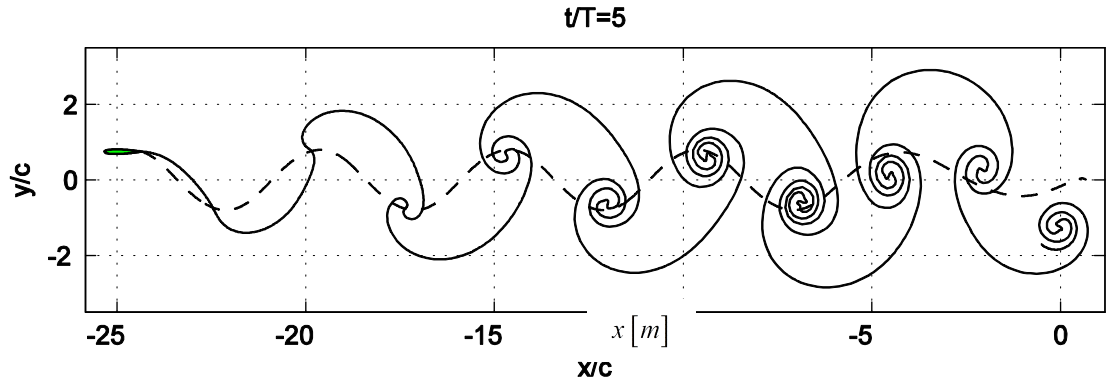

Figure 2.4: Snapshot of trailing vortex sheet in flapping motion (Filippas, 2013). The free trailing sheet is shown in solid lines, while the frozen wake defined as in the present work is shown in dashed lines. The vortices shed

at the highest and lowest points of the foil trajectory gather the free vortices around them, as their intensity is locally maximum. The result is a clockwise pattern around the vortices shed at the lowest trajectory points and counter – clockwise pattern at the highest points. This causes a jet – like flow between them, resulting in net thrust.

The derivation of Eq.(2.3.2) assumes that the background velocity $\mathbf{V_G}$ is weakly rotational so terms involving $\nabla \times \mathbf{V_G}$ can be ignored. In Eq.(2.3.2), $\Phi = \Phi(x, y; t)$ is the perturbation potential, $p = p(x, y; t)$ is the absolute pressure and p_∞ is the pressure at infinity. The flow is assumed to be incompressible, so the fluid density ρ is assumed constant.

An important note concerning Eq.(2.3.2) is that the involved spatial and time derivatives are written in the sense of space values. In the present method though, as is common in BEM, the potential values and their derivatives are calculated in a body – fixed reference frame in the sense of traces. We remind that the trace value of the potential is defined by the relation

$$\varphi(s; t) = \Phi\left(x(s), y(s); t\right), \ \left[x(s), y(s)\right]^T \in \partial D \ . \tag{2.3.3}$$

Taking the total derivative of the potential trace $\varphi\left(s; t\right) = \Phi\left(x(s), y(s); t\right)$ with respect to the curvilinear coordinate s, such that $r\left(s; t\right) \in \partial D$, we have

$$\begin{aligned} d\varphi &= \frac{\partial \Phi}{\partial t} dt + \frac{\partial \Phi}{\partial x} \cdot \left(\frac{\partial x}{\partial s} \cdot ds + \frac{\partial x}{\partial t} \cdot dt \right) + \frac{\partial \Phi}{\partial y} \cdot \left(\frac{\partial y}{\partial s} \cdot ds + \frac{\partial y}{\partial t} \cdot dt \right) = \\ &= \frac{\partial \Phi}{\partial t} dt + \nabla \Phi \cdot \left(\frac{\partial \mathbf{r}}{\partial s} \cdot ds + \frac{\partial \mathbf{r}}{\partial t} \cdot dt \right) \end{aligned} \tag{2.3.4}$$

Fixing a point on the boundary (fixing *s*), we have

$$d\varphi = \frac{\partial \Phi}{\partial t} dt + \nabla \Phi \cdot \left(\frac{\partial \mathbf{r}}{\partial t} \cdot dt \right) \quad . \tag{2.3.5}$$

For fixed *s*, $d\varphi = \nabla \varphi \cdot d\boldsymbol{\tau}$ is the velocity of the point $A \in \partial D$, $\mathbf{V_A}$ where $d\boldsymbol{\tau}$ is a surface tangent vector. Dividing Eq. (2.3.5) by *dt* we have

$$\frac{d\varphi}{dt} = \frac{\partial \Phi}{\partial t} + \nabla \Phi \cdot \mathbf{V_A} \ \Rightarrow \ \frac{\partial \Phi}{\partial t} = \frac{d\varphi}{dt} - \nabla \Phi \cdot \mathbf{V_A}. \tag{2.3.6}$$

(Politis 2005). Eq. (2.3.6) gives the value of the space time derivative from the value of the trace time – derivative.

We shall now find an expression between the space and trace values of the gradient in Eq. (2.3.2). Fixing time and releasing *s* in (2.3.4), we have

$$d\varphi == \nabla\Phi \cdot d\boldsymbol{\tau}, \qquad (2.3.7)$$

where $d\boldsymbol{\tau}$ is the differential tangent at the surface vector. It also holds by default that

$$d\varphi = \nabla\varphi \cdot d\boldsymbol{\tau}, \qquad (2.3.8)$$

Equating the RHS's of the above relations we obtain

$$\left(\nabla\Phi - \nabla\varphi\right) \cdot d\boldsymbol{\tau} = 0, \qquad (2.3.9)$$

which implies that the vector $\left(\nabla\Phi - \nabla\varphi\right)$ is normal to the surface. Since $\nabla\varphi$ is by default tangent to the surface, it follows that

$$\nabla\Phi = \left(\nabla\Phi \cdot \mathbf{n}\right) \cdot \mathbf{n} + \nabla\varphi\,. \qquad (2.3.10)$$

The first term in the RHS of (2.3.10) is known from the no – entrance boundary condition (2.2). Replacing (2.2) in (2.3.10) we have

$$\nabla\Phi = \left(\mathbf{V_A} - \mathbf{V}_\infty - \mathbf{V_G}\right) \cdot \mathbf{n} + \nabla\varphi. \qquad (2.3.11)$$

From equations (2.3.2), (2.3.6), (2.3.11) we have

$$\frac{p - p_\infty}{\rho} + \frac{d\varphi}{dt} - \left[\left(\mathbf{V_A} - \mathbf{V}_\infty - \mathbf{V_G}\right) \cdot \mathbf{n} + \nabla\varphi\right] \cdot \mathbf{V_A} + \frac{1}{2}\left[\left(\mathbf{V_A} - \mathbf{V}_\infty - \mathbf{V_G}\right) \cdot \mathbf{n} + \nabla\varphi\right]^2$$

$$- \left[\left(\mathbf{V_A} - \mathbf{V}_\infty - \mathbf{V_G}\right) \cdot \mathbf{n} + \nabla\varphi\right] \cdot \left(\mathbf{V}_\infty + \mathbf{V_G}\right) = 0 \Rightarrow$$

$$\frac{p - p_\infty}{\rho} = -\frac{d\varphi}{dt} + \left(\mathbf{V_A} - \mathbf{V}_\infty - \mathbf{V_G}\right) \cdot \nabla\varphi + \frac{1}{2}\left[\left(\mathbf{V_A} - \mathbf{V}_\infty - \mathbf{V_G}\right) \cdot \mathbf{n}\right]^2 - \frac{1}{2}\left(\nabla\varphi\right)^2. \qquad (2.3.12)$$

Applying Eq. (2.3.12) for two points A_L, A_U on the lower and upper side of the foil's surface, respectively, we have

$$\frac{p_L - p_\infty}{\rho} = -\frac{d\varphi_L}{dt} + \nabla\varphi_L \cdot \left(\mathbf{V_A} - \mathbf{V}_\infty - \mathbf{V_G}\right) + \frac{1}{2}\left[\left(\mathbf{V_A} - \mathbf{V}_\infty - \mathbf{V_G}\right)\cdot \mathbf{n_L}\right]^2 - \frac{1}{2}\left(\nabla\varphi_L\right)^2, \qquad (2.3.13a)$$

$$\frac{p_U - p_\infty}{\rho} = -\frac{d\varphi_U}{dt} + \nabla\varphi_U \cdot \left(\mathbf{V_A} - \mathbf{V}_\infty - \mathbf{V_G}\right) + \frac{1}{2}\left[\left(\mathbf{V_A} - \mathbf{V}_\infty - \mathbf{V_G}\right)\cdot \mathbf{n}_U\right]^2 - \frac{1}{2}\left(\nabla\varphi_U\right)^2. \qquad (2.3.13b)$$

Subtracting (2.3.13b) from (2.3.12a) we have

$$\frac{p_L - p_U}{\rho} = \frac{d[\![\varphi]\!]}{dt} + \nabla[\![\varphi]\!]\cdot\left(\mathbf{V}_\infty + \mathbf{V_G} - \mathbf{V_A}\right) - \frac{1}{2}\left[\left(\nabla\varphi_L\right)^2 - \left(\nabla\varphi_U\right)^2\right] +$$

$$+\frac{1}{2}\left\{\left[\left(\mathbf{V_A} - \mathbf{V}_\infty - \mathbf{V_G}\right)\cdot\mathbf{n_L}\right]^2 - \left[\left(\mathbf{V_A} - \mathbf{V}_\infty - \mathbf{V_G}\right)\cdot\mathbf{n_U}\right]^2\right\}. \qquad (2.3.14)$$

The term in brackets in (2.3.14) vanishes, since $\mathbf{n_L} = -\mathbf{n_U}$, and the thirds term in the RHS of the above equation becomes

$$\frac{1}{2}\left[\left(\nabla\varphi_L - \nabla\varphi_U\right)\cdot\left(\nabla\varphi_L + \nabla\varphi_U\right)\right] = \frac{1}{2}\nabla[\![\varphi]\!]\cdot\left(\nabla\varphi_L + \nabla\varphi_U\right) \qquad (2.3.15)$$

It holds for $\nabla\varphi_L$, $\nabla\varphi_U$ that

$$\nabla\varphi_L(s;t) = u_L(s;t) = \frac{1}{2}\gamma_B(s;t), \text{ and } \nabla\varphi_U(s;t) = u_U(s;t) = -\frac{1}{2}\gamma_B(s;t), \qquad (2.3.16)$$

so the term in the RHS of Eq. (2.3.15) vanished. Ultimately, the pressure difference coefficient is given by the expression

$$\Delta C_P = \frac{p_L - p_U}{\frac{1}{2}\rho U^2} = \frac{2}{U^2}\left[\frac{d[\![\varphi]\!]}{dt} + \nabla[\![\varphi]\!]\cdot\left(\mathbf{V}_\infty + \mathbf{V_G} - \mathbf{V_A}\right)\right]. \qquad (2.3.17)$$

Knowing the pressure difference coefficient, we can easily calculate the forces and moments on the foil, as well as the power input required to maintain its unsteady motion. In

the present work only forces that are induced from pressure variations between the foil's upper and lower surface sides are considered. The forces, moments and input power are given in the form of non – dimensional coefficients. They are rendered non – dimensional with characteristic fluid forces, moments and power quantities. Specifically;

$$C_L(t) \hat{=} \frac{L(t)}{\frac{1}{2}\rho U^2 c} = \frac{1}{c}\int_{\partial D_B} (\Delta C_P \cdot \mathbf{n}) \cdot \hat{\mathbf{y}} ds \tag{2.3.18}$$

is the instantaneous lift coefficient (expressing the force normal to the parallel stream U),

$$C_T(t) \hat{=} \frac{T(t)}{\frac{1}{2}\rho U^2 c} = -\frac{1}{c}\int_{\partial D_B} (\Delta C_P \cdot \mathbf{n}) \cdot \hat{\mathbf{x}} ds \tag{2.3.19}$$

is the instantaneous thrust coefficient (negative values correspond to drag), and

$$C_M(t) \hat{=} \frac{M(t)}{\frac{1}{2}\rho U^2 c^2} = \frac{1}{c^2}\int_{\partial D_B} (\Delta C_P \cdot \mathbf{n}) \cdot \mathbf{r}(s \mid s^*; t) ds \tag{2.3.20}$$

is the instantaneous moment coefficient, where $\mathbf{r}(s|s^*;\ t)$ is the vector pointing from the reference point $\mathbf{r}(s^*;t)$ (pivot point around which moments are calculated) to the surface point $\mathbf{r}$(s; t). Note that in Eqs. (2.3.18) – (2.3.20) the $\hat{\mathbf{x}}, \hat{\mathbf{y}}$ vectors denote the unit – vectors along the inertial reference frame axis. Finally, the instantaneous input power coefficient is calculated as

$$C_P(t) \hat{=} \frac{P_{in}(t)}{\frac{1}{2}\rho U^3 c} = -\frac{1}{Uc}\int_{\partial D_B} (\Delta C_P \cdot \mathbf{n}) \cdot \mathbf{V_A}(s;t) ds \tag{2.3.21a}$$

In the case of rigid motion the general velocity of a surface point of the foil $\mathbf{V_A}(s;t)$ is a combination of translation $\mathbf{V}$ and rotation $\Omega\hat{\mathbf{k}}$, and is expressed as $\mathbf{V_A}(s;t) = \mathbf{V} + \Omega\hat{\mathbf{k}} \times \mathbf{r}(s \mid s^*; t)$ and using the latter in Eq.(2.3.21) we obtain for the input and output power

$$P_{in}(t) = L(t)\dot{h} + M(t)\dot{\theta}, \quad P_{out}(t) = TU \tag{2.3.21b}$$

However, we have maintained the more general expression given by Eq.(2.3.21) in order to account also for the additional power associated with the elastic deformation, which will be considered below in Chapter 4.

For periodic foil motion and flow conditions (as e.g. in flapping foils) we are interested in amplitudes of the lift and moment coefficient and mean values of the thrust and input power coefficient per cycle. If the motion period is T and the responses have reached their periodic steady – state, the amplitudes and mean values of the above coefficients are calculated as follows;

$$\overset{o}{C}_L = \frac{2}{T}\int_0^T C_L(t)\cdot\cos\left(\frac{2\pi}{T}t\right)dt \tag{2.3.22}$$

for the lift coefficient amplitude,

$$\overline{C_T} = \frac{1}{T}\int_0^T C_T(t)\,dt \tag{2.3.23}$$

for the mean thrust coefficient,

$$\overset{o}{C}_M = \frac{2}{T}\int_0^T C_M(t)\cdot\cos\left(\frac{2\pi}{T}t\right)dt \tag{2.3.24}$$

for the moment coefficient amplitude, and

$$\overline{C_P} = \frac{1}{T}\int_0^T C_P(t)\,dt \tag{2.3.25}$$

for the mean input power coefficient.

Moreover, the Froude efficiency is defined as the ratio of output power over input power, as follows (Anderson et al, 1998)

$$\eta \hat{=} \frac{P_{out}}{P_{in}} = \frac{UT}{P_{in}} = \frac{U\overline{C_T}\frac{1}{2}\rho U^2 c}{\overline{C_P}\frac{1}{2}\rho U^3 c} = \frac{\overline{C_T}}{\overline{C_P}} \tag{2.3.26}$$

2.4 Numerical Scheme

The solution to the unsteady lifting problem is equivalent to the solution of the integral equation (2.2.11) for the vorticity distribution bound on the foil's surface. Knowledge of this

distribution renders the calculation of pressure around the foil possible, from which the forces acting on the foil can be calculated by integration using Eqs. (2.3.18) – (2.3.21).

2.4.1 Discretization of vorticity distributions

The DVM solves the lifting problem in the time domain by calculating the discrete distribution of the bound vorticity at each time step, thus allowing for calculation of forces in transient as well as periodic conditions. The integral equation (2.2.11) is discretized appropriately to N_B panels on the foil's surface and N_W panels on the trailing wake surface, respectively. The foil vorticity is approximated by the following distribution of discrete vortices

$$\Gamma_{Bi} = \Gamma_B(s_i;t), \quad i = 1 \cdots N_B, \quad \text{located at} \quad \mathbf{r}(s_i;t) \in \partial D_B \tag{2.4.1.1}$$

in the sense that

$$\Gamma_{Bi}(t) = \int_{s_i}^{s_{i+1}} \gamma_B(s;t)ds, \quad i = 1,...,N_B \tag{2.4.1.2}$$

In a similar fashion, the wave vorticity distribution is approximated by

$$\Gamma_{Wj} = \Gamma_W(s_j;t), \quad j = 1 \cdots N_W, \quad \text{located at} \quad \mathbf{r}(s_j;t) \in \partial D_W, \tag{2.4.1.3}$$

in the sense that

$$\Gamma_{Wj}(t) = \int_{s_j}^{s_{j+1}} \gamma_W(s;t)ds, \quad j = 1,...,N_W. \tag{2.4.1.4}$$

In Figure 2.5 the velocity field of a point vortex in (0,0) is shown.

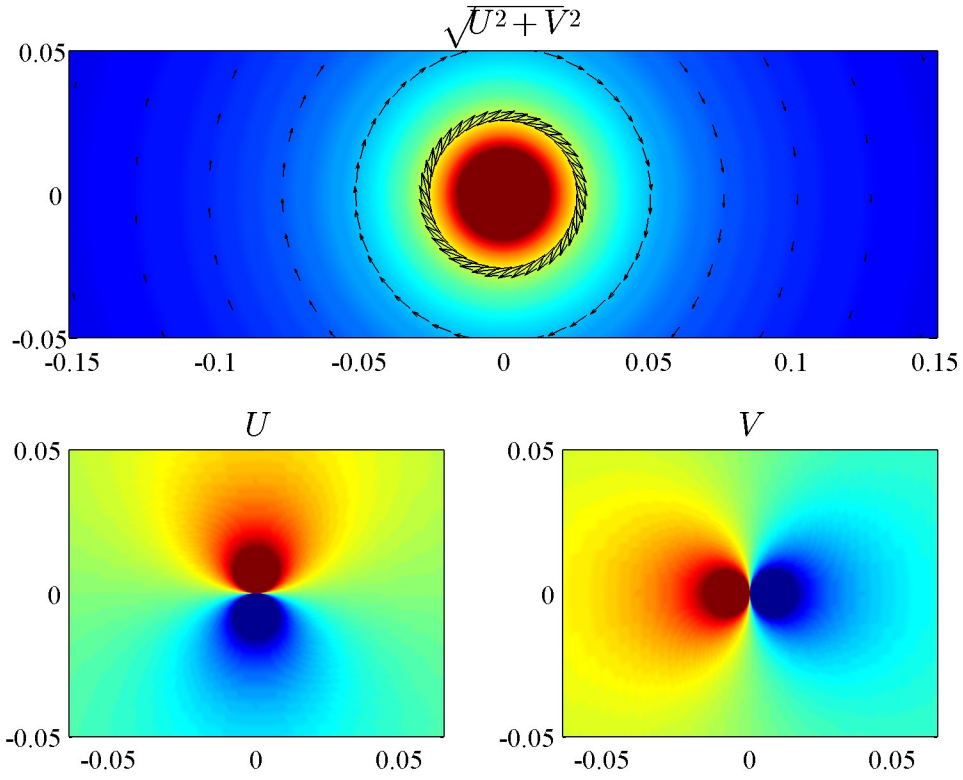

Figure 2.5: Velocity field of a unit – strength vortex placed at (0,0). The upper figure shows the absolute value of the velocity which is radially symmetric, while the lower figures display the horizontal velocity (left) and vertical velocity (right), which are symmetrical about the x and y axis, respectively.

2.4.2 Body, wake & temporal discretization

Since the discrete model is assumed to start from rest, the number of wake panels N_W is equal to the number of time steps N_t. The foil is discretized into N_B chord panels according to the cosine spacing method so that panels are accumulated in the leading and trailing edge regions were the most significant hydrodynamic variations are expected according to linear theory; see Fig.2.6. The foil elements are created as follows;

- Create a vector containing N_B+1 iso – spaced values $\chi_i, i=1,...,\mathrm{N}_B+1$ in the interval $[-\pi, 0]$
- Apply the transformation $x_i = \frac{c}{2}\left[\cos(\chi_i)+1\right], i=1,...,N_B+1$ where c is the foil's chord length. The values x_i are cosine – spaced in the interval $[0, c]$

- Calculate the length of each panel (projected to its chord) $dx_i = x_{i+1} - x_i, i = 1,...., N_B$
- Place a vortex point and a collocation point at each panel placed at 1/4 and 3/4 of the panel, as follows

$$xvor_i = \sum_{j=1}^{i-1} dx_j + 0.25 \cdot dx_i \tag{2.4.2.1}$$

$$xcp_i = \sum_{j=1}^{i-1} dx_j + 0.75 \cdot dx_i \tag{2.4.2.2}$$

in the body – fixed reference frame. This way the collocation points are always downstream of the vortex points. Also note that vortex or collocation points are never placed exactly at the leading or trailing edge, thus avoiding manifestation of singularities in the discrete model.

The time is discretized in equal discrete steps Δt. The wake panels have length $dw = U \cdot \Delta t$. The ratio of wake panel length to trailing edge region foil panel is a control parameter of the method. The wake panels have the same direction with the free stream velocity $\mathbf{V}_\infty$ which is consequence of the (approximate) material conservation of vorticity, as materialized by the present wake model. In this case we consider each wake panel to be a vector

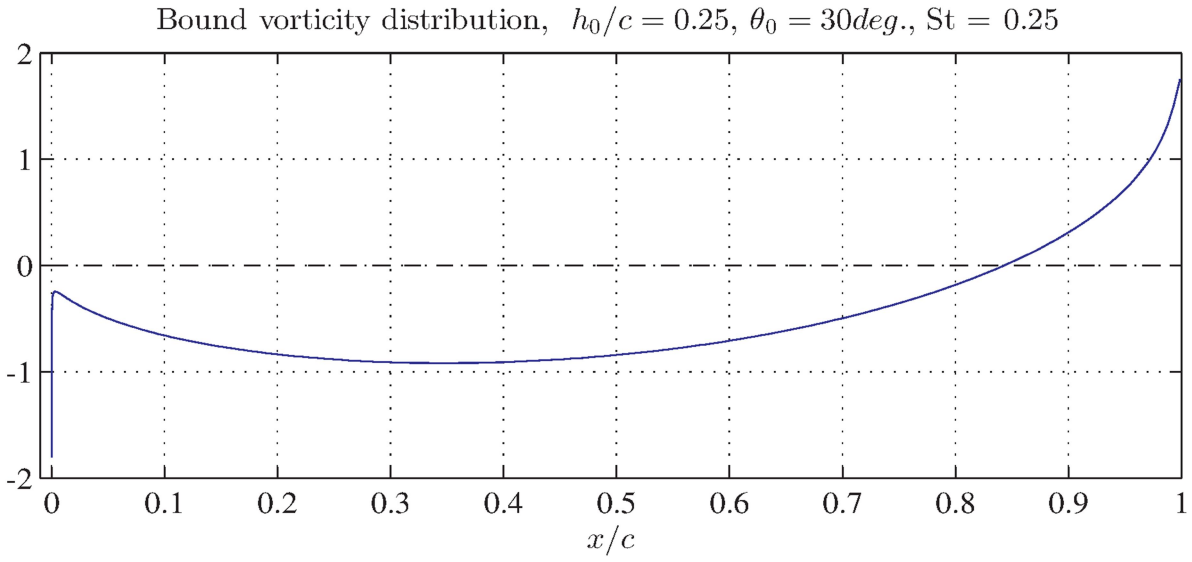

Figure 2.6: Bound vorticity for a flapping motion case. The time instant has been chosen so that the distribution displays significant variations in both the leading edge and trailing edge. This acts as an argument supporting the usage of cosine spacing for the collocation points on the foil's mean camber line

$$\mathbf{dw} = \mathbf{V}_\infty \cdot \Delta t = \left(dw_x, dw_y\right) = U \cdot \left(\cos\left(a\right), \sin\left(a\right)\right), \tag{2.4.2.3}$$

where $a = \tan^{-1}\left(\frac{\mathbf{V}_\infty \cdot \hat{\mathbf{y}}}{U}\right)$ is the mean angle of attack of the foil.

2.4.3 Solution of the hydrodynamic problem

The no – entrance boundary condition (2.2.11) is discretized by replacing the vorticity distributions γ_B, γ_W by the distributions of equivalent point vortices Γ_B, Γ_W. The resulting expression is

$$\sum_{j=1}^{N_B} \Gamma_{Bj} \cdot w_{ij}^B = -\sum_{k=1}^{N_W} \Gamma_{Wk} w_{ik}^W + U_{Bi}, i = 1,..., N_B \tag{2.4.3.1}$$

At each time step t_n, the term U_{Bi} is the RHS of the no – entrance boundary condition Eq. (2.2) evaluated at the collocation points, Eq (2.4.2.2). The terms $w^B{}_{ij}$ and $w^W{}_{ik}$ are the values of the normal velocity also at the collocation points $i = 1,..., N_B$ velocities, induced by the unit – strength bound point vortices located at $\left(xvor_j, yvor_j\right) = \mathbf{r}\left(s_j, t_n\right), j = 1,..., N_B$, and trailing wake unit – strength point vortices located at $\left(xw_k, yw_k\right) = \mathbf{r}\left(s_k, t_n\right), k = 1,..., N_W$, respectively. More specifically

$$w_{ij}^B\ \left(t_n\right) = \frac{\left\{-\mathbf{r}\left(s_j \mid s_i; t_n\right) \times \hat{\mathbf{k}}\right\} \cdot \mathbf{n}_i\left(t_n\right)}{\left|\mathbf{r}\left(s_j \mid s_i; t_n\right)\right|^2}, \quad w_{ik}^W\ \left(t_n\right) = \frac{\left\{-\mathbf{r}\left(s_k \mid s_i; t_n\right) \times \hat{\mathbf{k}}\right\} \cdot \mathbf{n}_i\left(t_n\right)}{\left|\mathbf{r}\left(s_k \mid s_i; t_n\right)\right|^2}. \tag{2.4.3.2}$$

More specifically, the induced velocities are given by the expressions

$$w_{ij}^B = \frac{1}{2\pi}\left(-\frac{yvor_j - ycp_i}{\left(xvor_j - xcp_i\right)^2 + \left(yvor_j - ycp_i\right)^2}, \frac{xvor_j - xcp_i}{\left(xvor_j - xvor_i\right)^2 + \left(yvor_j - ycp_i\right)^2}\right) \cdot \mathbf{n}_i \tag{2.4.3.3}$$

$$w_{ik}^W = \frac{1}{2\pi}\left(-\frac{yw_k - ycp_i}{\left(xw_k - xcp_i\right)^2 + \left(yw_j - ycp_i\right)^2}, \frac{xw_k - xcp_i}{\left(xw_k - xcp_i\right)^2 + \left(yw_k - ycp_i\right)^2}\right) \cdot \mathbf{n}_i \tag{2.4.3.4}$$

The positions of collocation points $\left(xcp_i, ycp_i\right)$, bound discrete point vortices $\left(xvor_j, yvor_j\right)$ and trailing wake point vortices $\left(xw_k, yw_k\right)$ must be given in the inertial reference frame, as provided by Eqs. (2.4.3.3) - (2.4.3.4). The positions of the trailing wake point vortices $\left(xw_k, yw_k\right)$ are given by the discrete equivalent of Eq.(2.2.10) as follows

$$\left(xw_k, yw_k\right)\Big|_{t_n} = \begin{Bmatrix} \left(x_{TE} + 0.25\cdot dw_x, y_{TE} + 0.25\cdot dw_y\right)\Big|_{t_{n-k+1}}, \text{ if } n-k+1>0 \\ \text{undefined, otherwise} \end{Bmatrix} \tag{2.4.3.5}$$

Note that the trailing wake point vortices are placed at 1/4 location of each wake panel.

In the discretized no – entrance boundary condition (2.4.3.1) the trailing wake point vortices $\Gamma_{Wk}, k \geq 2$ are all known from the history of the motion, by virtue of Eq. (2.2.10), while the value of Γ_{W1} is an unknown quantity at every time step. We will follow an informal procedure and attempt to incorporate it in a straightforward way in the linear system Eqs. (2.4.3.1). We consider a time step of the discrete vortex method, $t \in \left[t_n, t_{n+1}\right]$ and let $\tau = t - t_n$ By definition, the discrete vortex strength of the first wake element is

$$\Gamma_{W1}\left(t_n\right) = \int_{s_k}^{s_{k+1}} \gamma_W\left(s; t_n\right) ds, \tag{2.4.3.6}$$

Assuming that $s \cong x$, setting $x = c + U\tau$ and replacing in Eq. (2.4.3.6), we acquire

$$\Gamma_{W1}\left(t_n\right) = \int_0^{\Delta t} \gamma_W\left(c + U\tau; t_n\right) U d\tau \cong \int_0^{\Delta t} \gamma_W\left(c; t_n\right) U d\tau. \tag{2.4.3.7}$$

where $\Delta t = t_n - t_{n-1}$. Replacing the wake vorticity using Eq. (2.2.4) we have (see Fig.2.6)

$$\Gamma_{W1}\left(t_n\right) = -\frac{1}{U}\int_0^{\Delta t} \frac{d\Gamma\left(t\right)}{dt} U d\tau = -\frac{1}{U}\int_0^{\Delta t} \frac{d\Gamma\left(t_{n-1} + \tau\right)}{d\tau} U d\tau = -\int_0^{\Delta t} d\Gamma(t_{n-1} + \tau) =$$

$$= \Gamma\left(t_{n-1}\right) - \Gamma\left(t_n\right) \tag{2 .4.3.8}$$

Eq. (2.4.3.8) stresses the fact that every change of circulation around the foil must be counterbalanced by an opposite change in the circulation of the vortex wake, so that Kelvin's theorem is satisfied at each time step. The first term in the RHS is the circulation around the

foil at the previous time step which is already known. The second term is the sum of the bound point vortices at the current time step

$$\Gamma\left(t_n\right)=\sum_{j=1}^{N_B}\Gamma_{Bj}, \tag{2.4.3.9}$$

which is unknown. However since it is a linear combination of the unknown quantities, it can be transferred to the LHS of the linear system. From Eq. (2.4.3.1), (2.4.3.8) & (2.4.3.9) we have

$$\sum_{j=1}^{N_B}\Gamma_{Bj}\cdot\left(w_{ij}^{B}-w_{i1}^{W}\right)=-\Gamma\left(t_{n-1}\right)\cdot w_{i1}^{W}-\sum_{k=2}^{N_W}\Gamma_{Wk}w_{ik}^{W}+U_{Bi}, i=1,...,N_B. \tag{2.4.3.10}$$

Eq. (2.4.3.10) constitutes a linear system of equations that is solved at each time step for the intensities of the bound point vortices Γ_{Bj}, $j=1,...,N_B$.

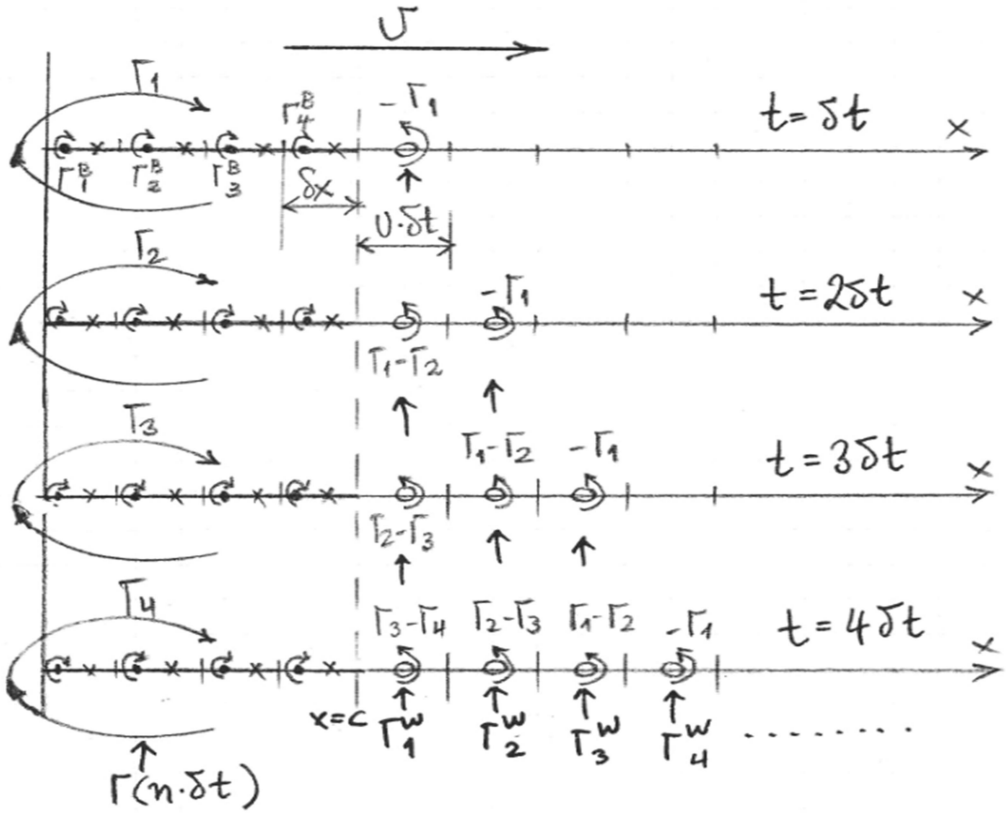

Figure 2.7: Visualization of the discrete wake model utilized in the present DVM. The foil starts from rest and the first wake vortex is shed, with intensity equal to $-\Gamma_1$, opposing the circulation around the foil. At each subsequent time step t_n, the intensity of the shed vortex is equal to $\Gamma\left(t_{n-1}\right)-\Gamma\left(t_n\right)$

2.4.4 Calculation of pressure and forces in DVM

The pressure difference coefficient is calculated via a discrete expression equivalent to Eq.(2.3.17). According to the present scheme, we have

$$\frac{d\left[\!\left[\varphi\left(t_n\right)\right]\!\right]_i}{dt}=\frac{1}{\Delta t}\sum_{j=1}^{i}\left[\Gamma_{Bj}\left(t_n\right)-\Gamma_{Bj}\left(t_{n-1}\right)\right] \tag{2.4.4.1}$$

and

$$\nabla\left[\!\left[\varphi\left(t_n\right)\right]\!\right]_i=\frac{\Gamma_{Bi}\left(t_n\right)}{dx_i}\cdot\boldsymbol{\tau}_i\left(t_n\right). \tag{2.4.4.2}$$

Substituting the above expressions in Eq.(2.3.17) we have

$$\Delta C_{Pi}\equiv\left[\!\left[C_{Pi}\left(t_n\right)\right]\!\right]=\frac{2}{U^2}\left[\frac{1}{\Delta t}\sum_{j=1}^{i}\left[\Gamma_{Bj}\left(t_n\right)-\Gamma_{Bj}\left(t_{n-1}\right)\right]+\frac{\Gamma_{Bi}}{dx_i}\cdot\boldsymbol{\tau}_i\cdot\left(\mathbf{b}_i\cdot\boldsymbol{\tau}_i\right)\right], \tag{2.4.4.3}$$

where $\mathbf{b}_i=\mathbf{V}_\infty+\mathbf{V}_{\mathbf{G}i}-\mathbf{V}_{\mathbf{A}i}$.

With the pressure difference coefficient known at each time step, the forces, moments and power coefficients time histories can be easily calculated by evaluating the integrals in Eqs (2.3.18) – (2.3.21) .

Detailed results and comparison of the present DVM against other theoretical methods BEM and experimental data, in the case of rigid foils, will be presented in the next Chapter of the thesis. In particular, unsteady thin hydrofoils at various conditions, including heaving and pitching motion, flapping hydrofoils and hydrofoils in gust will be presented and discussing validating the developed numerical scheme.

2.5 Concluding Remarks

A velocity potential, low order panel method, DVM, has been constructed for the solution of the unsteady lifting problem of a thin foil. The flow is governed by the Laplace equation (conservation of mass). The foil and its wake are assumed to be surfaces of potential discontinuity, and are represented by a distribution of vortices, which at each time during the solution satisfy the Neumann no – entrance boundary condition on the foil surface, and the dynamic boundary condition on the vortex wake, ignoring wake vorticity interactions with a simplified wake model. The field equation is immediately satisfied by the distribution of vortices, since the potential generated from each vortex by default satisfies it, and the potential from a distribution of vortices is the result of linear superposition of the single – vortex potentials.

The flow is comprised by a free stream velocity due to the foil's forward motion, radiation – potential velocities due to the foil's unsteady motions (such as in flapping mode) and, possibly rotational, flow disturbances such as a sinusoidal gust. Due to the flow's unsteadiness, vorticity is shed at each time step from the trailing edge to the trailing vortex sheet. For the calculation of pressures, an unsteady Bernoulli equation is employed, which does not make the usual negligibility of disturbance velocities assumption of linear, analytic theories. The wake complies with a prescribed model which assumes that the shed vortices coincide with the trajectory of the trailing edge, in an inertial frame of reference, or equivalently in a foil mean – position frame, travel downstream with celerity equal to the free stream velocity.

The distribution of the bound vorticity is calculated by applying a collocation scheme on the foil's surface, satisfying the kinematic boundary condition at a discrete number of points. This enables the calculation of circulation around the foil at each time step, and consequently that of forces and moments.

In the present DVM we have assumed that points on the foil may possess a velocity, which is in a straightforward way incorporated in the no – entrance boundary condition in the case where is it *a priori* known. In the course of this work we will consider the chordwise passive elastic deformations of the foil which couple the velocity of points on the foil’s camber line with the potential flow around the body.

Chapter 3: Numerical Study of Discrete Vortex Method – DVM

The effectiveness of tackling 2D – flapping foils problems with DVM described in detail in the previous section is investigated in this chapter, in the case of rigid bodies.

Initially, the performance of the developed method is examined for the case of constant angle of attack. The convergence of the method is first shown in steady-state problems starting from rest, by increasing the space and time discretization. Subsequently, oscillatory motions of the foil will be studied, i.e. heaving and pitching motion and comparison against analytic results (in the case of small amplitudes). Next the highly interesting flapping motion is examined. The latter is obtained by combination of the two oscillatory motions with specific phase difference, which under proper selection of the kinematic parameters can produce thrust. Finally, the unsteady problem associated with the effect of an oscillatory gust is also investigated and results from DVM are compared against analytical solution of the Sears problem (Newman, 1977).

The validity of the present method is examined by comparing the results with linear analytic theory results and other method and experimental results from the literature.

3.1 Kinematic Parameters

The foil is assumed to travel towards the negative of the horizontal x axis with constant velocity U and possibly having an angle of attack a. It performs an unsteady motion comprising of simultaneous heaving and pitching. In this work the unsteady motion considered is flapping motion, where both the heaving and pitching motions are harmonic in time. They are given by the relations

$$h(t) = F(t) \cdot h_0 \cdot \sin(\omega t) = F(t) \cdot \mathrm{Re}\left\{ \overset{o}{h}_0 \cdot e^{i\omega t} \right\} = F(t) \cdot \mathrm{Re}\left\{ h_0 \cdot e^{-i\pi/2} \cdot e^{i\omega t} \right\}, \tag{3.1.1}$$

$$\theta(t) = \theta_0 \cdot \sin(\omega t + \psi) = F(t) \cdot \mathrm{Re}\left\{ \overset{o}{\theta}_0 \cdot e^{i\omega t} \right\} = F(t) \cdot \mathrm{Re}\left\{ \theta_0 \cdot e^{-i\left(\pi/2 - \psi\right)} \cdot e^{i\omega t} \right\}, \tag{3.1.2}$$

respectively. In the above relations, h_0 is the heaving amplitude, θ_0 is the pitching amplitude and ψ is the phase lag between the two motions. The function $F(t) = 1 - \exp(-\alpha t^p)$ is a ramp function allowing for smooth transition between initial state of rest and unsteady motion. The parameters that affect the foil's performance are

- h_0 / c : non – dimensional heaving amplitude
- ψ : phase lag between heaving and pitching motion
- a_{max} : maximum effective angle of attack
- $k_r = \dfrac{\omega c}{2U}$: reduced frequency
- $St = \dfrac{fA}{U}$: Strouhal number, where $A \cong 2h_0$ is the characteristic trailing edge amplitude and $f = \omega / 2\pi$ is the oscillatory motion frequency.
- x_R : non – dimensional chordwise position of pivot point

The reduced frequency k_r is a non – dimensional parameter that associates the oscillatory motion frequency ω with a typical hydrodynamic time scale, $c/(2U)$, which is the time it takes for a fluid particle moving with the free – stream velocity to travel a half – chord length. The Strouhal number St is a non – dimensional parameter associating the motion frequency with the vortex sheet forming behind the foil during its motion. It is a well – known fact that when bluff bodies, e.g. spheres, are placed in a uniform flow, a drag – producing Karman vortex sheet forms behind them. In the flapping motion case a reverse Karman vortex sheet is formed (Koochesfahani, 1989; Triantafyllou et al, 1993), creating a jet behind the foil which leads to thrust production. The Strouhal number is also a degree of the non – linearity of the flow.

The maximum effective angle of attack a_{max} is defined by the following expression (see also Read et al, 2003)

$$a_{max} = \tan^{-1}\left(\frac{\omega h_0}{U}\right) - \theta_0 \tag{3.1.3}$$

which is preferred as representative non-dimensional parameter instead of the pitching amplitude θ_0 ; Read et al (2003)

A sketch is given in figure 3.1 to assist in the interpretation of (3.1.3). Consider an observer fixed on the pivot point of the foil. Ignoring pitching motion, this observer is subject to an inclined velocity, a result of the free – stream velocity U and the heaving velocity $\dot{h}(t)$. The apparent angle of attack is then $\tan^{-1}\left[-\frac{\dot{h}(t)}{U}\right]$. Adding the pitching motion, the total angle of attack is given by the expression

$$a_{eff}(t) = \tan^{-1}\left[-\frac{\dot{h}(t)}{U}\right] + \theta(t) \tag{3.1.4}$$

Assuming harmonic heaving and pitching motion profiles and $\psi \cong 90^o$, as it has shown to be the most efficient value of the phase lag (Anderson et al, 1998), we have

$$a_{eff}(t) = \tan^{-1}\left[-\frac{\omega h_0 \cos(\omega t)}{U}\right] + \theta_0 \sin\left(\omega t + \pi/2\right) = \tan^{-1}\left[-\frac{\omega h_0 \cos(\omega t)}{U}\right] + \theta_0 \cos(\omega t) \tag{3.1.5}$$

From Eq.(3.1.5) and assuming small motion amplitudes, we acquire (3.1.3). It is noted here

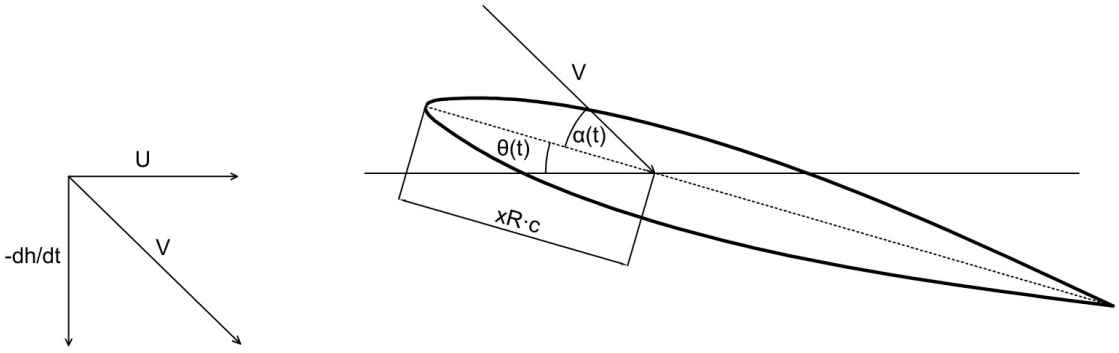

Figure 3.1: Derivation of effective angle of attack

that positive values of the pitching angle correspond to nose – down configurations. In the case that a constant angle of attack exists, it is added to expression (3.1.5)

The pivot point x_R is naturally placed somewhere on the chord length of the foil. An obvious choice would be the pressure centre which, although unknown in cases of unsteady flow around the foil, can be approximated by steady analytic theory results. For the case of a symmetric foil approximated by a thin flat plate it holds that $x_R = 1/4$. In practice x_R is taken between 0.25 and 0.3. The position of the pivot point affects the power input to the foil, rendering its choice important for flapping foil propulsion. It is noted here that in the case of flexible foils the pivot point is generally be placed near the leading edge, as is the case in most bio-swimmers in nature.

The foil travels in otherwise undisturbed fluid with constant velocity $-\mathbf{V}_\infty$, while simultaneously performing periodic unsteady flapping motion with zero mean value. An equivalent from a fluid mechanics perspective case is that of a foil with zero mean velocity performing flapping motion around its mean position while subject to a free – stream velocity $\mathbf{V}_\infty$. In this reference frame, the positions of points on the foil are given by the expressions

$$x(t) = (x_0 - x_R \cdot c) \cdot \cos(\theta(t)) - y_0 \cdot \sin(\theta(t)) + x_R \cdot c, \tag{3.1.6}$$

$$y(t) = (x_0 - x_R \cdot c) \sin(\theta(t)) + y_0 \cdot \cos(\theta(t)) + h(t), \tag{3.1.7}$$

where $[x_0, y_0]^T$ is the initial position of each point in the body-fixed reference frame, so x_0, where x_0 is the chordwise distance of foil points from the leading edge. In this work we have mainly considered uncambered hydrofoils and thus, $y_0 = 0$, however, the analysis is also applicable to the general case.

3.2 Symmetric foil at constant angle of attack

The present DVM is first validated by reproducing known results from the steady linear theory. The case of a symmetric foil at a constant angle of attack is treated in the framework of small thickness theory as a branch cut on the x axis resulting in the following

expression for the lift and moment coefficient (corresponding to the steady response of a flat plate,) see, e.g., Katz & Plotkin (1991)

$$C_L = 2\pi a, \tag{3.2.1}$$

$$C_M = \frac{1}{2}\pi a, \tag{3.2.2}$$

respectively, where a is the angle of attack, defined as the angle of the free – stream velocity with respect to the chord.

Apart from the agreement with the linear theory, we are interested in the convergence characteristics of the present method. To this end, we modify the number of chord elements used in the numerical solution. We therefore use 10, 20, 50, 100 elements chordwise and calculate the relative error of each approximation with the value acquired from the case with 100 chord elements. The number of time steps per chord length travelled is set to 100. The simulation runs until the foil has travelled a distance equal to 100 chord lengths. In Figure 3.2 the convergence of the lift coefficient is shown, while Figure 3.3 presents the convergence of the moment coefficient. The horizontal axis displays the number of chord elements used for each approximation.

In all cases the method is shown to be rapidly convergent. It is remarkable that the error for the lift coefficient is negligible, even for 10 chord elements. This fact is due to the specific arrangement of bound vortex – collocation point used in this work. It can be proven that the $1/4$- $3/4$ choice leads to the exact value for the lift coefficient in the steady case, even for a single chordwise panel (James, 1971; Katz & Plotkin 1991). However the vorticity, and hence the pressure, distribution is not adequately reproduced for low numbers of chord elements which causes inaccuracies in the moment coefficient calculations. The relative error for the moment coefficient when 10 chord elements are used is around 20%

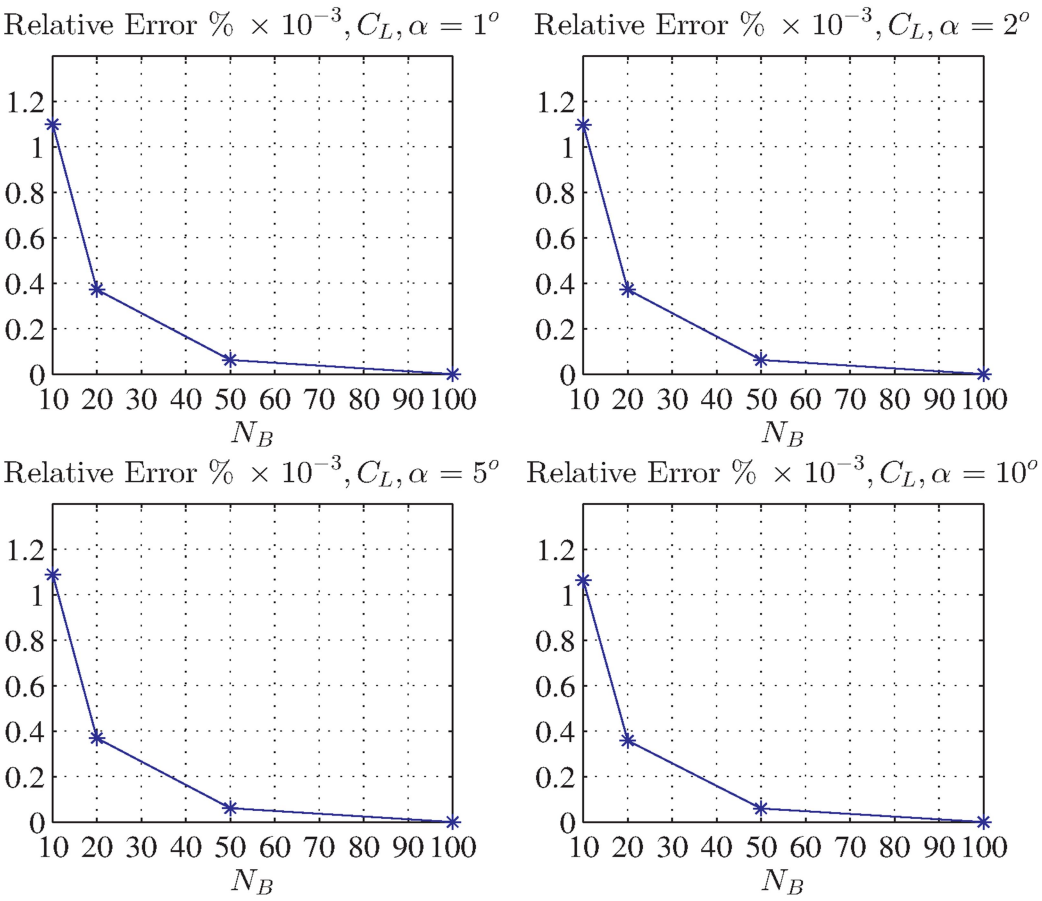

Figure 3.2: Lift coefficient convergence

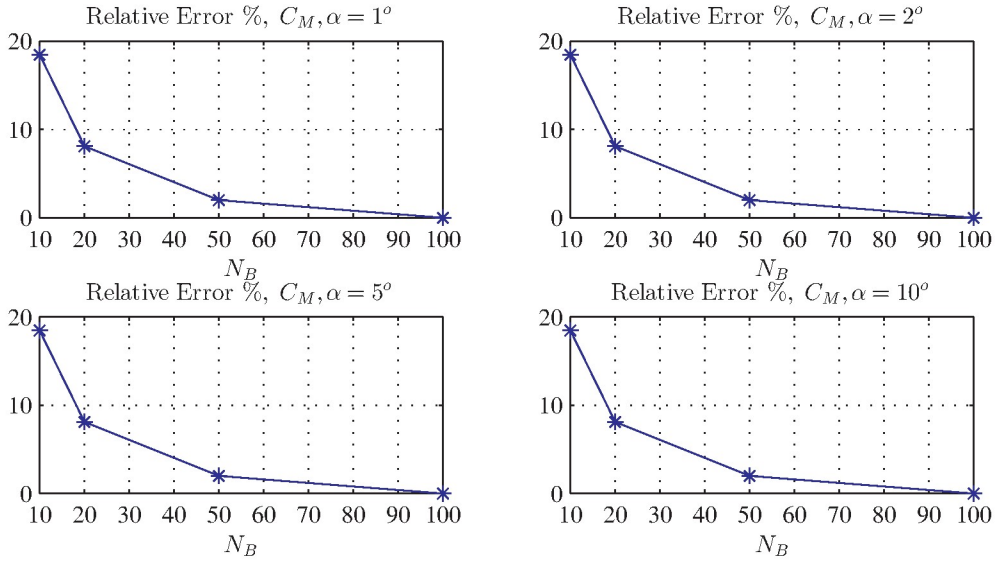

Figure 3.4: Moment coefficient convergence

The problem of a flat plate started abruptly from rest with a constant angle of attack assumes an analytical solution by the Wagner's function (Newman, 1977), by considering the equivalent problem of the foil moving with zero angle of attack with speed U and at time t =0 a vertical component is added to the velocity in a step – like manner. The steady – state result for the lift coefficient is of course correctly predicted by the steady analytical theory, but a transient response is now produced. The time history of the lift coefficient is given by the following approximate expression

$$C_L(t) \approx C_{L0} \cdot \left(1 - 0.165e^{-0.045s} - 0.335e^{-0.3s}\right), \tag{3.2.3}$$

(Kier, 2005), where $s = \dfrac{Ut}{c/2}$ is the number of half – chords travelled at time t and C_{L0} is given by relation (3.2.1). Figure 3.5 shows the time histories of the lift coefficient as predicted by the present method compared to relation (3.2.2).

The time histories acquired by the DVM display very good agreement with the predictions by Wagner's function.

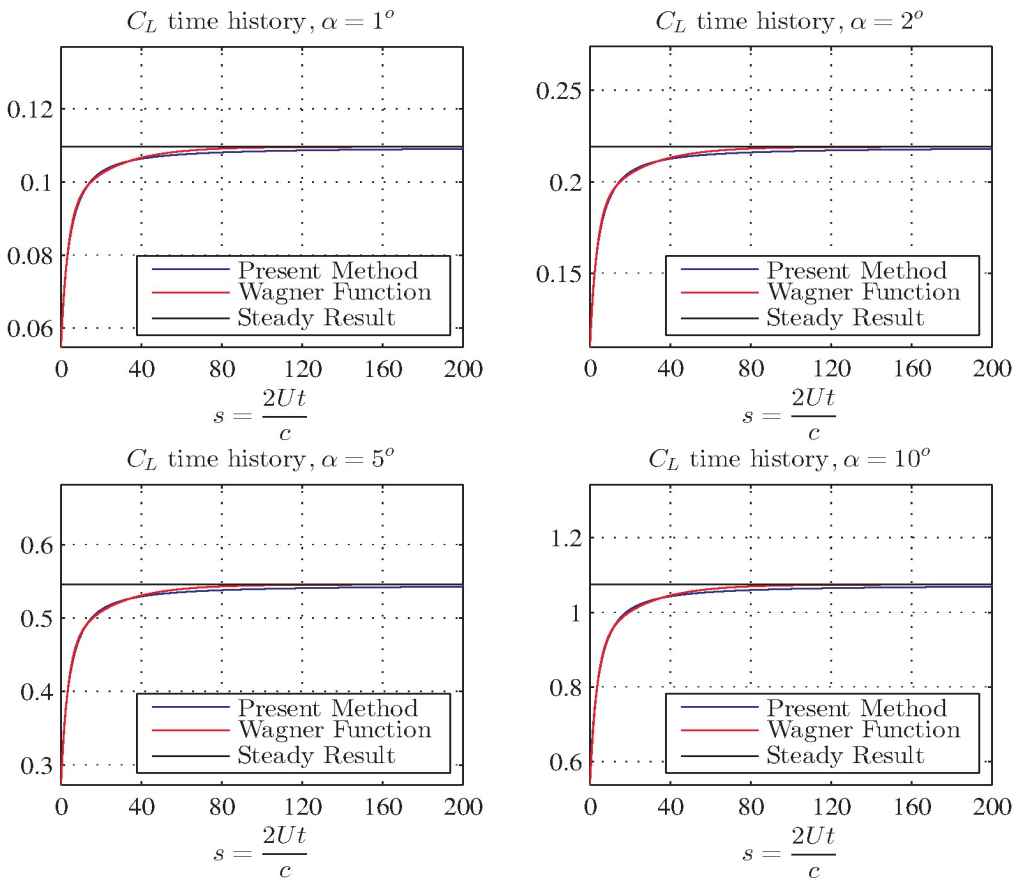

Figure 3.5: Comparison of time histories with prediction by Wagner's function

According to the steady-state analytic result concerning the vorticity distribution is given by the expression (Moran, 1984)

$$\gamma(x) = 2U\sqrt{\frac{c-x}{x}} \cdot a \tag{3.2.4}$$

From the fact that the prediction of the moment coefficient (Fig.3.3) is not as well predicted as the lift coefficient (Fig.3.2) we conclude that t the vorticity distribution is not accurately represented by the present method for small numbers of chord elements (coarse discretization).

In Figure 3.6 the vorticity distribution approximations for 10, 20, 50, 100 chord elements are given for four values of the angle of attack when the steady – state is reached and are compared to the analytical result Eq. (3.2.4). Note that in this figure only the first $1/10$ of the chord length is shown, where the vorticity distribution has the most significant variations. We see that increasing the number of chord elements the resulting vorticity distribution weakly converges to the analytic result.

Finally in Fig.3.7 we present results for the steady – state lift and moment coefficient over a range of angles of attack. The results for the lift coefficient are compared with results from a steady low – order panel method based on Hess & Smith BEM (see Moran 1984), in the case of a very thin NACA 0001 hydrofoil.

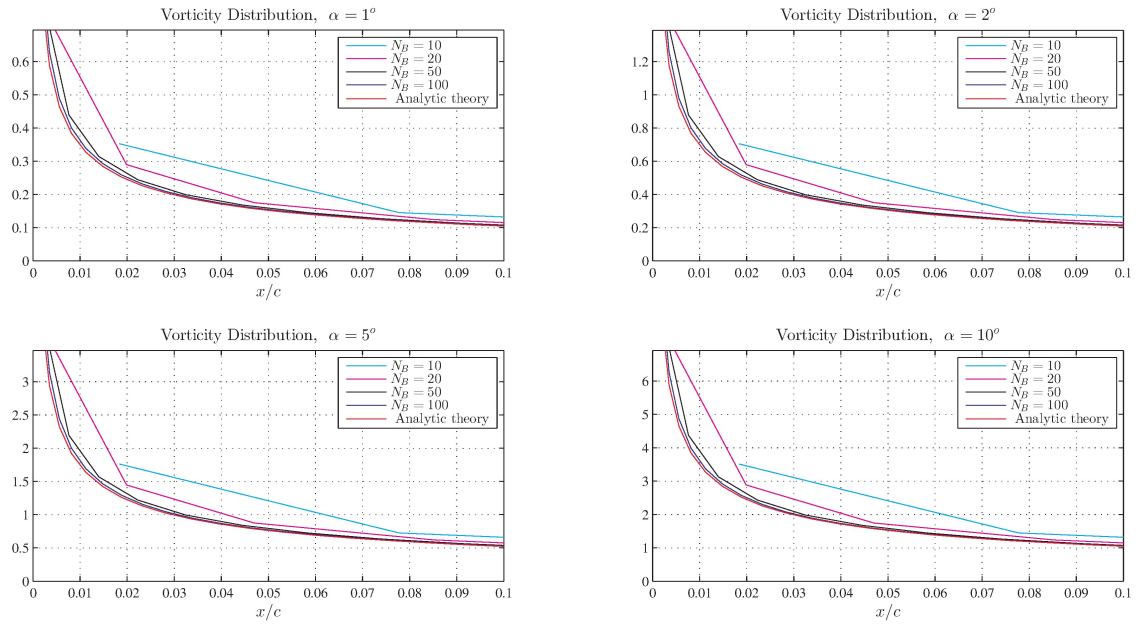

Figure 3.6: Vorticity distribution for flat plate at constant angle of attack

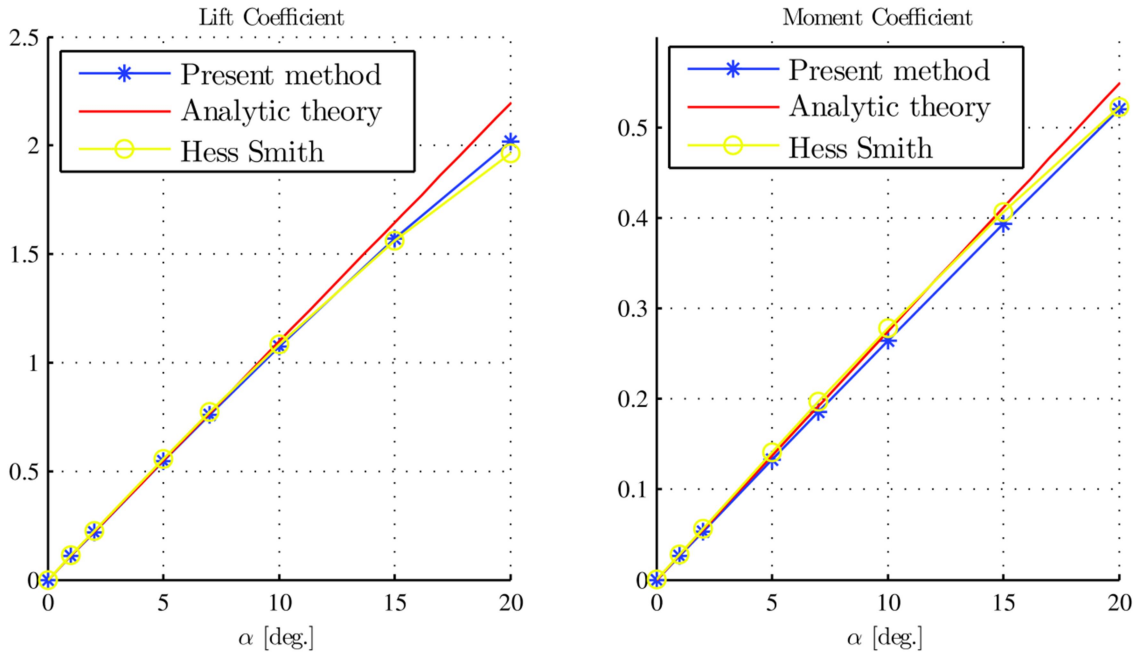

Figure 3.7: Steady results for lift and moment coefficient. Comparison with Hess & Smith, analytic theory

The agreement of present DVM is very good with the panel method for all examined angles of attack. Small deviation between numerical methods and analytic theory results is observed as angle of attack becomes greater than about 10deg. This is attributed to the linearization of the analytic theory, in the treatment and approximation of the boundary condition and its transfer from the exact boundary on the cut (see, e.g. Newman 1977, Chap.5.3).

3.3 Symmetric foil in unsteady motion – Convergence study

Next, we will present results of a symmetric foil performing unsteady periodic flapping motion, comprising of simultaneous heaving and pitching motions, which will also be separately investigated. First we try to establish the convergence characteristics of the DVM. We perform runs for a range of flapping motion parameters, e.g. heaving/pitching amplitudes and reduced frequencies or Strouhal numbers. The phase angle between the heaving and pitching motions is set to $\psi = 90^o$.

To start with, we define a parameter that controls the temporal discretization of the flapping foil problem solution. We set

$$TSR = 100 \cdot \frac{\Delta t}{T}, \tag{3.3.1}$$

short for *Time Stepping Ratio*. In Eq. (3.3.1) T denotes the period of the flapping motion. The parameter that controls the space discretization is the number of panels N_B on the foil.

We will study the convergence characteristics of the flapping foil problem in two separate ways; first we set TSR = 1 and systematically change N_B. The foil is then subject to three sets of flapping motion parameters $h_0/c, \theta_0, St$. The numbers of chord elements used are 10, 20, 50, 75, 100. For each run we calculate the lift and thrust coefficients and present the relative error with that acquired with 100 chord elements. The results are illustrated in Figure 3.8.

The lift and thrust coefficients display good rate of convergence, with the relative error reducing as the number of chord elements N_B increases. In all three cases tested the relative error has dropped below 2% for 50 chord elements, while for 75 chord elements convergence (error below 0.1%) has been practically achieved.

Next we fix the number of chord elements at $N_B = 100$ and modify the TSR to study the convergence of the DVM when temporal discretization gets finer. The lift and thrust coefficients' values are calculated for TSR = 0.1, 1, 2, 5, 10, which means that the time steps

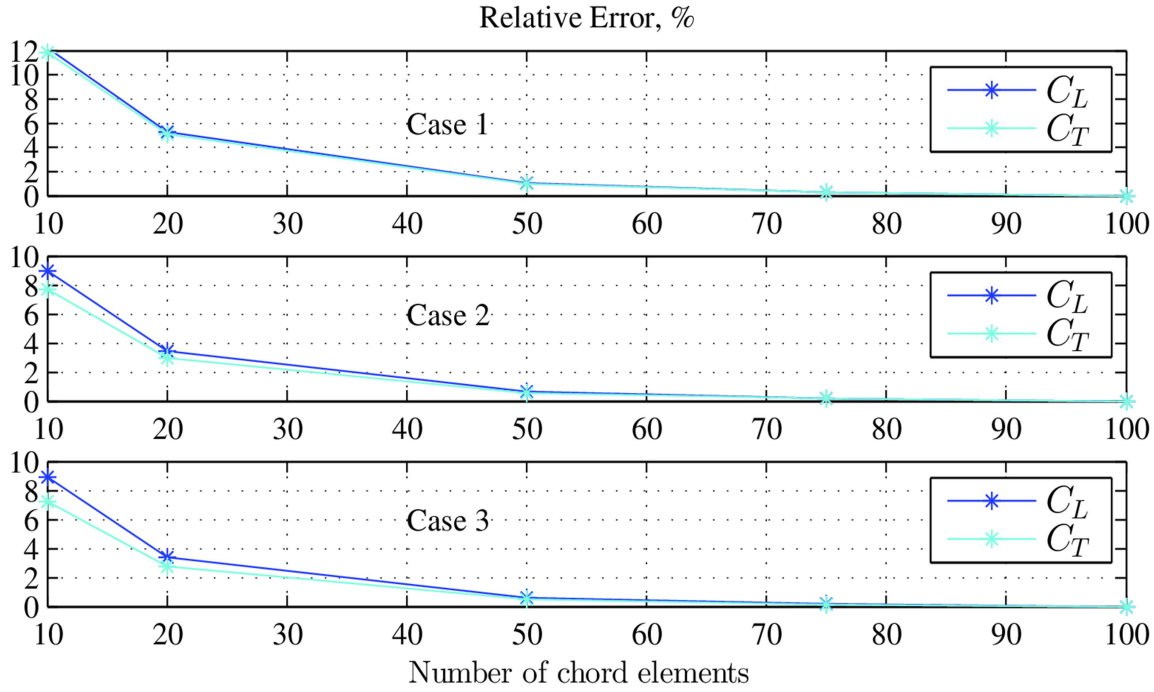

Figure 3.8: Flapping foil convergence study with fixed TSR and modifying number of chord elements. Case 1: , Case 2: , Case 3:

per period used are 1000, 100, 50, 20, 10, respectively. The results are shown in Figure 3.9. As the time discretization gets finer, the relative error decreases, as expected.

The results of the convergence study lead us to the obvious consideration that there exists an optimum relationship between the space and time discretization in the DVM in order for the numerical results to exhibit convergence. We define the following non-dimensional parameter;

$$\lambda = \frac{U\Delta t}{\Delta x_{TE}}, \tag{3.3.2}$$

which is the ratio between the wake panel length over the foil panel length at the trailing edge region. We performed tests for a range of flapping parameters where the number of foil panels N_B and TSR were systematically varied from 10 to 200 and 0.03 to 1, respectively. The relative error of the value for the thrust coefficient was calculated for each approximation, with the value for the finest discretization (N_B = 200 and TSR = 0.03) serving as reference. The results are shown in Figure 3.10, where iso – λ curves are shown by using solid lines.

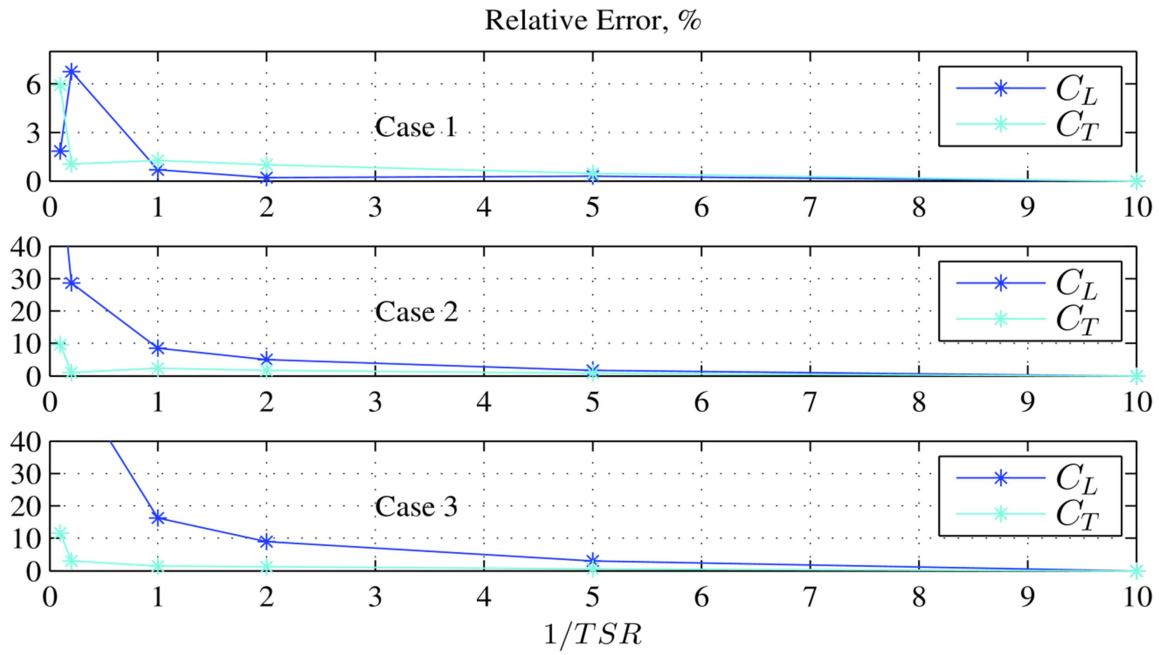

Figure 3.9: Flapping foil convergence study with fixed NB and modifying TSR. Case 1, Case 2, Case 3; as in figure 3.8

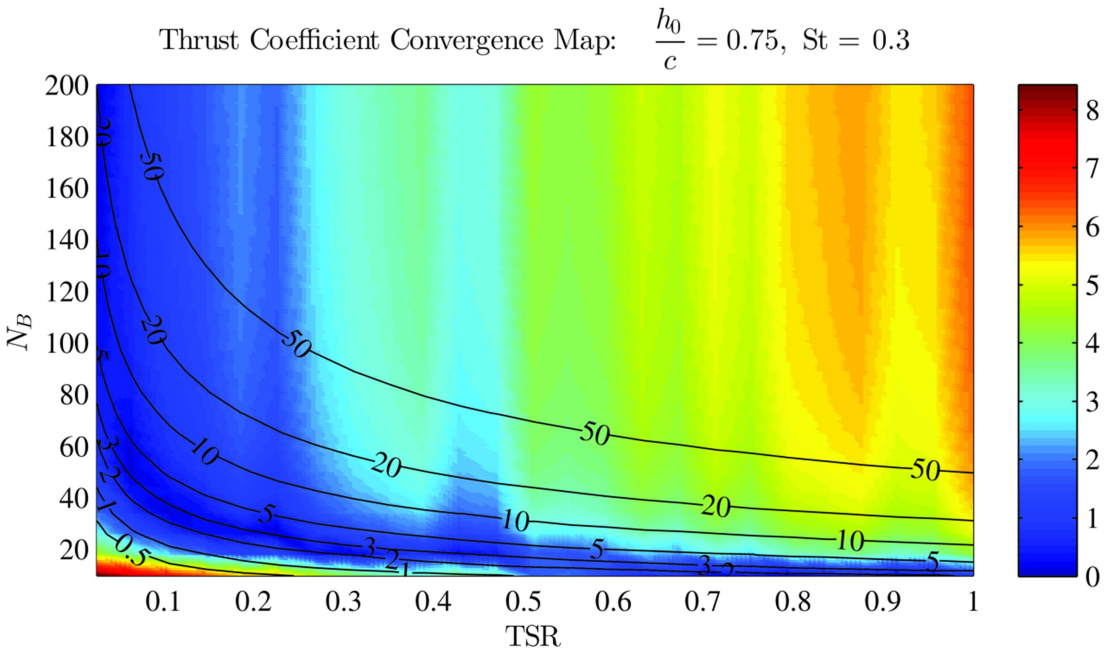

Figure 3.10: Map of convergence error

From Fig.3.10 and experience from similar cases it is evident that the values of λ that lead to relatively fast convergence of the thrust coefficient are approximately between 2 and 5. The values used in this work henceforth are in this interval. In the present work, the TSR and λ are input values by the user which means that N_B is accordingly constrained. To avoid very high N_B (leading to increased run time) or very low N_B (leading to insufficient vorticity distribution representation) the λ parameter should take values in the suggested interval.

3.4 Symmetric foil in heaving motion

We begin by showing results of the DVM for unsteady motions in the case of pure heaving, (or plunging) motion. The foil is considered to be symmetric and of negligible thickness, subject to a constant potential free – stream flow with velocity magnitude U while performing a simple oscillatory heaving motion about its mean position. The problem of a heaving flat plate allows for an analytic solution expressed by the Theodorsen function (Newman, 1977).

$$C(k_r) = \frac{H_1^{(2)}(k_r)}{H_1^{(2)}(k_r) + iH_0^{(2)}(k_r)}, \tag{3.4.1}$$

where $H_m^{(2)}(k_r)$ is the Hankel function of m-order and second kind. We will present results for the lift coefficient, which according to the linear theory is equal to

$$C_L(k_r) = 2\pi k_r \frac{h_0}{c} \left| -2iC(k_r) + k_r \right| \tag{3.4.2}$$

The Theodorsen function is complex – valued and models the wake memory effects. It is thus expected that as the reduced frequency decreases, its value gets close to unity. Its other limiting value occurs when the reduced frequency increases and is equal to 0.5. Its Argand diagram is shown in Figure 3.11.

Focusing on small values of $k_r \to 0$, it is easily seen that the above result is also compatible with the steady analytic theory result $C_L = 2\pi\alpha$, where $\alpha \approx 2k_r h_0 / c$.

The DVM is applied to heaving motion with amplitude $h_0 / c = 0.05, 0.1, 0.2, 0.4$ and reduced frequency varying between 0.1 and 1.8. The simulation time was equal to the time needed for the foil to travel 30 chord lengths or 5 motion periods, whichever is higher. The results are shown in Figure 3.12 for unit chord length. The maximum Strouhal number is equal to about 0.45. The DVM shows great agreement with the analytic theory results for small motion

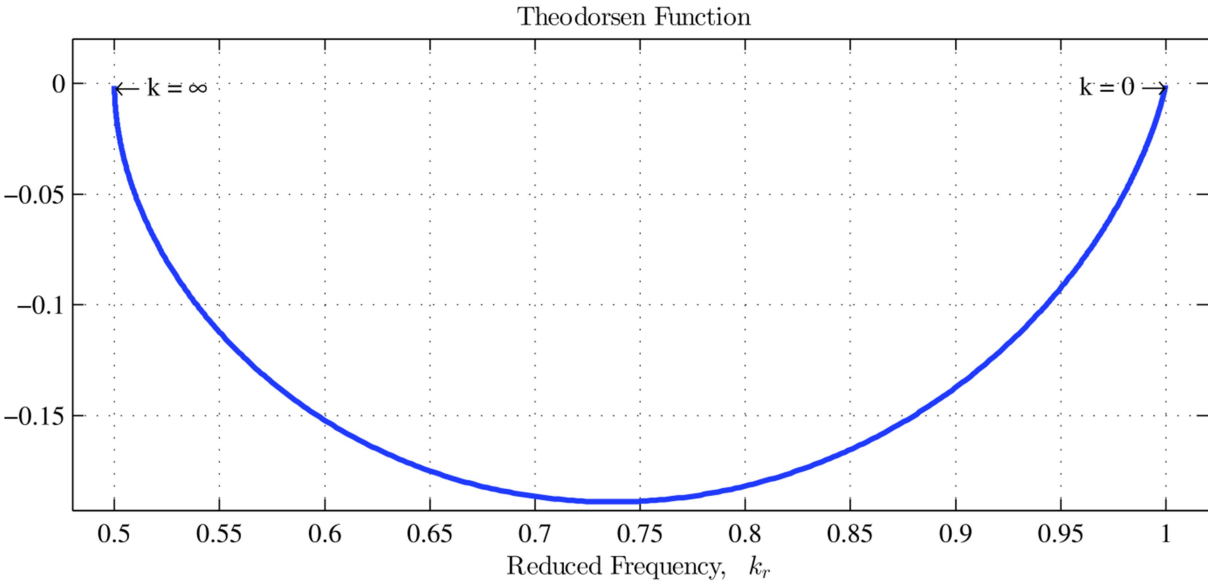

Figure 3.11: Theodorsen function

amplitudes in the whole frequency range tested. As the heaving amplitude increases, the DVM produces larger lift coefficient results, a trend which becomes more clear as the reduced frequency increases. This observation lies in the fact that the wake geometry displays a significant deviation from the linear one assumed by the linear theory, and thus the Theodorsen function cannot accurately describe the foil response.

The deviation from the linear theory results is evident not only in the lift coefficient amplitude, but in the phase and time history as well. In Figure 3.13, for a rather large value of $k_r = 2$ and moderate heaving amplitude we present the time history of the lift coefficient for and compare with linear theory. In this case, the DVM predicts a more complicated time history, clearly possessing higher harmonics. The differences are essentially due to the sinusoidal wake geometry and will be investigated in more detail below in Sec.3.8.

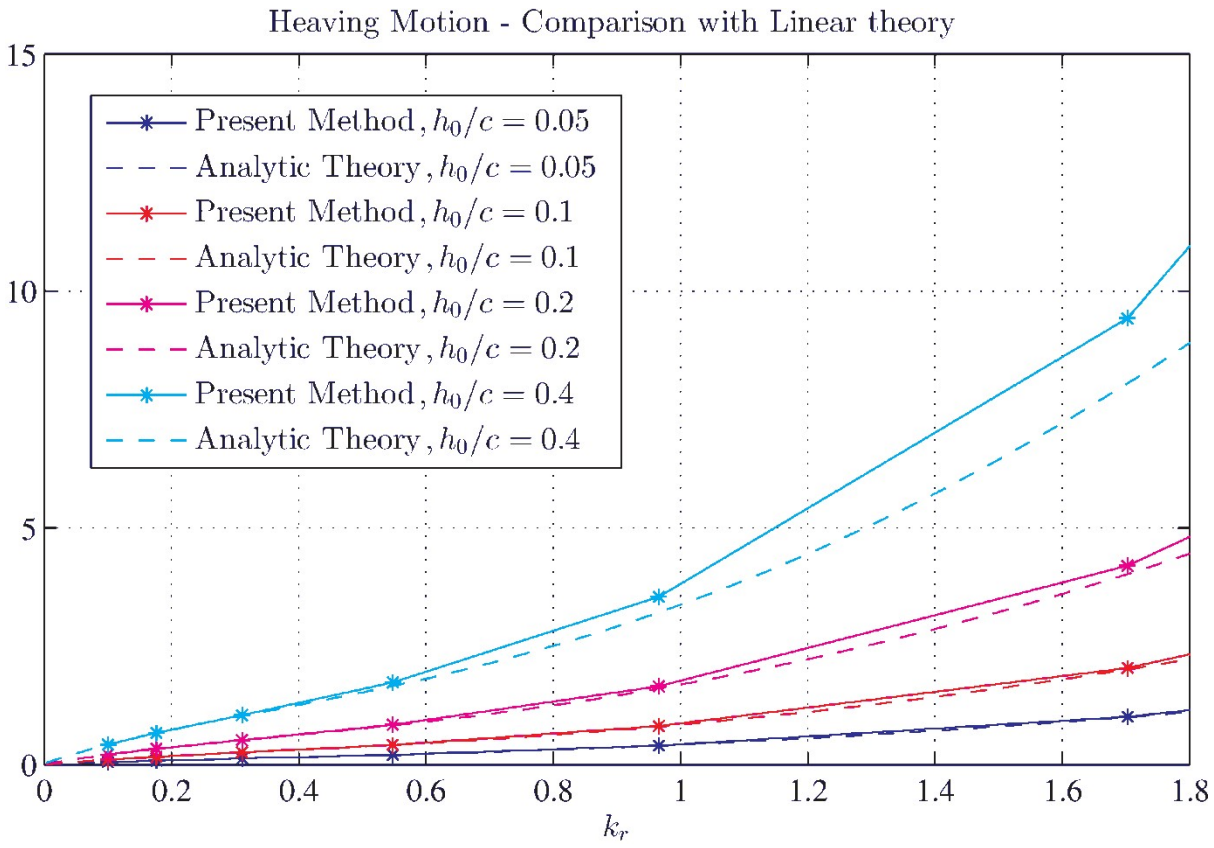

Figure 3.12: Lift Coefficient - Heaving motion

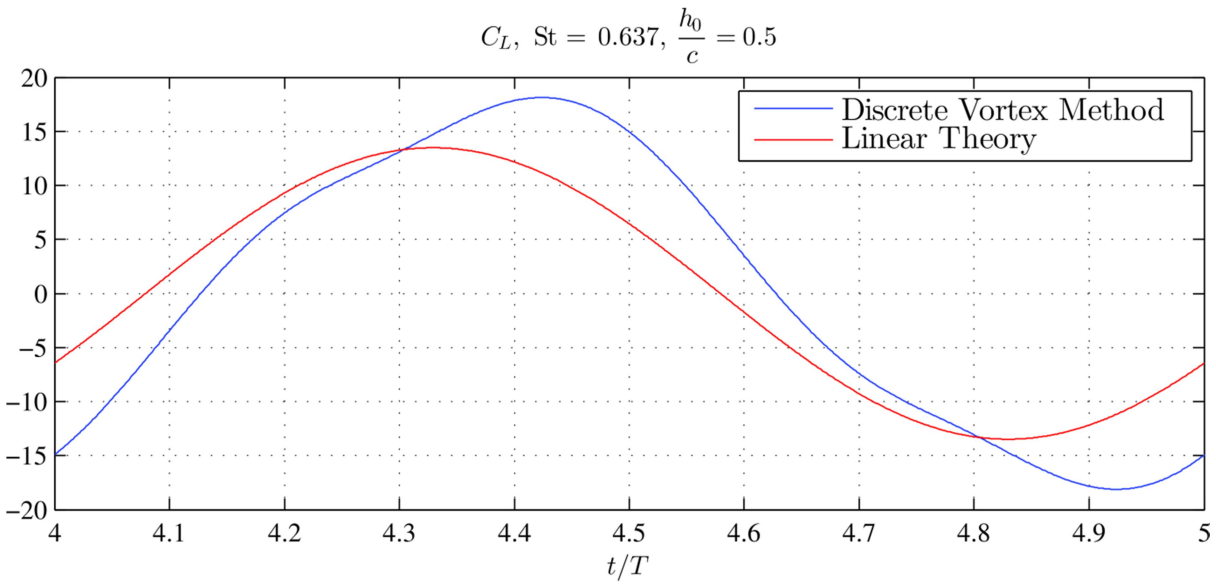

Figure 3.13: Comparison of lift coefficient time history with linear theory – high frequency heaving motion

3.5 Symmetric foil in pitching motion

Next we study the performance of a symmetric foil of negligible thickness in harmonic pitching motion, given by Eq.(3.1.2). This problem can also be treated in the scope of linear theory, assuming infinitesimal pitching amplitudes. The result for the lift coefficient is also given by an expression containing the Theodorsen function (3.4.1). The corresponding expression is

$$C_L(k_r) = 2\pi\theta_0 \left| \left(1 + \frac{1}{2} ik_r\right) \cdot C(k_r) + \frac{1}{2} ik_r \right|, \tag{3.5.1}$$

similar to Eq. (3.4.2). Again, compatibility of the above equation with steady theory result is evident for small values of $k_r \to 0$.

In order to study the performance of the DVM in pitching motion we ran simulations for $\theta_0 = 1^o, 2^o, 5^o, 10^o$ and reduced frequencies varying between 0.1 and 3. The pivot axis is placed at the mid – chord. The rest of the simulation parameters are the same as in the case of

heaving motion. The results are shown in Figure 3.14, where the results of the linear theory are indicated by using dashed lines.

The results for the lift coefficient for pitching motion show the same trend as for heaving motion. The DVM shows very good agreement with the linear theory, even for large values of k_r, with deviations becoming evident only for the largest pitching amplitude and k_r=3. As the reduced frequency further increases, the differences between linear theory and DVM become significant as, for example, presented in Figure 3.15. The DVM predicts a more complicated time history clearly containing a second harmonic which the linear theory by default cannot reproduce. This deviation is due to both the high pitching motion amplitude and the high value of reduced frequency, similarly as in the pure heaving motion case presented in Figure 3.13.

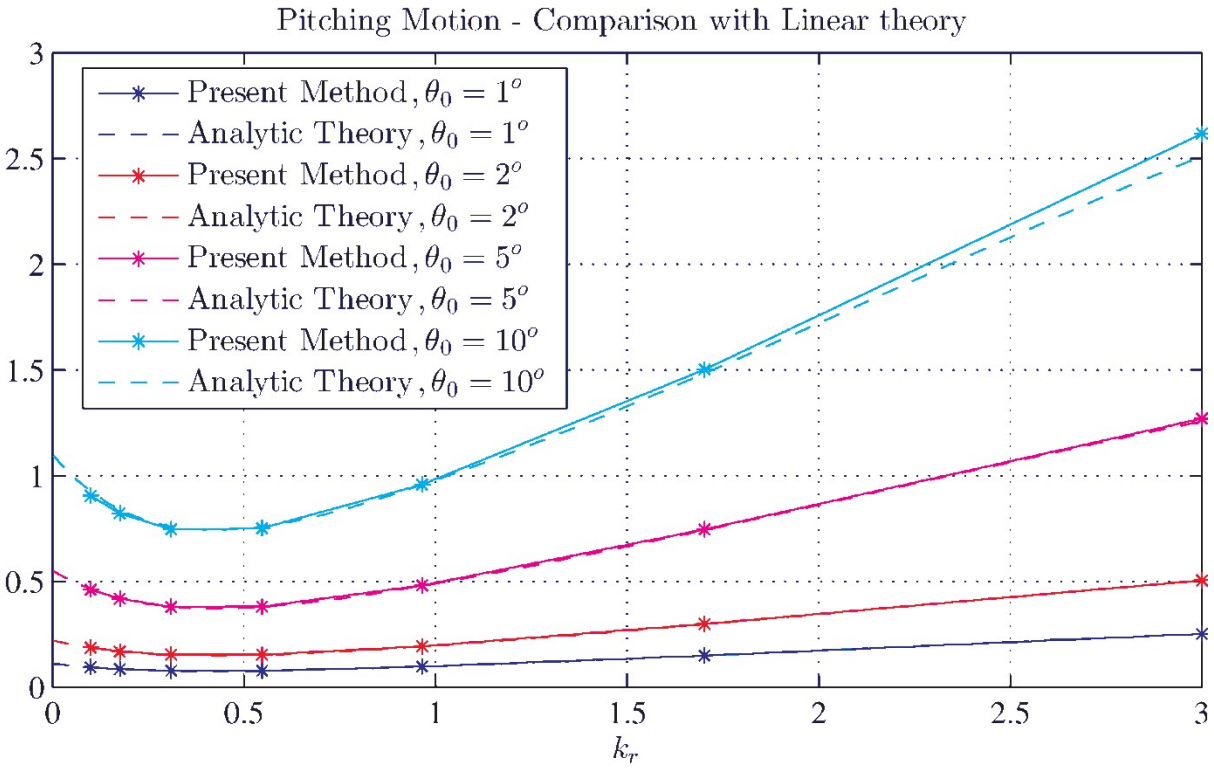

Figure 3.14: Lift Coefficient – Pitching motion

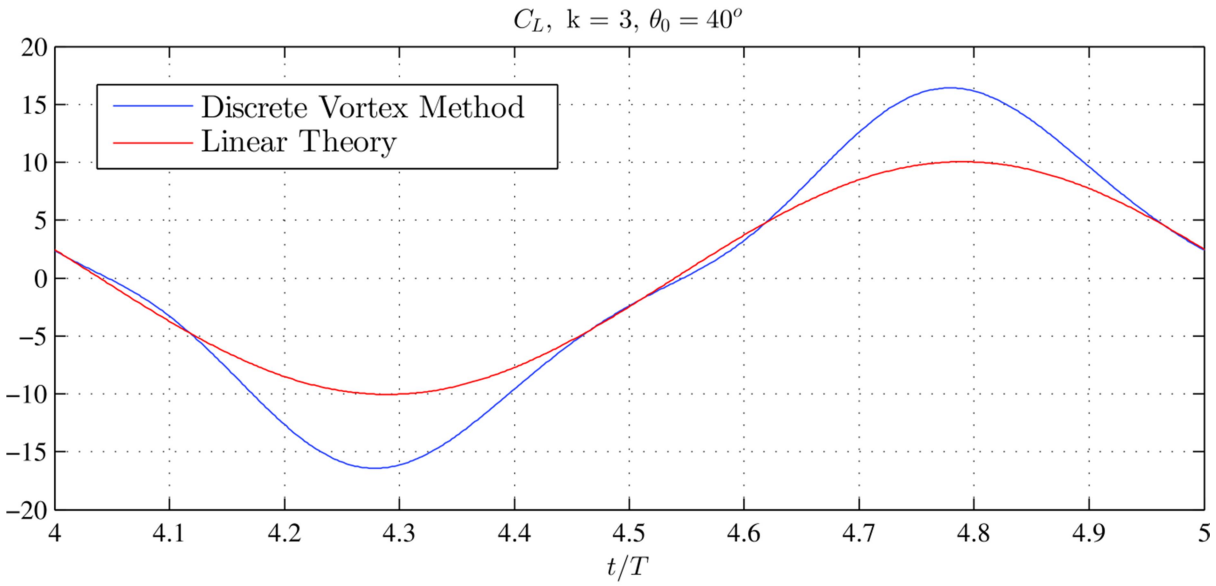

Figure 3.15: Comparison of lift coefficient time history with linear theory –high frequency pitching motion

3.6 Symmetric foil in flapping motion

Combining the heaving and pitching motions with phase difference around 90deg flapping foil motions are generated. This is the motion that many aquatic animals perform with their tails, while in some species a large portion of the body takes part (see Fig 1.1). It has been both theoretically and experimentally demonstrated that the flapping motion is thrust producing with high performance, under proper selection of the flapping parameters. In this section we will present results from the DVM concerning flapping motion configurations and compare the results with those predicted by the linear theory.

The heaving and pitching motions are described by relations (3.1.1), (3.1.2). The phase lag between heaving and pitching is set equal to 90^o, while the pivot axis is placed at the mid – chord. To obtain the analytic theory result for the amplitude of the lift coefficient in the case of flapping motion we simply superpose the results for the heaving and pitching motions. Thus, the formula for the lift coefficient is

$$C_L\left(k_r\right)=\left|-4\pi i k_r \frac{\overset{o}{h}_0}{c}\cdot C\left(k_r\right)-2\pi i^2 {k_r}^2 \frac{\overset{o}{h}_0}{c}+2\pi\left(1+\frac{1}{2}ik_r\right)\overset{o}{\theta}_0\cdot C\left(k_r\right)+\pi i k_r \overset{o}{\theta}_0\right| \tag{3.6.1}$$

where the phase difference is $\psi=\arg\left(\overset{o}{h}_0\right)-\arg\left(\overset{o}{\theta}_0\right)$.

We perform numerical simulations for heaving amplitudes $h_0/c=0.05, 0.1, 0.2, 0.4$ and pitching amplitudes $\theta_0=1^o, 2^o, 5^o, 10^o$, while the reduced frequency is varied between $k_r=0.1$ and $k_r=2$. The results for the lift coefficient obtained are presented in Figure 3.16, along with those predicted by Eq.(3.6.1).

The results are in agreement with those already observed for heaving and pitching motion. As the motion amplitudes increase the deviation of DVM from linear theory is amplified. Differences are attributed to the sinusoidal wake effects and the approximation of coupled heaving and pitching motion in the no – entrance boundary condition by the linear theory. In Figure 3.17 a time history of the lift coefficient is presented for a large – amplitude and high – frequency case. The time history of the lift coefficient as predicted by the DVM is non – symmetric due to a higher harmonic that is out of phase with the main harmonic corresponding to the flapping motion frequency.

3.7 Symmetric foil in sinusoidal background gust

In this section the presence of a non – uniform background flow field is considered. This flow field is a sinusoidal gust transverse to the foil's mean forward motion. Thus, it effectively changes the angle of attack causing the forces on the foil to become unsteady. A practical example of a sinusoidal background velocity is a propeller's blade operating in the wake of the ship. The assumption of the sinusoidal gust is a simple way to approach this very difficult problem. Another example would be a hydrofoil ship operating in waves, where its lift – producing components are subject to free – surface effects.

The sinusoidal velocity gust is described by the following expression in the inertial frame of reference (moving with the foil mean forward travelling speed)

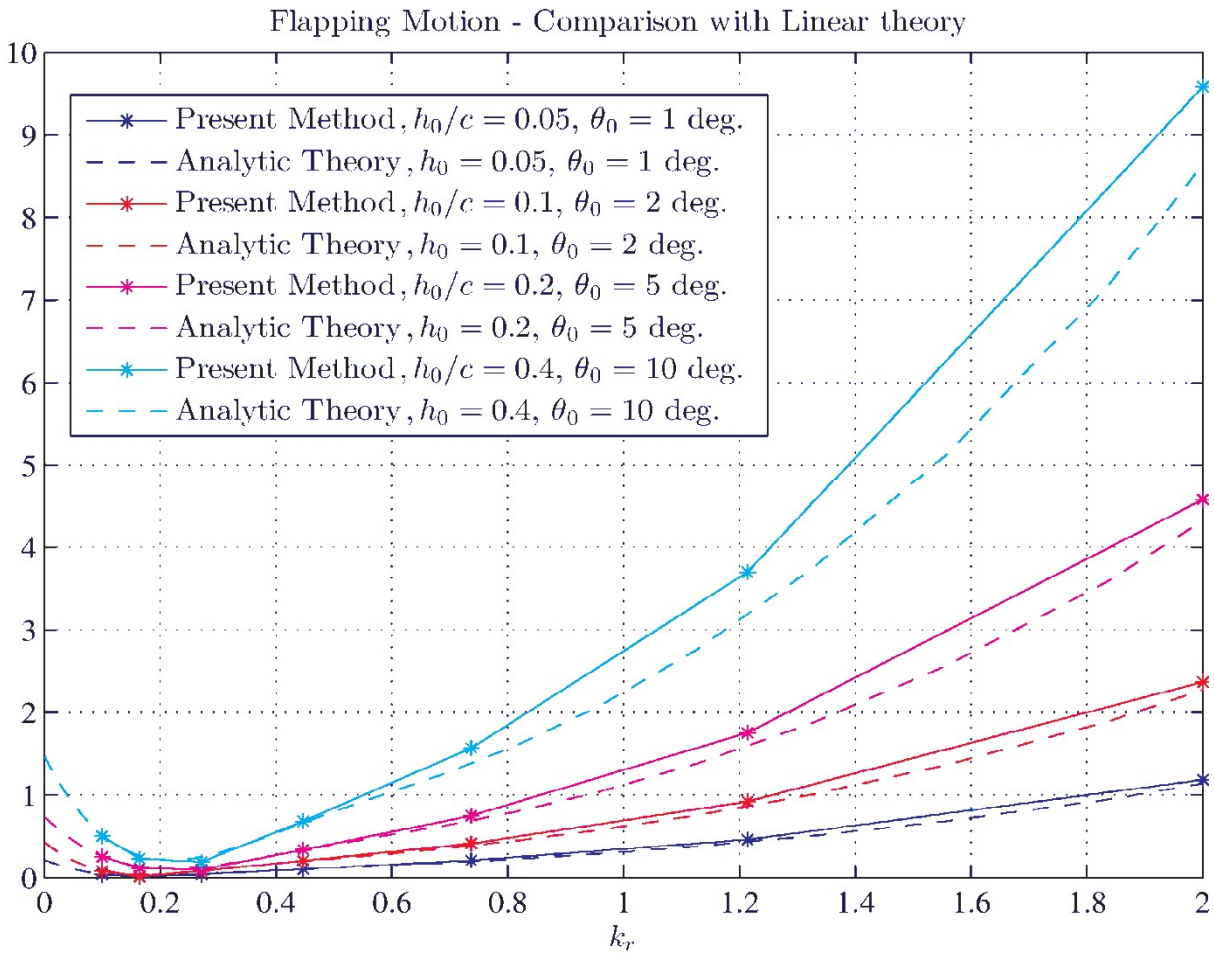

Figure 3.16: Lift Coefficient – flapping motion

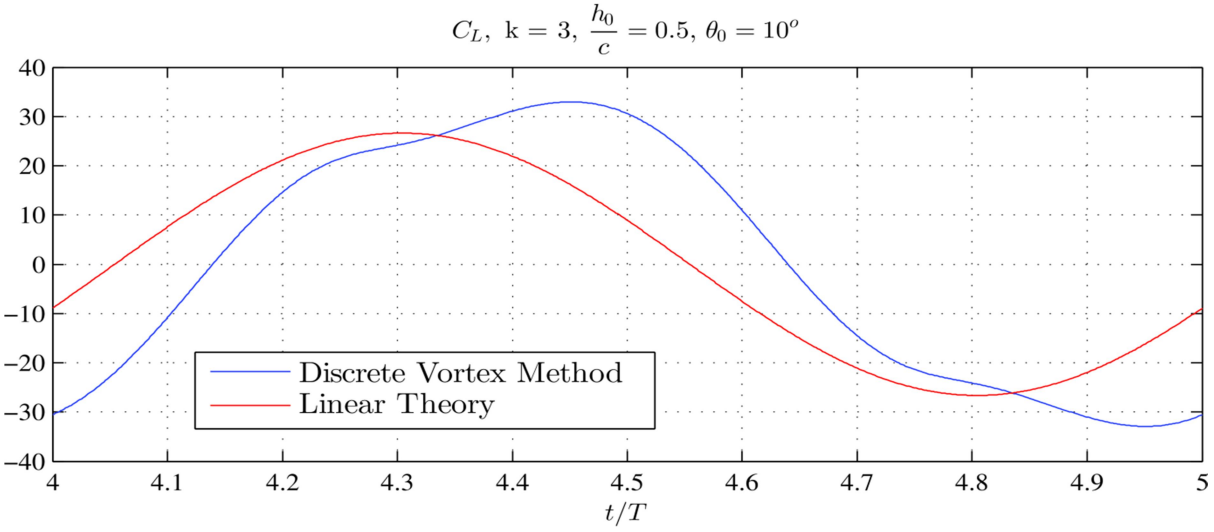

Figure 3.17: Comparison of lift coefficient time history with linear theory –high frequency flapping motion

$$V_g = U_g \cdot \cos\left(g_k x - \omega t\right). \tag{3.7.1}$$

In the case where the gust is stationary in the earth-fixed frame of reference $g_k = 2k_r / c$ implying that the celerity of the gust (with respect to the above inertial steadily travelling frame of reference) is equal to the free – stream velocity U , since $C = \omega / g_k = \omega c / 2k_r = U$ by virtue of the reduced frequency definition. In this work we consider only such cases, however extension of the present model to the more general case of wave-like gusts, representing the effects of waves on flapping foils (see, e.g., Belibassakis & Politis 2013, Filippas & Belibassakis 2014) is straightforward.

The problem of a foil travelling with a constant velocity in a sinusoidal background velocity field assumes an analytical solution for the lift coefficient;

$$C_L\left(k_r\right) = 2\pi \frac{u_g}{U} \cdot S\left(k_r\right) \tag{3.7.2}$$

where $S\left(k_r\right)$ is the Sears function (see Newman 1977) defined in terms of the Hankel functions of the second kind by the expression

$$S\left(k_r\right) = \frac{2i}{\pi k_r} \frac{1}{H_1^{(2)}\left(k_r\right) + iH_0^{(2)}\left(k_r\right)} \tag{3.7.3}.$$

The Sears function is complex valued. Its Argand diagram is shown in Figure 3.18. It naturally assumes the value 1 for very small frequencies, which again brings the above result given by Eq. (3.7.2) to agree with the steady result. The Sears function tends to zero for large frequencies (large k_r), with rapid variation of its phase due to the denominator oscillating proportionally to e^{-ik_r} .

We perform numerical simulations for a symmetric foil of negligible thickness in constant motion through a fluid with sinusoidal velocity field. The TSR is equal to 0.02, which is a very low value. The gust amplitudes tested are $U_g / U = 0.05, 0.1, 0.2, 0.4$ and the reduced frequency is varied between 0.1 and 3. The results for the lift coefficient amplitude are presented in Figure 3.19.

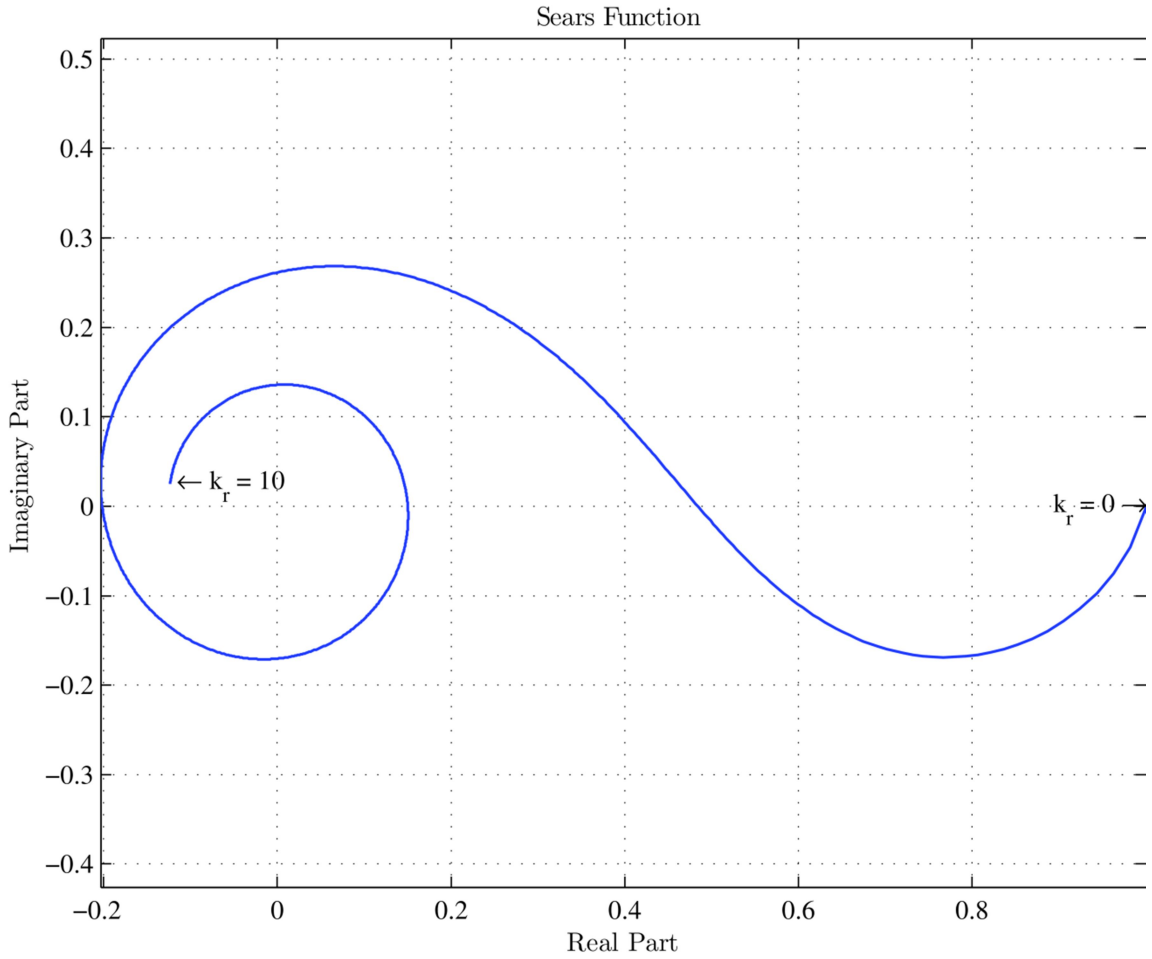

Figure 3.18: Sears function

The agreement of the DVM with the linear theory is very good, even for large amplitudes of the gust velocity where deviations were clearly observed for unsteady motions of the foil. This is attributed to the fact that in the case of background gust velocity the trailing vortex wake coincides with a straight line since it has been constrained to convect downstream with the free – stream velocity, as explained in detail in Chapter 2. The only source of unsteadiness is the harmonically varying normal to the foil velocity.

Non – linearities that occur due to wake geometry are not evident here as in the case of unsteady foil motion. Since the vorticity distribution depends linearly on the normal velocity and the trailing wake position, the hydrodynamic output of the foil motion in the velocity field in also harmonic with the same frequency. As a result non – harmonic time histories of vorticity, circulation and forces are not possible in this setup.

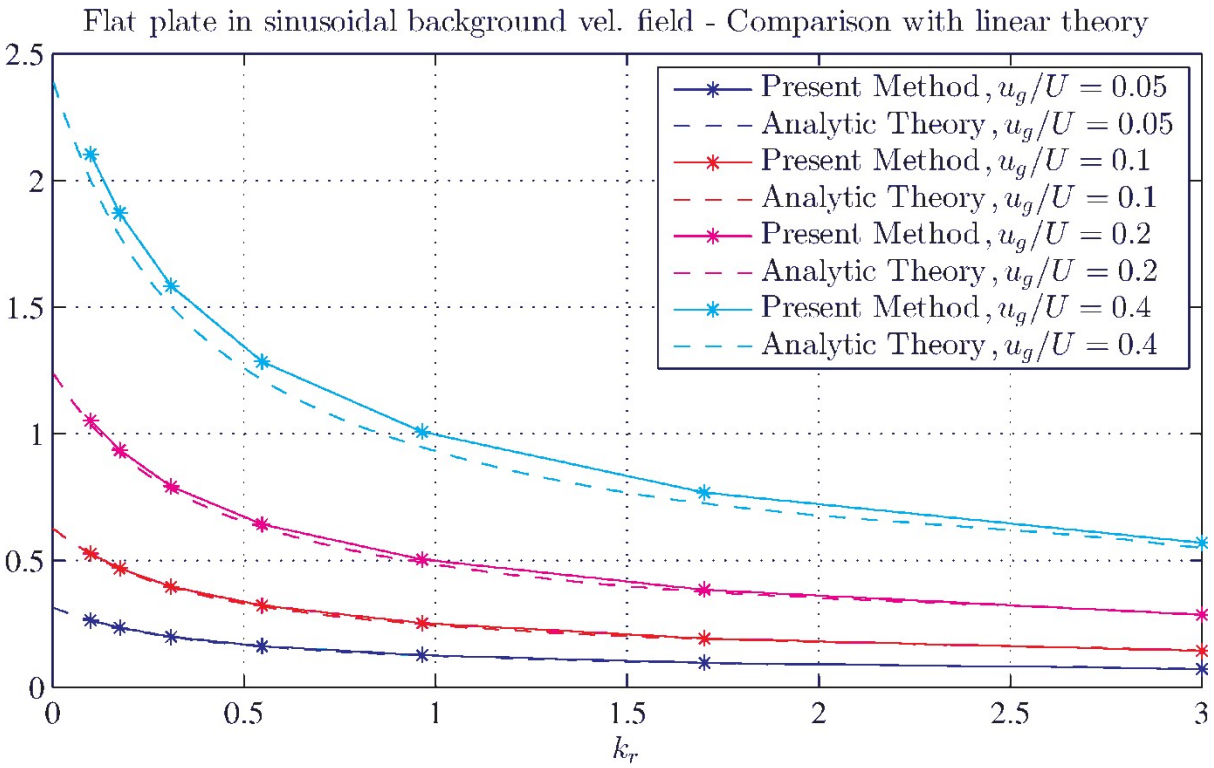

Figure 3.19: Lift coefficient – background gust velocity

3.8 Further investigation of the DVM results

Having established the convergence characteristics and the agreement of the DVM resuts with the linear theory we will proceed to further investigation accompanied by brief discussion.

3.8.1 Approaching steady results

A fundamental requirement for the numerical model to be valid is for it to be able to capture the results of the steady thin hydrofoil theory in both possible ways; as a limit of infinite chord lengths travelled after the foil starting its constant speed motion with a constant angle of attack and as a limit of a foil performing flapping motion with infinitesimal motion amplitudes. In the first case it has been shown in Sec. 3.3 that the DVM indeed captures the steady analytical theory result. Here we will attempt to run the DVM for decreasing values of

the reduced frequency and extrapolate the results for the lift coefficient to $k_r \to 0$, where it is impossible to apply the numerical model. To this end we perform numerical simulations for a flapping foil with $h_0/c = 0.1, \theta_0 = 5^o$ for values of reduced frequency varying in the interval $k_r \in \left[0, 10^{-1}\right]$. The TSR is set to 0.05 and λ to 2.5. The result of the lift coefficient is divided by the amplitude of the effective angle of attack as defined by Eq. (3.1.3).

For very small values of the reduced frequency numerical simulations are not actually possible, since the motion period becomes very large and the number of chord lengths required by the foil to travel in order to achieve steady – state is unrealistically large. In the present case we performed simulations for 7 values of the reduced frequency k_r logarithmically spaced between $10^{-1.5}$ and 10^{-1}. Therefore the smallest value of k_r for which we actually performed numerical calculations is 0.0316. In order to approximate the case for $k_r \to 0$ we fit the acquired data with a 3 – rd degree polynomial and extrapolate the results. The results are presented in figure 3.20. The fitting curve approaches the value 2π. This indicates that the presented model is compatible with the steady linear theory

3.8.2 Lift Hysteresis loop in the case of unsteady hydrofoil

The flapping foil motion results in a periodic effective angle of attack and lift coefficient time history, after some duration from the starting time, when a sufficient number of chord lengths has been travelled by the foil's and the starting vortex no longer affects the flow around it. In order to study the effect of non – dimensional parameters to the solution in terms of time – domain response (as opposed to essentially frequency domain response that has been already studied), we perform numerical simulations of flapping motion in a range of frequencies and present the phase portrait of instantaneous angle of attack – lift coefficient.

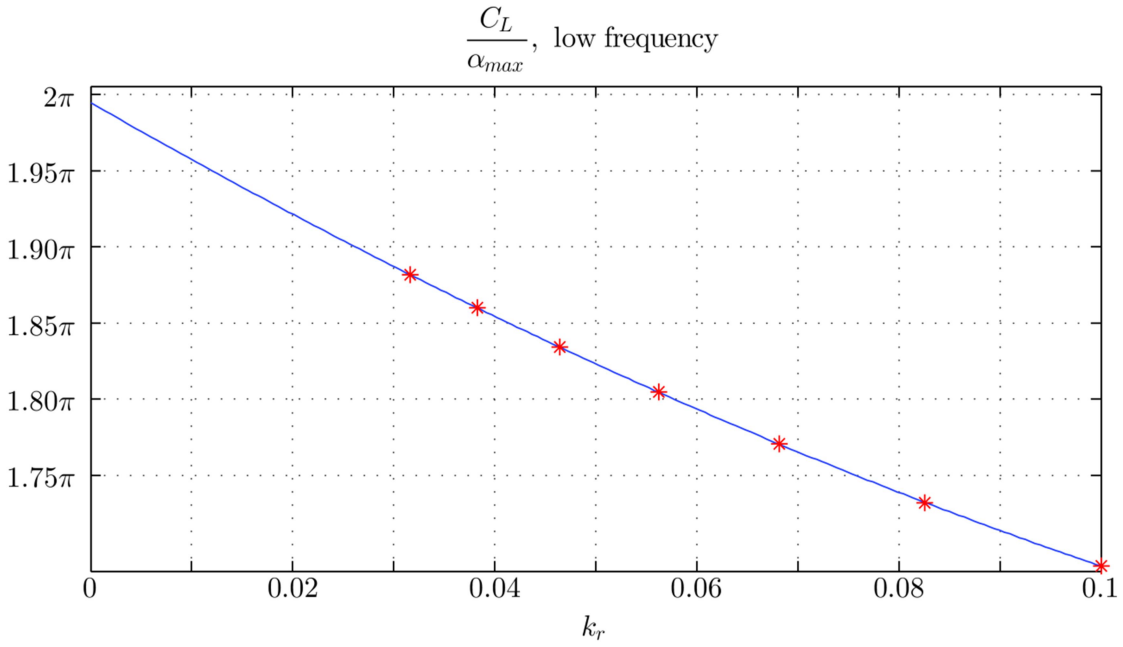

Figure 3.20: Flapping in low frequency. Red asterisks: results from DVM, Blue solid line: Data fitting

The results are presented in Figure 3.21, where the effective angle of attack profile is also shown.

The phase diagrams indicate a hysteresis loop, a characteristic of time – dependent systems. In the first case (St = 0.10) the hysteresis loop resembles an inclined ellipse around the steady case curve, which is a line with inclination $2\pi \cdot \frac{\pi}{180}$ (since the angle of attack is presented in degrees). The elliptical shape suggests that the response in this case in mainly linear. This observation is also associated with the time history of the effective angle of attack, which is predominantly sinusoidal, that is the $\tan^{-1}$ term in relation (3.1.3) has not yet deviated from its linear behaviour. In the second case (St = 0.20) the hysteresis loop slightly deviates from the elliptical one observed in the first case. This indicates that the system operates on the outskirts of the linear regime. The effective angle of attack profile is different than the sinusoidal one in the previous case, with a more flattened crest. In the third case (St = 0.40) the hysteresis loops

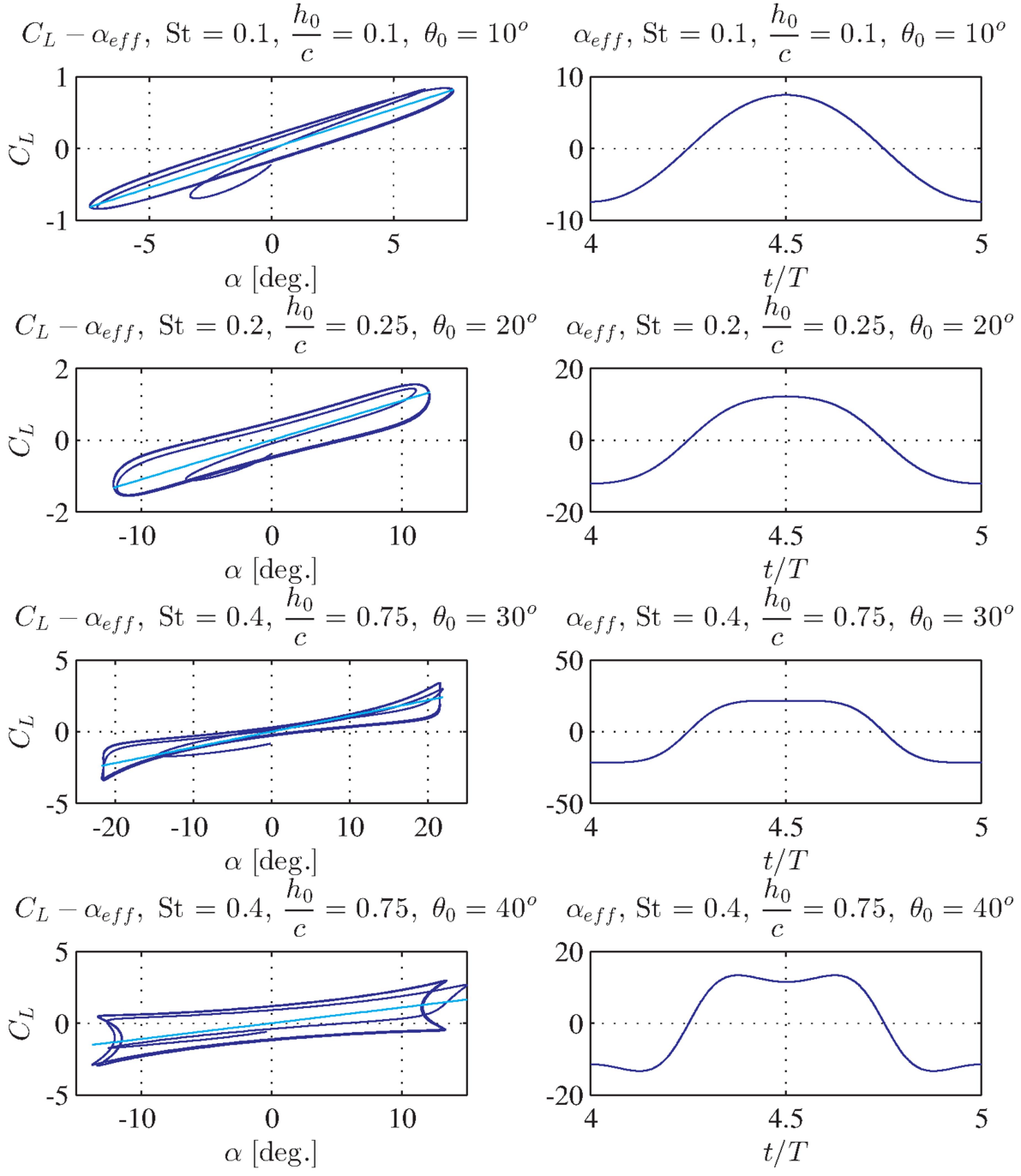

Figure 3.20: Phase diagram of (right column) and effective angle of attack time history for three flapping motion cases: , , and

significantly deviates from the ellipse in the first case. This is a trademark of the non – linear regime. The lift coefficient values attained for the extreme values of the effective angle of attack are larger than those predicted by linear theory. This can be explained by observing that the corresponding angle of attack profile has deteriorated and two crests are starting to

form. In this case the $\tan^{-1}$ term of the effective angle of attack has significantly deviated from the linear region of small arguments.

In the last case (St = 0.40), the maximum angle of attack is smaller than the third case but its profile is seriously degraded, possessing many peaks in a period of oscillation. The result is a hysteresis loop that is more complex than in the previous cases, with very sharp crests at the points where the direction of the system changes.

The effective angle of attack profile serves as an indicator of the efficiency of the flapping foil system in thrust – producing applications. Deformed profiles such as the one in the last case for St = 0.40 are generally characterized by poor efficiency. Read et al (2003) tried to alleviate this fact by appropriately modifying the heaving motion amplitude so that the effective angle of attack profile remains sinusoidal.

3.8.3 An in – depth analysis of the time histories of DVM

We will in this sub – section examine more closely the results of the DVM. We perform simulations for four kinematic setups:

- $h_0/c = 0.25, \alpha_{max} = 20^o, \quad St = 0.2$ (Case 1a)
- $h_0/c = 0.25, \alpha_{max} = 20^o, \ St = 0.4$ (Case 1b)
- $h_0/c = 0.75, \alpha_{max} = 30^o, \quad St = 0.2$ (Case 1c)
- $h_0/c = 0.75, \alpha_{max} = 30^o, \ St = 0.4$ (Case 1d)

Parameters $\psi = 90^o, \ x_R/c = 1/3$ in all cases. The simulation parameters are TSR = 0.05 and λ = 2.5, while the time duration of the simulations is equal to 5 motion periods. We display results for pressure difference coefficient, bound vorticity, lift coefficient, circulation and the satisfaction of the linearized Kutta condition (see Ch. 2).

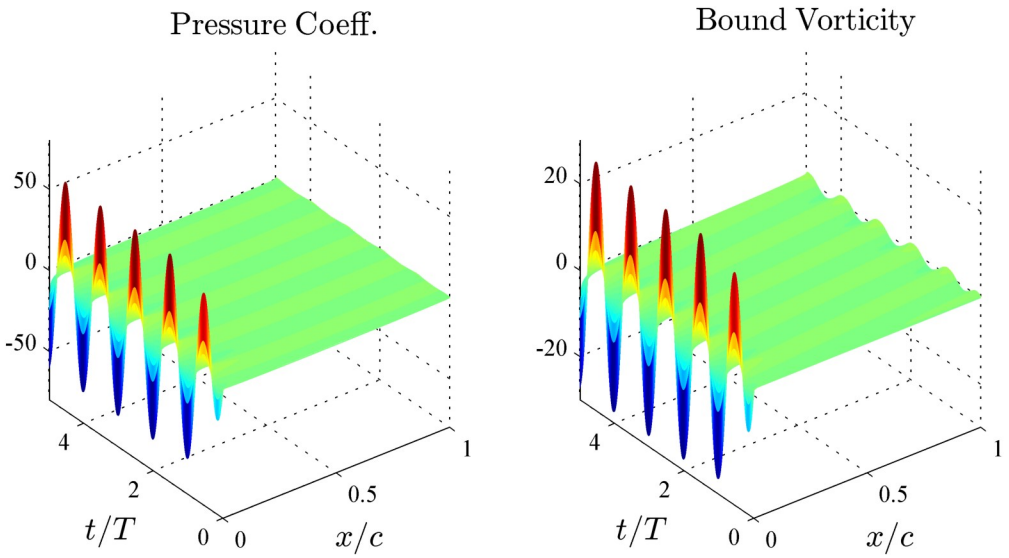

Figure 3.21: Case 1a; $h_0/c = 0.25$, $a_{max} = 20^o$, $St = 0.2$. Pressure coefficient & Bound Vorticity

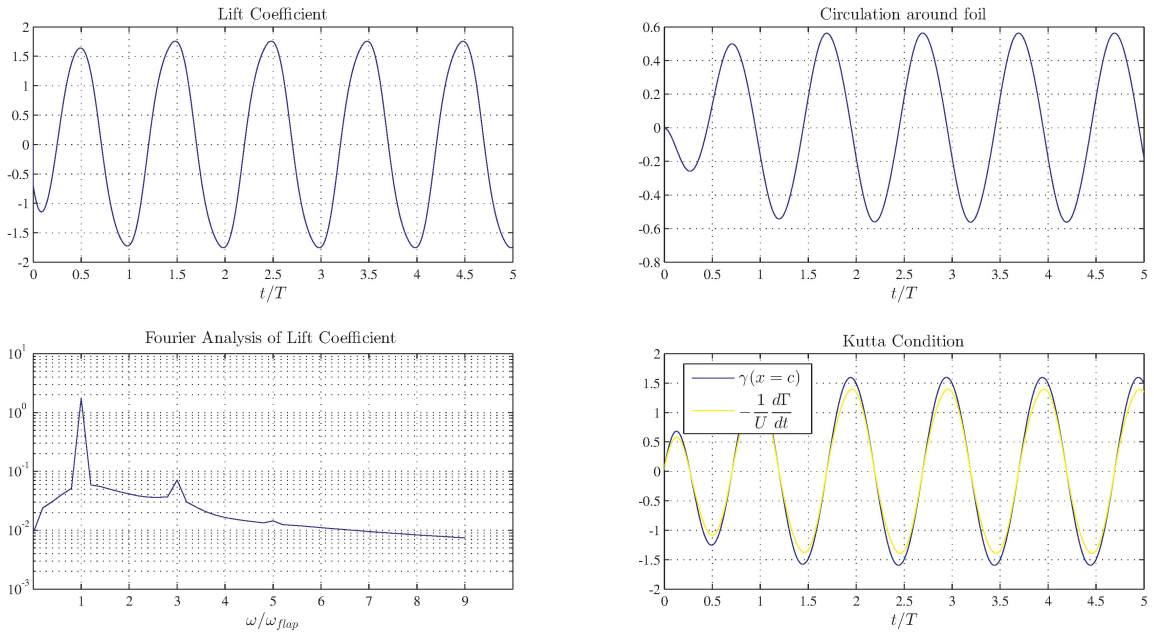

Figure 3.22: Case 1a; $h_0/c = 0.25$, $a_{max} = 20^o$, $St = 0.2$. Lift Coefficient, Circulation & Kutta condition

In Figure 3.21 the pressure coefficient and bound vorticity are presented as functions of chordwise position and time. Both quantities display the anticipated behaviour as $x \to 0$, in conformity with the linear theory. More specifically, the bound vorticity is characterized by an integrable square – root singularity at the leading edge region which results in the well –

known leading – edge suction force enforcing satisfaction of Kutta – Joukowski theorem in the steady case (Kerwin, 2001). The pressure coefficient assumes very small values towards the trailing edge region as expected, even though no pressure – type Kutta condition is enforced as we have already discussed in Ch. 2. We note that the vorticity distribution does not vanish at the trailing edge, as we expected by virtue of the application of Kelvin's theorem for unsteady foil motion.

Time histories of lift coefficient and circulation are displayed in Figure 3.22, for flapping case 1a. We have already discussed the time histories of C_L (upper – left figure). The lower – left figure presents a Fourier analysis of the lift coefficient time signal. The amplitude is shown in log – scale over a range of frequencies non – dimensionalized by the flapping frequency. The most significant peak of the response amplitude occurs exactly at the flapping frequency, as expected. However, two more peaks are observed; one at 3 times and one at 5 times the flapping frequency, negligible but certainly existing. Note that results concerning the response amplitude for frequencies that are not integer multiples of the fundamental (in this case, the flapping) frequency are not correctly represented by the Fourier Transform.

An explanation concerning the appearance of the above peaks can be provided in terms of the effective angle of attack, which is given by relation (3.1.4), repeated here for clarity

$$a_{eff}(t) = \tan^{-1}\left(-\frac{\dot{h}(t)}{U}\right) - \theta(t) \qquad (3.8.3.1)$$

The first term's series expansion contains only odd powers of its argument, the case for sinusoidal functions as well. Hence we can comprehend every term in its expansion as an odd – valued higher – order harmonic. This explains the peaks of the lift coefficient Fourier analysis.

In the lower right plot of Figure 3.22 the satisfaction of the linearized form of the Kutta condition is investigated. The blue line is the bound vorticity of the last chordwise panel on the foil, defined numerically as the ratio of the corresponding bound point vortex over the panel's length. The yellow line corresponds to the numerical evaluation of the circulation around foil time derivative. The two curves display the same quantitative characteristics, although there is a small deviation in amplitude probably due to the heuristic incorporation of the shed vortex position in the numerical model, defined in Eq. (2.4.3.5) in Ch. 2. However no violation is made as far as Kelvin's theorem is concerned, since the trailing vortex shed at each time instant is assigned the proper intensity in order to compensate for changes in the circulation around the foil.

In Figures 3.23 – 3.24 the results are displayed for Case 1b. The frequency in this case is twice that of Case 1a.

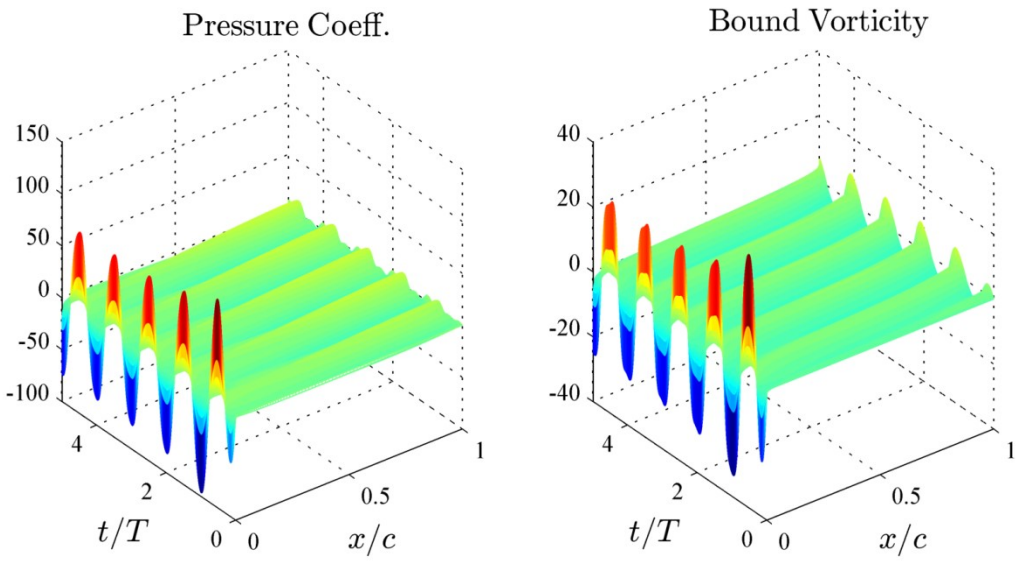

Figure 3.23: Case 1b; $h_0/c = 0.25$, $a_{max} = 20^o$, $St = 0.4$. Pressure coefficient & Bound Vorticity

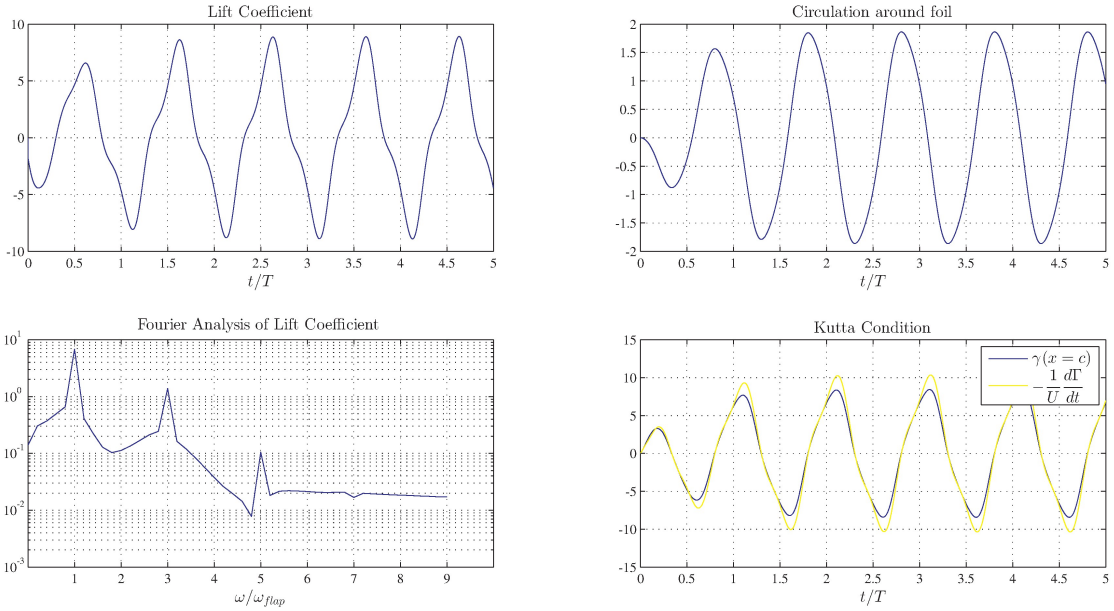

Figure 3.24: Case 1b; $h_0/c = 0.25$, $a_{max} = 20^o$, $St = 0.4$. Lift Coefficient, Circulation & Kutta condition

This case displays a significantly amplified unsteady behaviour compared to the previous one. In Figure 3.23 the pressure coefficient distribution envelope strongly deviates from the

steady case, possessing significant values for the most part of the chord length and very abruptly diminishing at the trailing edge region. Similar observations are made for the vorticity distribution, most notable of which are the large values attained in the trailing edge, indicating a very intense circulation change around the foil. The lift coefficient Fourier analysis shown in Figure 3.24 indicates that the third harmonic in the time signal is of the same order of magnitude of the fundamental harmonic.

In Figures 3.25 – 3.26 the results are displayed for Case 2a, where $h_0 / c = 0.75, a_{max} = 30^o, St = 0.2$.

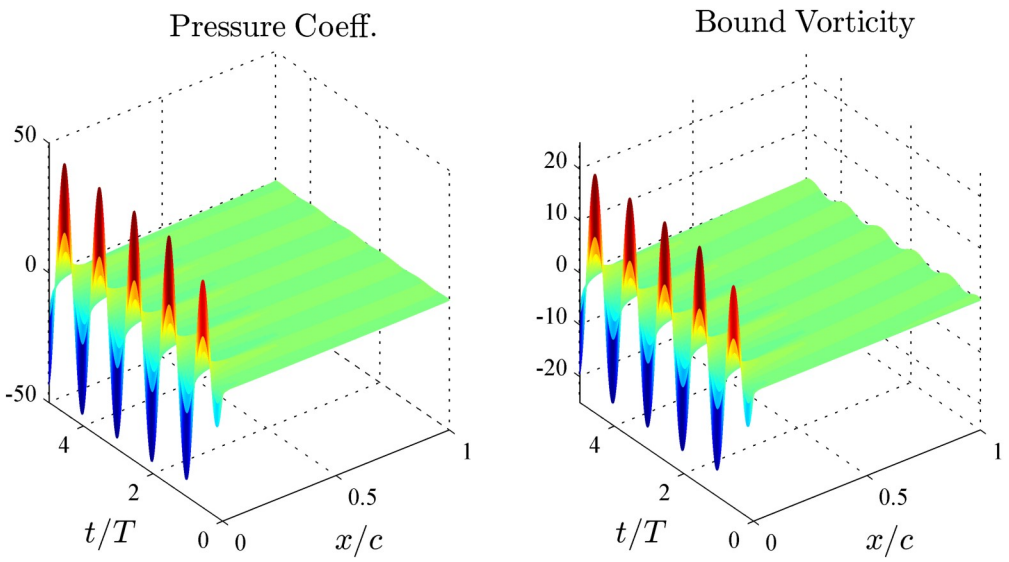

Figure 3.25: Case 2a; $h_0/c = 0.75, a_{max} = 30^o, St = 0.2$. Pressure coefficient & Bound Vorticity

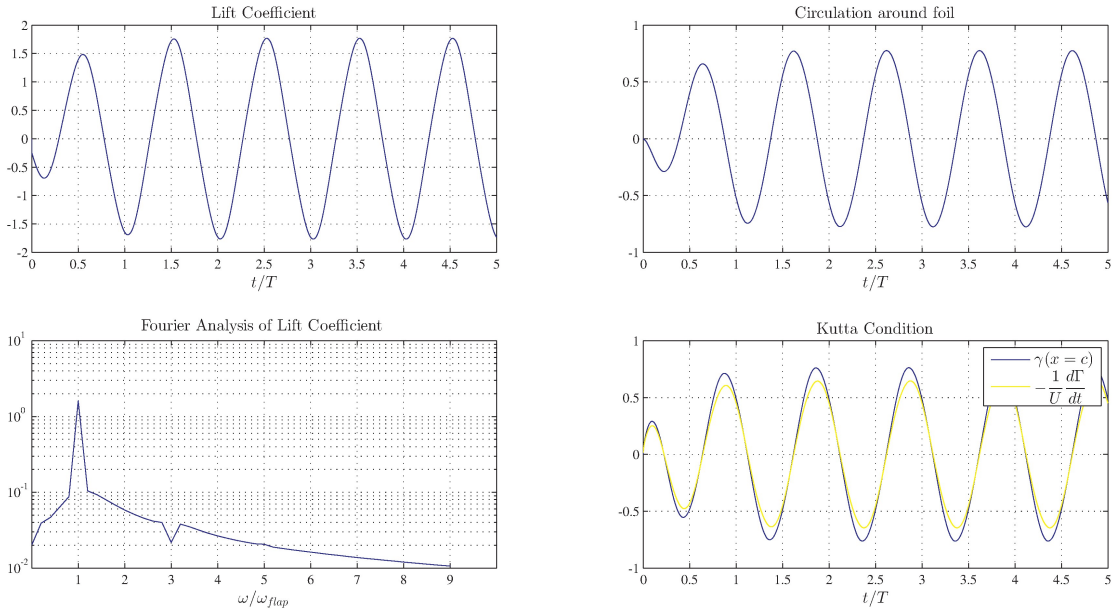

Figure 3.26: Case 2a; $h_0/c = 0.75$, $a_{max} = 30^o$, $St = 0.2$ Lift Coefficient, Circulation & Kutta condition

The vorticity in this region is negligible compared to the vorticity close to the leading edge, implying that the flow is weakly unsteady. In Figure 3.26 we observe that the higher – order peaks already reported are not reproduced in this case. This points to the fact that this parameter range corresponds to the linear response regime. Recall that for the same Strouhal number the previous case $\left(h_0/c = 0.25, a_{max} = 20^o\right)$ displayed higher unsteadiness.

The last case results, 2b, are presented in figures 3.27 – 3.28.

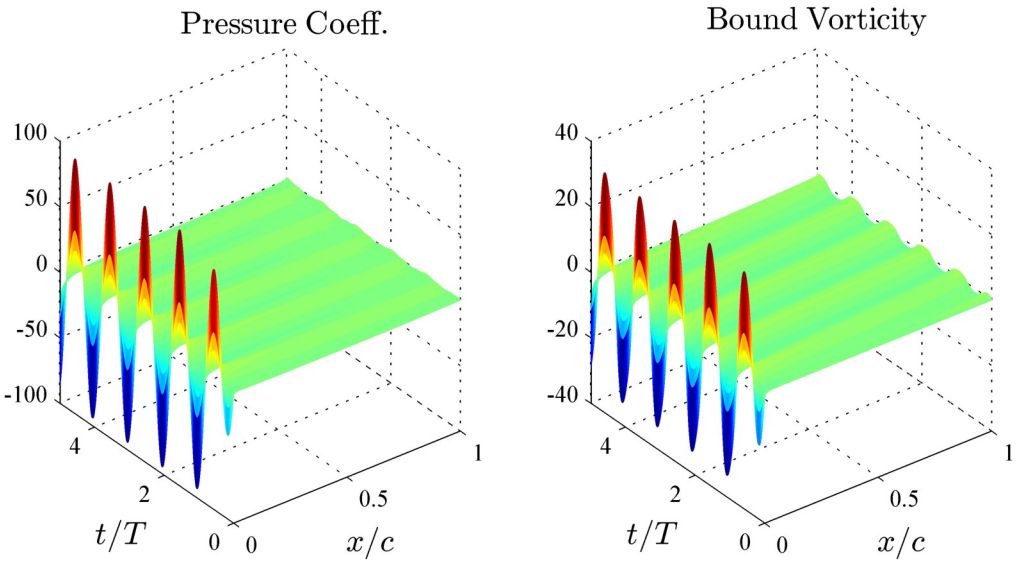

Figure 3.27: Case 2b; $h_0/c = 0.75$, $a_{max} = 30^o$, $St = 0.4$. Pressure coefficient & Bound Vorticity

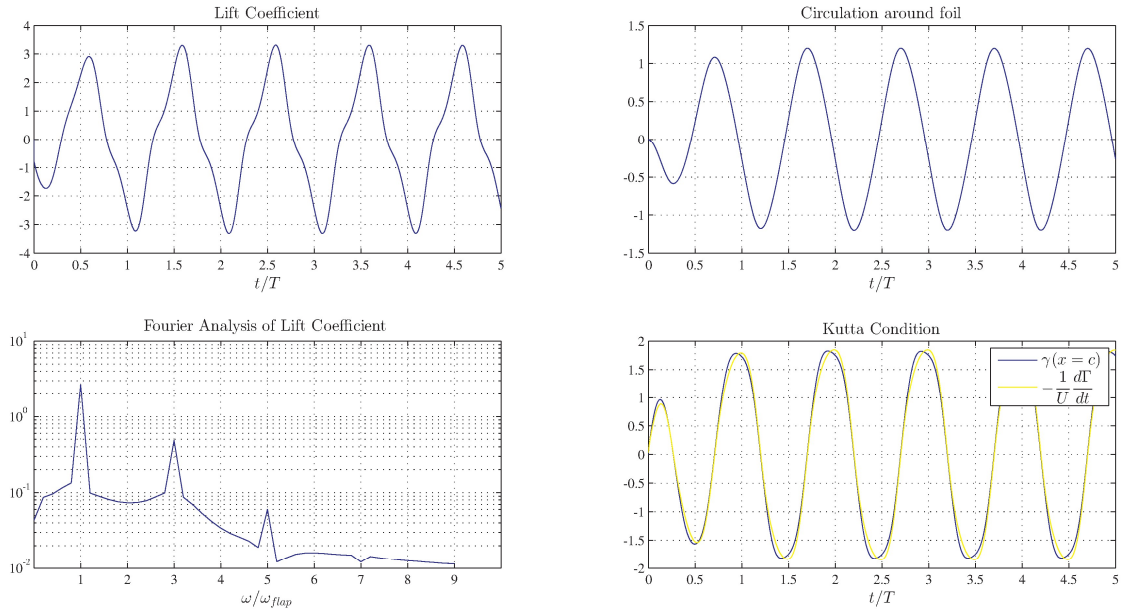

Figure 3.28: Case 2b; $h_0/c = 0.75$, $a_{max} = 30^o$, $St = 0.4$. Lift Coefficient, Circulation & Kutta condition

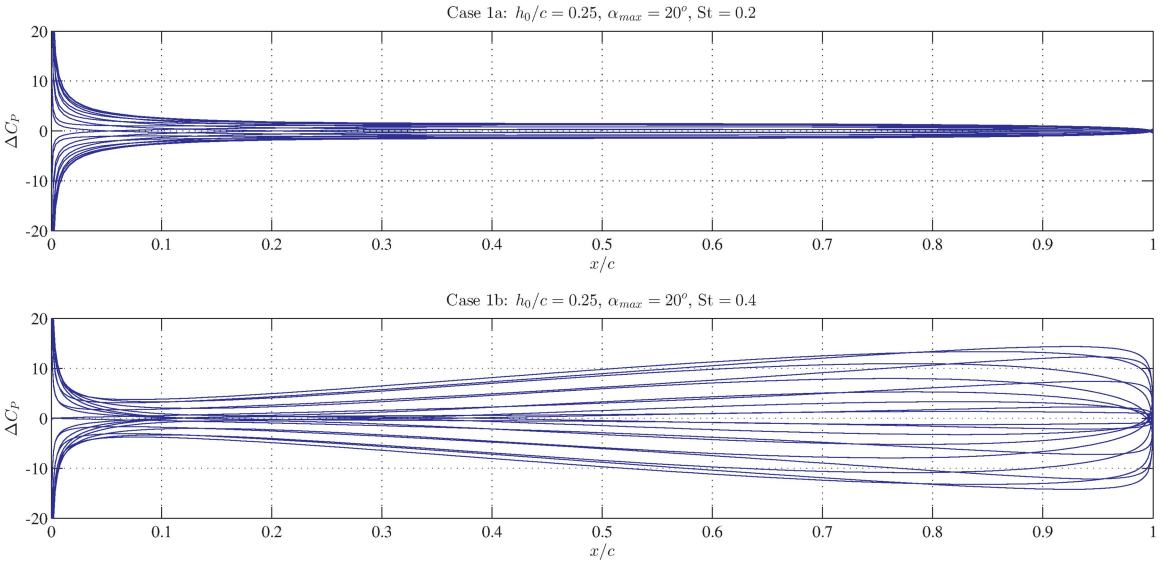

Figure 3.29: Comparison of the envelopes of the pressure difference coefficient ΔC_P for Cases 1a & 1b, during the last period of oscillation. In Case 1a (St = 0.2) ΔC_P smoothly tends to zero towards the leading edge, as is the case for steady flow. In Case 1b (St = 0.4) the flow is highly unsteady and ΔC_P attends high values in the trailing edge vicinity before abruptly diminishing to near zero values. This behaviour is also predicted by the analytical theory of Wu (1961) based on Prandtl's acceleration potential (1922).

3.8.4: Vorticity distribution: Bound & Free

In this section we present some results for the vorticity distribution in the whole domain boundary $\partial D = \partial D_B \cup \partial D_W$. The case study is a thin symmetric foil in flapping motion with kinematic parameters $h_0 / c = 0.8, St = 0.45, a_{max} = 20^o$ pitching around $1/3$ of its chord length with phase lag between heaving and pitching set to 90^o. The TSR has been set to 0.05, or 2000 time steps are used per motion period. The value of λ is set to 2.5, resulting in 59 chord elements iso – cosine spaced on the foil's camber line. The simulation duration is equal to 10 motion periods.

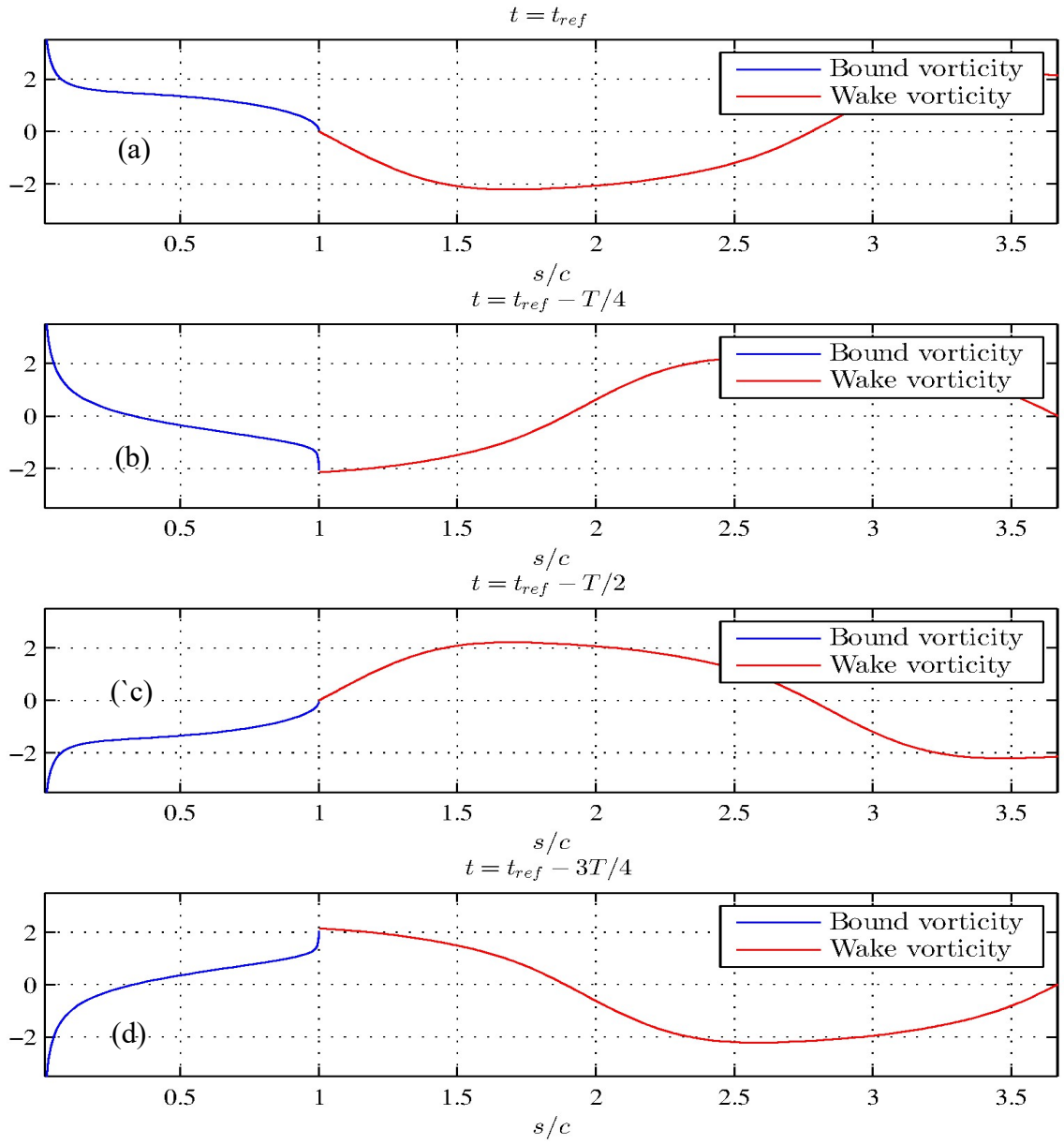

Figure 3.30: Vorticity distribution across foil and trailing wake.

Plots of the vorticity distribution across the foil and the adjacent trailing wake region are given in Figure 3.30 for four time instants in the last motion period, having as reference the instant where the circulation around the foil is maximized, t_{ref}.

In Figure 3.30 – a, the vorticity distribution is presented at the time instant when circulation around the foil is maximized. This means that $d\Gamma / dt = 0$, and hence by virtue of Eq.(2.2.4) the vorticity at the trailing edge is zero. The numerical results acquired by DVM satisfy this theoretical consideration. In Figure 3.30 – b the vorticity distribution is presented at a time instant *T*/4 before the circulation maximization. Keeping in mind that the circulation time signal is periodic with fundamental frequency equal to the flapping frequency and possible higher – orders harmonics being necessarily odd multiplies of the latter (as thoroughly explained in the previous section), this time instant corresponds to maximization of the circulation rate of change, $d\Gamma/dt$. By virtue of Eq.(2.2.4) again, the vorticity at the trailing edge is maximized. Note that in this case the vorticity at the trailing edge is negative, since the circulation around the foil is increased.

In Figure 3.30 – c the vorticity distribution is presented when the modulus of (negative) circulation is again maximized. As expected, the results are the same as in (a). Similarly, in Figure 3.30 – d the results are presented for three quarters of a period before the maximization of the circulation around the foil. The results are the same as in (b) with negative sign. This time instant is the same as $t_{ref} + T/4$ in the steady – state results. Finally, it is interesting to note that in all cases it holds

$$\lim_{\mathbf{r}(s;t)\to\mathbf{r}(s_{TE};t)^{+}}\left[\gamma\left(\mathbf{r}(s;t)\right)\right]=\lim_{\mathbf{r}(s;t)\to\mathbf{r}(s_{TE};t)^{-}}\left[\gamma\left(\mathbf{r}(s;t)\right)\right],$$

(3.8.4.1)

that is, continuation of the vorticity distribution is ensured at the trailing edge region.

3.9 Thrust and efficiency of flapping foil thruster

In this section we will study the thrust – producing capabilities of flapping foils. The results acquired through the DVM are compared with those from experiments and numerical simulations from the literature.

In Figure 3.31 the results of the present numerical method are compared against experimental results of Read et al (2003). The quantity tested is the thrust coefficient, as defined in Ch. 2, relations (2.3.19), (2.3.23). Systematic runs are performed for Strouhal numbers 0.20, 0.25, 0.30, 0.35, 0.40, 0.45 and pitch amplitudes ranging from 15° to 50°, resulting in effective angles of attack ranging from 5° to 35°, approximately.

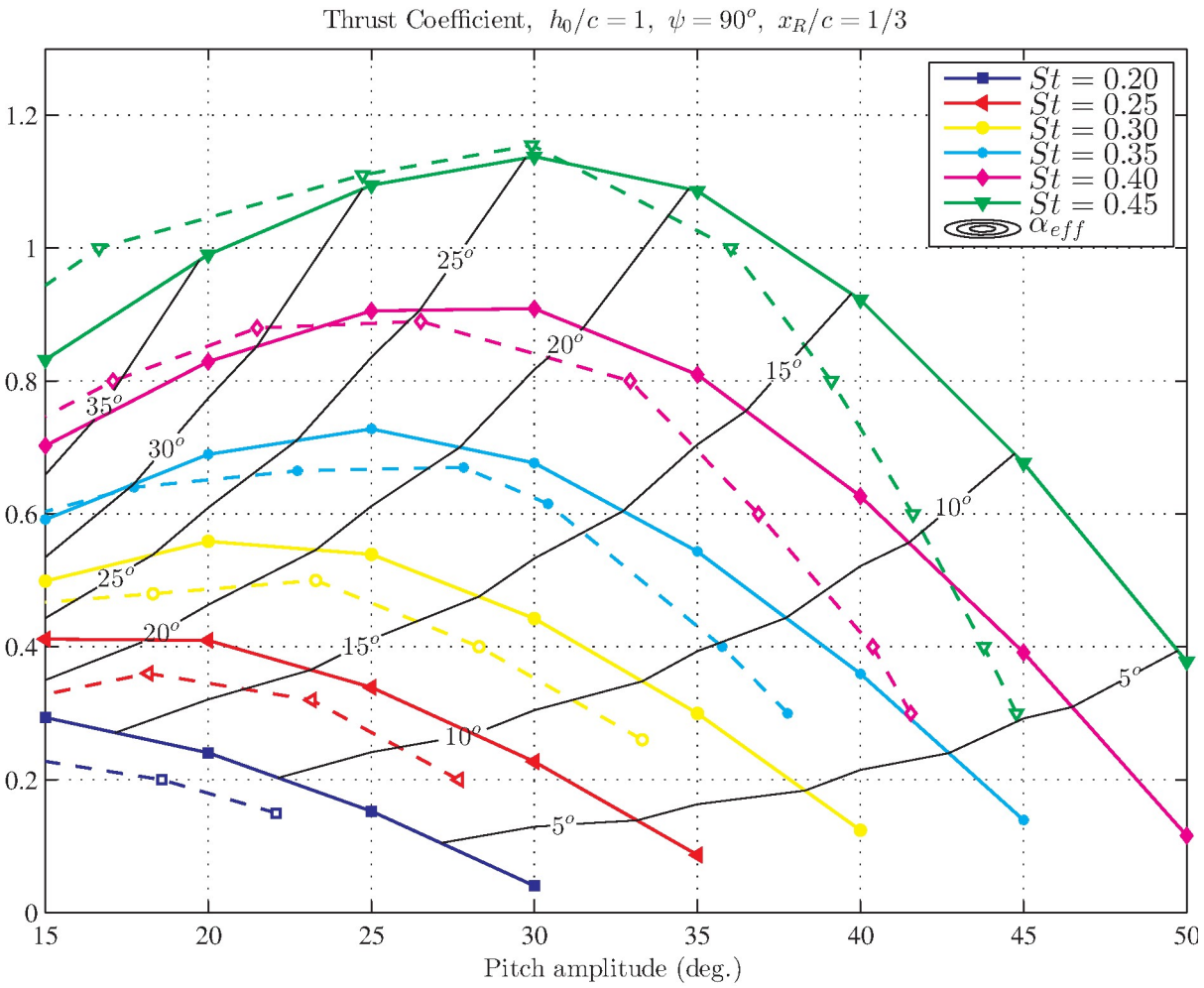

Figure 3.31: Comparison of C_T with experimental results for NACA 0012 foil from Read et al (2003). Solid lines correspond to the DVM results and dashed lines to the experimental results, respectively. Solid black lines visualize iso - a_{eff} lines, valid for numerical results only.

The agreement is good for moderate to large effective angles of attack up to about 25° and Strouhal numbers up to 0.40, approximately. For large values of a_{eff} (upper – left region of figure 3.31) the experimental values of C_T are larger than those of the DVM for St>0.3. This deviation is attributed to the fact that the NACA 0012 section that was used in the experiments, although symmetric it possesses different hydrodynamic attributes than the flat plate used in the present DVM. On the other hand, the performance of the NACA foil in the experiments is significantly worse for small values of a_{eff} as the Strouhal number increases (lower – right region of Figure 3.31). This is attributed to the degraded angle of attack time signal, possessing many peaks in a motion period, as has been stated by the authors in Read et al (2003). In Figure 3.31 three distinct cases of effective angle of attack profiles are presented.

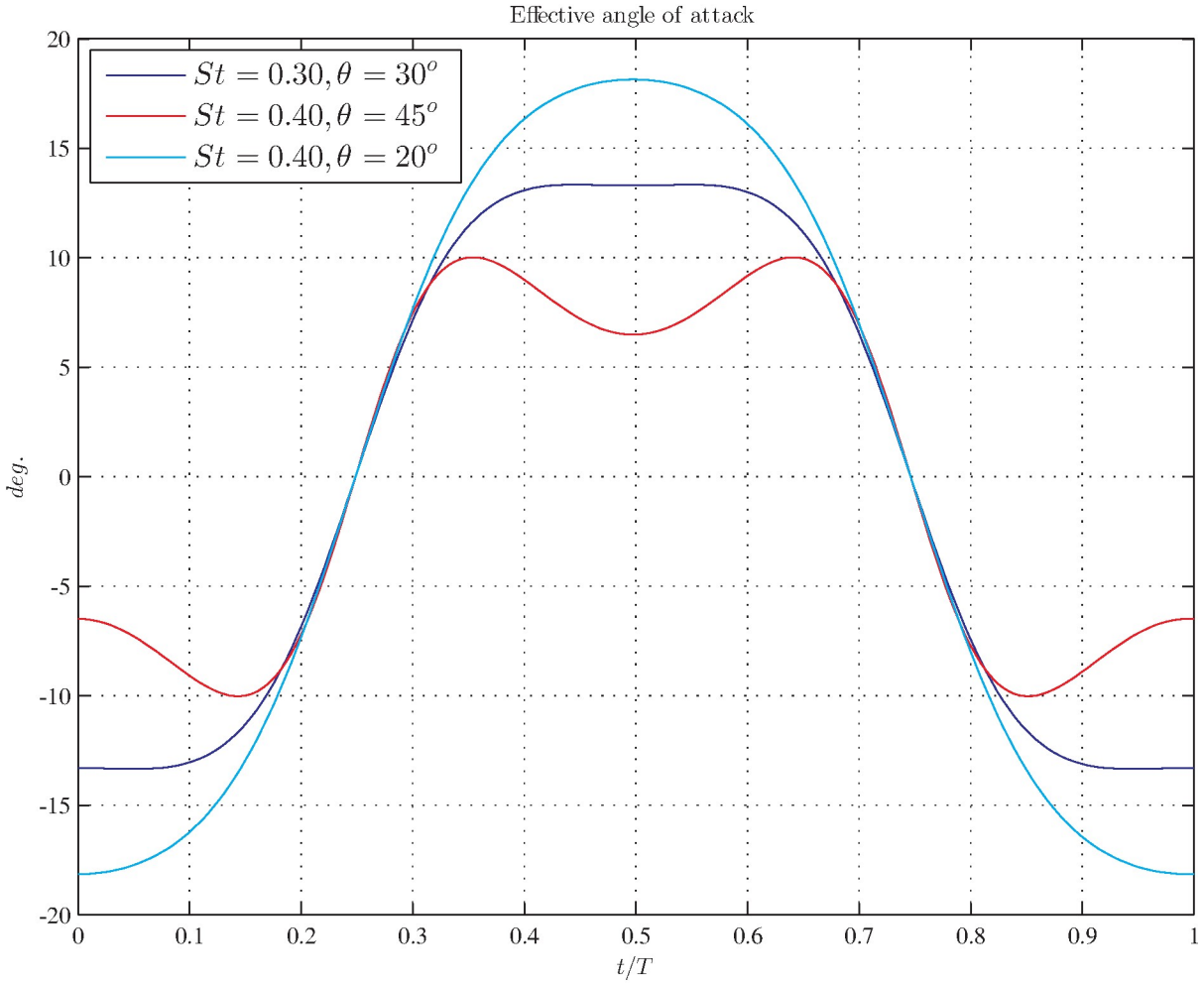

Figure 3.32: Angle of attack profiles for flapping motion in the parameter range experimentally tested by Read et al (2003)

In general, the rounded angle of attack profiles result in better efficiency, while sawtooth profiles (with two peaks per period) are associated with high thrust. High thrust and high efficiency are conflicting requirements; this is a known result from simple actuator disk theory in propellers. However, there are regions in the parameter range tested where high efficiency and sufficient thrust co – exist.

In Figure 3.33, the thrust curves acquired through the DVM for the parameter range tested by Read et al (2003) are presented along with iso – efficiency curves. This visualization is very useful for design purposes. It is obvious that there is a large region where moderate thrust coefficients and efficiencies can be achieved, which renders this parameter range interesting for propulsive purposes.

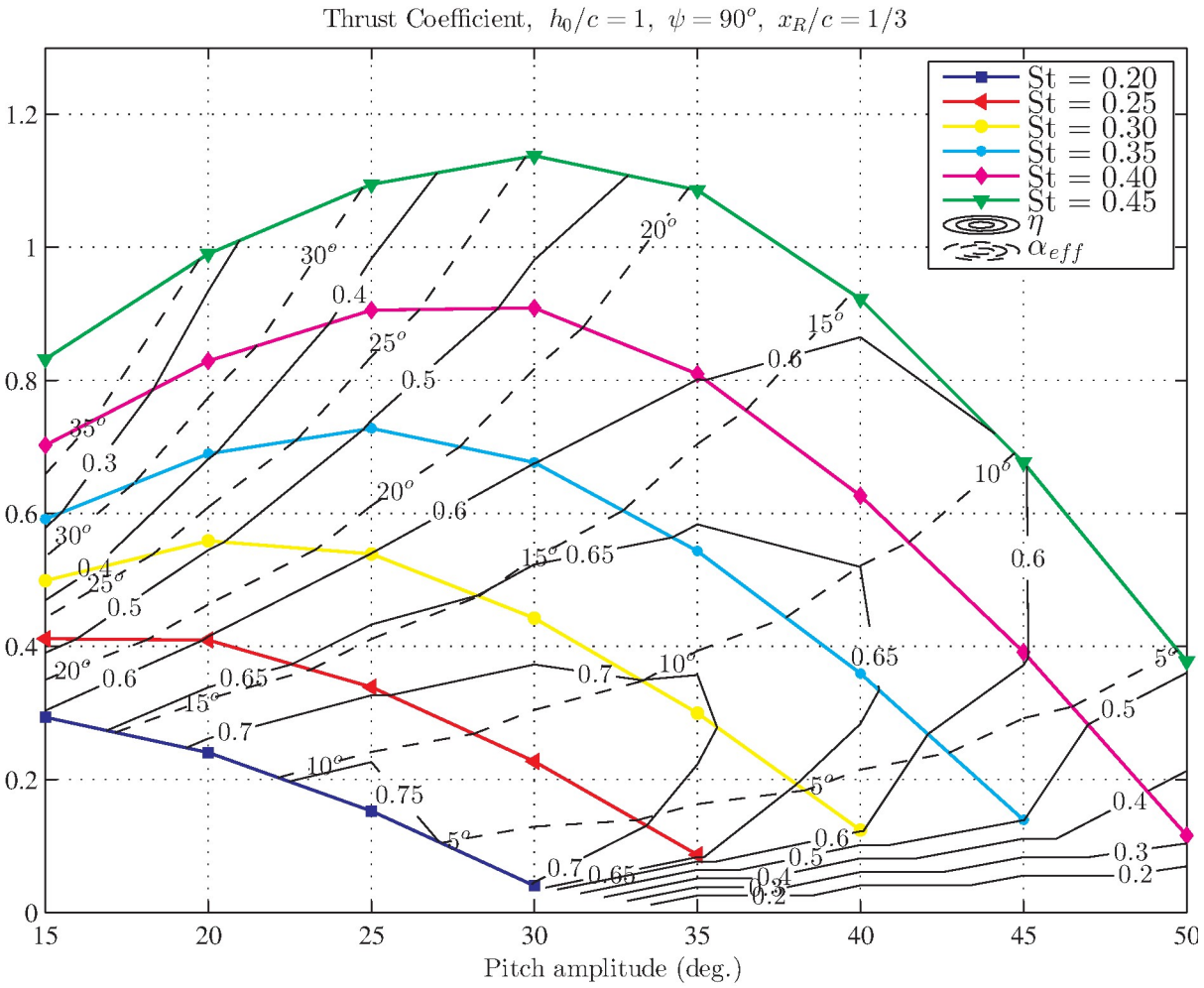

Figure 3.33: Thrust – efficiency curves for $h_0/c = 1, \psi = 90^o, x_R/c = 1/3$. Solid contour lines display iso – efficiency curves, while dashed contour lines display iso - a_{eff} curves.

Concluding the thrust and efficiency study of the DVM, we present time histories compared to the experimental results of Schouveiler et al (2005). The case in study is a flapping foil with $h_0/c = 0.75, a_{eff} = 20^o, St = 0.3, \psi = 90^o$. The authors provide the time histories of the thrust and lift force obtained. Their apparatus composed of a 18 meter – long water tank and a NACA 0012 section, with chord length equal to 0.1 m. and span 0.6 m. Thus an aspect ratio AR = 6 is achieved. Furthermore, they placed end – plates on the wing's tips to suppress 3 – D effects. Hence comparison between the experimental results and the present 2 – D method is possible. The curves are shown in figure 3.34.

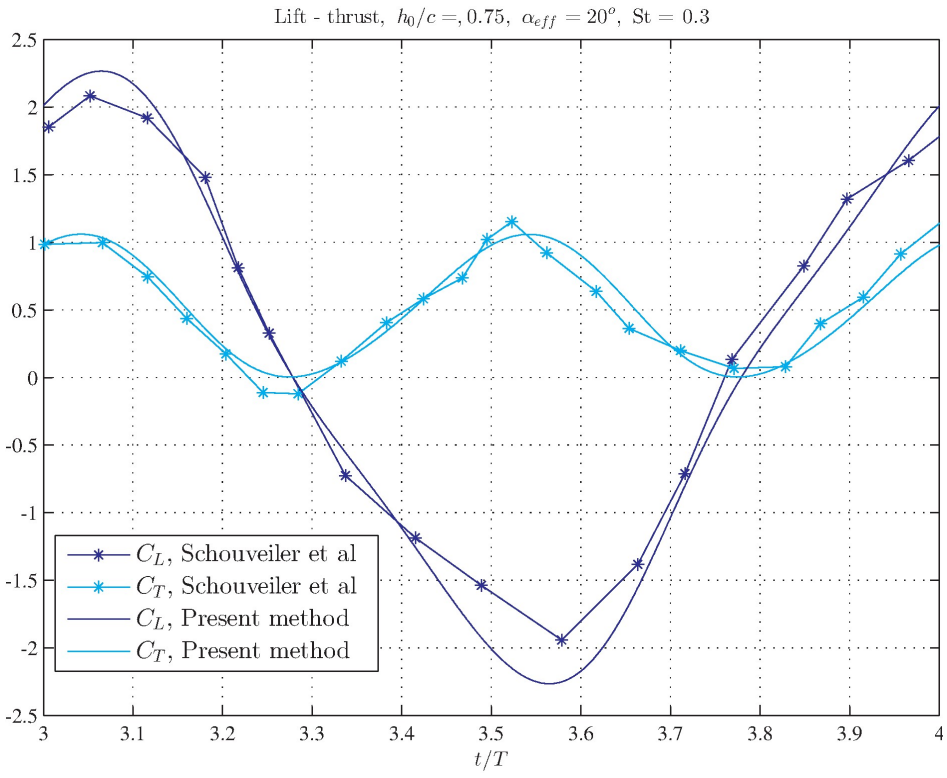

Figure 3.34: Comparison of time histories with experimental from Schouveiler et al (2005)

3.9.1 Leading Edge Suction Force

At this point where we have discussed the thrust capabilities of a flapping foil we deem necessary to consider the leading edge suction force. In order to acquire a physical interpretation of this quantity, consider a thin symmetric foil in parallel steady flow, having a

constant angle of attack. In Eq. (3.2.4) we gave the analytic result for the vorticity distribution in this case, which is repeated here for convenience

$$\gamma(x) = 2U\cos(a)\sqrt{\frac{c-x}{x}}\cdot\sin(a) \tag{3.9.1.1}$$

where α is the constant angle of attack and c is the chord length. In Eq. (3.9.1) we have taken into account that the parallel flow component on the foil's surface is $U\cos(\alpha)$ instead of U. The pressure difference coefficient is defined for this case by

$$\Delta C_P(x) = \frac{\rho U\gamma(x)}{\frac{1}{2}\rho U^2} = \frac{2}{U}\gamma(x). \tag{3.9.1.2}$$

Integrating ΔC_P we get the result

$$C_N = 2\pi\sin(a)\cos(a), \tag{3.9.1.3}$$

which is a normal to the foil's camber line force. Projecting it to directions parallel and normal to the incoming flow we have

$$C_L^* = 2\pi\sin(a)\cos^2(a) \tag{3.9.1.4}$$

and

$$C_X^* = 2\pi\sin^2(a)\cos(a) \tag{3.9.1.5}$$

The force parallel to the incoming flow in Eq. (3.9.1.5) is obviously a *drag* force. However, this cannot be the case in the scope of potential theory by virtue of the Kutta – Joukowski theorem. This indicates that there must be a force component, ignored by thus – far considerations. Moreover, the result for the lift force coefficient in (3.9.1.4) is not correct; we already know that it should be equal to $2\pi\sin(a)$. These curious results indicate that a force must exist to cancel out the obviously non – existent drag and adjust the lift force to meet the Kutta – Joukowski standard. This is the leading edge suction force, which is a result of an infinitely small pressure acting in an infinitely small area in the leading edge region, resulting in a finite result. We follow here the procedure by Kerwin (2001) and a more detailed proof

can be achieved through conformal mapping of a flat plate in a circle and forces calculation with the Blasius formula (Katz & Plotkin, 1991). One way to approach the problem in a simple manner is to calculate the leading – edge singularity. In the vicinity of the leading edge, the vorticity distribution is proportional to $\sqrt{c/x}$. We calculate the leading edge singularity strength as the bounded part of the vorticity distribution as

$$C = \lim_{x \to 0} \left[\gamma(x) \cdot \sqrt{x/c} \right]. \tag{3.9.1.6}$$

The leading edge suction parameter is defined as

$$C_S = \frac{\pi}{2} \left(\frac{C}{U} \right)^2 . \tag{3.9.1.7}$$

In the case of steady parallel flow at an angle of attack relative to the thin foil, it holds that $C_S = 2\pi \sin^2(a)$. If we now consider the force $F_{S0} = -\frac{1}{2}\rho U^2 c C_S = -\pi \rho U^2 c$ acting parallel to the foil and project it to axis normal and parallel to the incoming flow, we have

$$C_L = C_L^* - 2F_S / \rho U^2 c \left(-\sin(a) \right) = 2\pi \sin(a) \cos^2(a) + C_S \sin(a) = \\ = 2\pi \sin(a) \cos^2(a) + 2\pi \sin^3(a) = 2\pi \sin(a) \tag{3.9.1.8}$$

and

$$C_D = C_D^* - \cos(a) C_S = 2\pi \sin^2(a) \cos(a) - 2\pi \sin^2(a) \cos(a) = 0 \tag{3.9.1.9}$$

which are the expected results.

These results are valid for the steady case. However, for lack of a better method, we use Eq. (3.9.1.7) in a quasi – steady approximation in the case of unsteady motions, as well, where α is replaced by the instantaneous value of the effective angle of attack $\alpha_{eff}(t)$. However, in reality the leading edge suction cannot be achieved in its full strength. This is a result of flow separation which takes place at the leading edge region in large angles of attack or cavitation due to the vaporization of water, entering its wet region. This unattainability of the theoretical quasi – steady leading – edge suction is crudely incorporated in our numerical model. The idea belongs to Paraz et al (2016). The instantaneous value of the leading edge suction is modified as follows;

$$\mathbf{F}_S = F_{S0}\, f_{corr}(t)\left(\cos\theta(t), \sin\theta(t)\right) \tag{3.9.1.10}$$

where $F_{S0} = -\frac{\pi}{4}\rho U^2 c\left(\frac{C(t)}{U}\right)^2$ and $C(t)$ is calculated in the present DVM by means of Eq.(3.9.1.6) as follows

$$C(t) = \lim_{x\to 0}\left[\gamma(x,t)\sqrt{x/c}\right] \approx \frac{\Gamma_{B1}(t)}{\Delta x_1}\sqrt{\frac{xcp_1}{c}} \ . \tag{3.9.1.11}$$

Finally, the term $f_{corr}(t)$ is a correction term given by the expression

$$f_{corr}(t) = \left[1 - \tanh\left(8\left|a_{eff}(t)\right| - 3\right)\right]/2, \tag{3.9.1.11}$$

which attempts to account for flow separation at the leading edge. In their original work, Paraz et al (2015) used the expression $\tanh(15\alpha_{eff}(t) - 3)$, however, when we compared results with the experiments of Read et al (2003) the coefficient 7 gave better results. This can be explained by considering that Paraz et al (2015) used a flat plate as opposed to the NACA 0012 used by Read et al (2003). The empirical coefficient defined by Eq. (3.9.1.11) provides a leading-edge suction value that is 50% decreased for angle of attack around 20^o

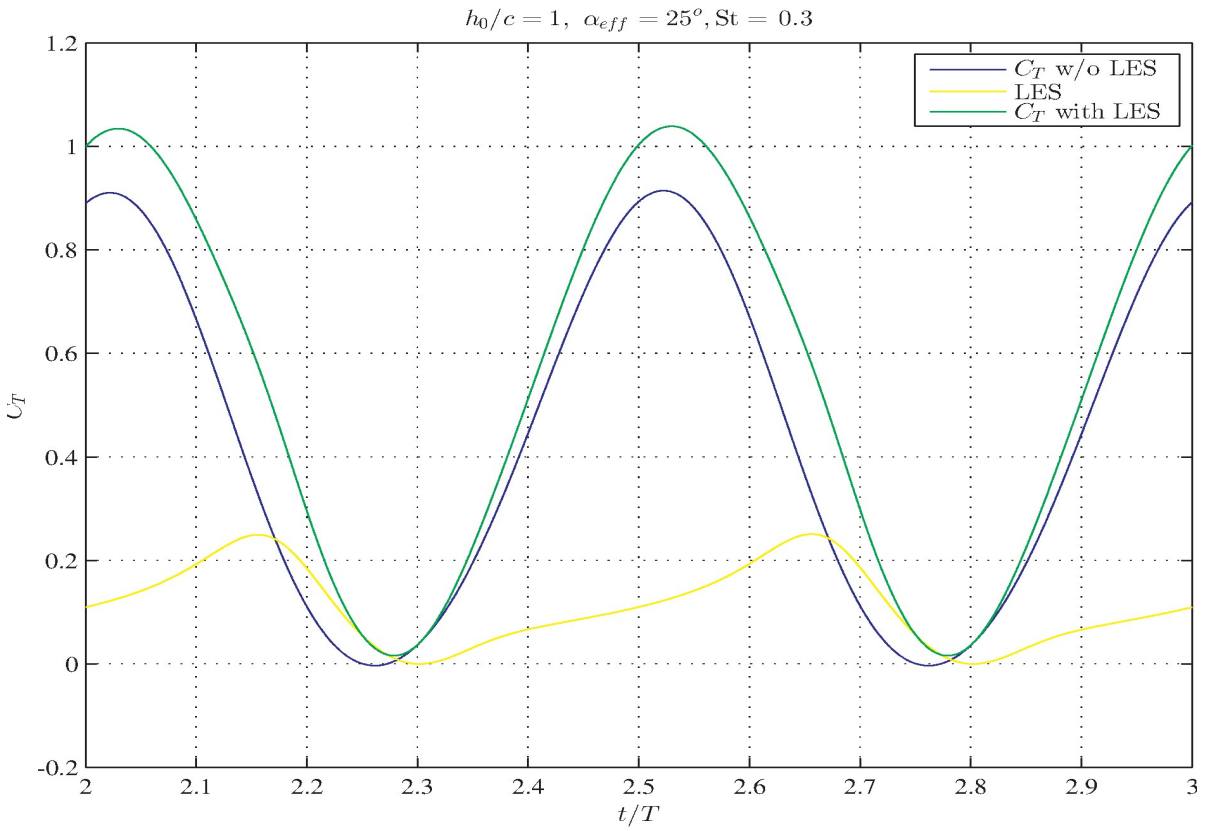

Figure 3.35: Leading Edge Suction

In Figure 3.35 the effect of the above Leading Edge Suction model to the total thrust coefficient is presented. It is obvious that the LES cannot be negative, a requirement that is satisfied by the present model. The modification of the suction force as a function of the instantaneous effective angle of attack causes the resulting thrust force to be somewhat biased.

Chapter 4: Flapping Foil with Chordwise Flexibility

In the final chapter of this work we will attempt to couple the hydrodynamics of the flapping foil which have been thoroughly presented in chapters 2 and 3 with chordwise flexibility added to it. The idea stems from observation of many aquatic as well as flying animals that seem to benefit from flexibility added to their tails or wings, adjusting their effective angle of attack relative to the flow in ways that preferable levels of thrust and efficiency are maintained.

The added chordwise flexibility renders the foil a thin elastic plate (without spanwise 3D effects) which is clamped at the pivot point and has free ends. In the present work the foil is considered clamped at the leading edge. The main reason is that experimental data that will be used for testing and validation of the present Elastic DVM are referred to such configurations (Fig.4.1). In addition, in the case of aquatic animal propulsion (e.g. thunniform swimming), the largest part of the body is considered rigid while the tail performs an oscillatory mode. The main characteristics of this setup are reproduces by a foil in heaving motion, pitching around its trailing edge.

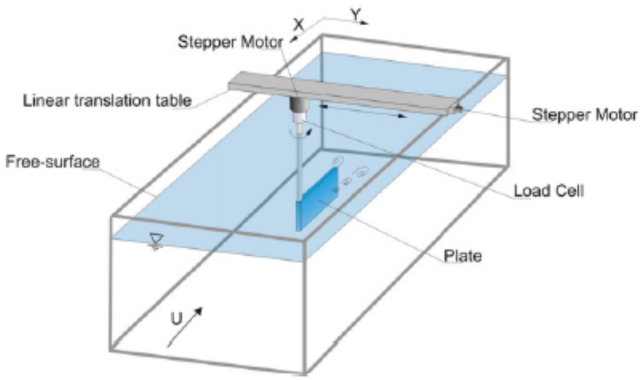

Fig.4.1 Schematic of the experimental system (Barranyk et al, 2012)

However, the present method is extendable to treat other configurations (e.g. clamped on any chordwise position)

4.1 Formulation of the foil as a thin flexible plate

We assume that the thin plate response is governed by the *Kirchhoff plate theory*.(Graff, 1975). Ignoring higher – order terms, rotary inertia, shear deformation and damping, the governing equation assumes the form

$$\nabla^2\left(D\nabla^2\eta\left(x,z;\mathrm{t}\right)\right)+\rho d\frac{\partial^2\eta\left(x,z;\mathrm{t}\right)}{\partial t^2}=p\left(x,z;t\right) \tag{4.1.1}$$

while the deflection occurs in the y – direction (normal to the plate mean surface). The first term in Eq.(4.1.1) is the inertia forces and the second term is the linear restoring force according to Hooke's law. The flexural rigidity D is given by

$$D\left(x\right)=\frac{Ed^3}{12\left(1-\nu^2\right)} \tag{4.1.2}$$

where E is the Young's modulus of the material and ν its Poisson ratio. The linear mass distribution of the plate is given by the relation

$$m\left(x\right)=\rho d\left(x\right) \tag{4.1.3}$$

where ρ is the material's density and d is the plate thickness.

Expanding the first term in the LHS of Eq. (4.1.1), we obtain $\nabla^2\left(D\nabla^2\eta\left(x,z;\mathrm{t}\right)\right)=\nabla^2D\cdot\nabla^2\eta\left(x,z;\mathrm{t}\right)+D\cdot\nabla^4\eta\left(x,z;\mathrm{t}\right)$. The biharmonic operator ∇^4, is defined as

$$\nabla^4\left(\cdot\right)=\frac{\partial^4\left(\cdot\right)}{\partial x^4}+\frac{\partial^4\left(\cdot\right)}{\partial z^4} \tag{4.1.4}$$

where z is the spanwise direction.

The term $\rho d\frac{\partial^2\eta\left(x,z;\mathrm{t}\right)}{\partial t^2}$ in the plate equation is associated with inertial effects. This expression would be correct and sufficient in the case when the analysis is carried out in an inertial coordinate system, as the one travelling with the hydrofoil at constant forward speed. In a subsequent section (Sec.4.5) the necessary modifications concerning the formulation in a non-inertial (accelerating) coordinate system (see Fig.4.1) as the body-fixed reference system

which is used in the case of a flapping hydrofoil (including the additional terms like centrifugal, Coriolis acceleration etc) are introduced and discussed.

The term in the RHS of Eq. (4.1.1) is the loading force per unit surface, having pressure units. In the present work spanwise deflections and hydrodynamic 3D phenomena are ignored, hence any z – dependence of the problem vanishes. Moreover, the model's assumptions under bending loading closely resemble those of the Euler – Bernoulli beam, in that plane sections remain plane and perpendicular to the middle plane, the deflection of which is the one actually described by Eq.(4.1.1). Applying all these assumptions and simplifications in Eq.(4.1.1), we finally obtain

$$\frac{\partial^2}{\partial x^2}\left(D(x)\frac{\partial^2 \eta(x;t)}{\partial x^2} \right) + m(x)\frac{\partial^2 \eta(x;t)}{\partial t^2} = p(x;t) \tag{4.1.5}$$

4.2 Coupling of Hydrodynamics with Elastic Response

In the case of a flapping foil, the transverse deflection is a result of the hydrodynamic pressure around it due to the incoming flow and its unsteady motion. This fact essentially states that the hydrodynamics and the response of the foil as a flexible thin plate are coupled through the pressure term of the RHS of Eq.(4.1.5). Thus the pressure term in Eq.(4.1.5) is8

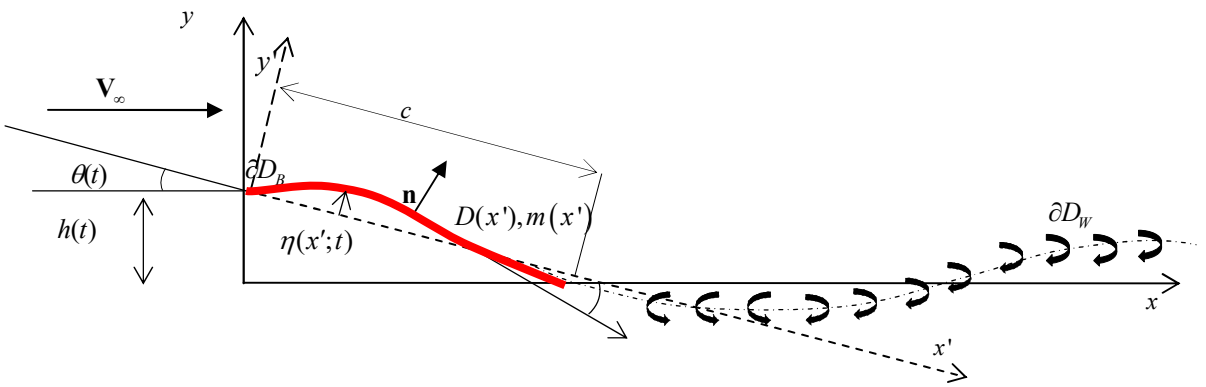

Figure 4.2: Foil (thick red line) and motion parameters sketch. The moving inertial and body fixed frames are denoted by x, y (solid lines) and x', y' (dashed lines), respectively. The trailing wake is drawn in dash – dot line and wake point vortices are denoted by curved arrows.

actually dependent on the elastic response $\eta(x;t)$ and should be formally written in the form $p(x,t;\eta)$.

The coupling of the potential flow problem and the elastic response is implicit in nature, meaning that the pressure term cannot be explicitly written in terms of the unknown function $\eta(x;t)$. The three main coupling mechanisms are;

- Adjustment of the no – entrance boundary condition to include the unit – normal to the foil vector modification due to elastic response – induced inclination. In the case where the foil is absolutely rigid, the unit – normal to the foil vector is given by (see figure 4.1)

  $$\mathbf{n}_{rig} = \left[-\sin\left(\theta(t)\right), \cos\left(\theta(t)\right)\right]^T \tag{4.2.1}$$

  Assume now that the foil is flexible, so a transverse deflection given by $\eta(x;t)$ results in an inclination distribution

  $$\theta_{el}(x;t) = \tan^{-1}\left(\frac{\partial \eta(x;t)}{\partial x}\right). \tag{4.2.2}$$

  This results in the following expression for the unit – normal vector;

  $$\mathbf{n}_{el} = \left[-\sin\left(\theta(t) + \theta_{el}(x;t)\right), \cos\left(\theta(t) + \theta_{el}(x;t)\right)\right]^T \tag{4.2.3}$$

- The no – entrance boundary condition must include the normal to the foil velocity due to its elastic response. This velocity is equal to $\frac{\partial \eta(x;t)}{\partial t}$. Projecting it to a direction normal to the foil's mean camber line, we obtain the term $\frac{\partial \eta(x;t)}{\partial t} \cdot \cos\left(\theta_{el}(x;t)\right)$ that is included in the RHS of the Neumann boundary condition.
- The geometry of the trailing wake is not a priori known, the case for a rigid flapping foil. Due to the unknown elastic response of the foil the position of the shed vortex at each time step is part of the solution. Formally, the position of the trailing edge in the rigid case is given by (see also Eqs. 2.2.10, 3.1.6, 3.1.7)

$$\mathbf{r}_{rig}(s_{TE};t) \triangleq \partial D_B \cap \partial D_W = \begin{bmatrix} c(1-x_R)\cos\left(\theta(t)\right) + x_R c \\ c(1-x_R)\sin\left(\theta(t)\right) + h(t) \end{bmatrix}, \tag{4.2.4}$$

which is only a function of the prescribed kinematics. In the case of a flexible flapping foil the position of the trailing edge is given by the relation

$$\mathbf{r}_{el}\left(s_{TE};t\right) \triangleq \partial D_B \cap \partial D_W = \begin{bmatrix} c\left(1-x_R\right)\cos\left(\theta\left(t\right)\right)+x_R c+\eta\left(c;t\right)\cdot\sin\left(\theta\left(t\right)\right) \\ c\left(1-x_R\right)\sin\left(\theta\left(t\right)\right)+h\left(t\right)+\eta\left(c;t\right)\cdot\cos\left(\theta\left(t\right)\right) \end{bmatrix}, \tag{4.2.5}$$

which is a function of the unknown trailing edge response $\eta\left(c;t\right)$. This implicit nonlinearity is treated by iterations are described in more detail in Sec. 4.7 below, where the extension of the present discrete model is presented.

4.3 Addition of Damping in Hydroelastic Coupling Model

It is a well – known fact that all realistic structures possess damping of some sort. In the case of a flapping foil, the damping is a result of internal damping due to the material, as well as external damping due to the surrounding fluid.

The viscoelasticity is an important aspect of the mechanical properties of polymers, the material that is used in many of the experimental apparatus to produce foils. It is defined as the property of the material which causes its strain to be time – dependent. It becomes more important as the temperature of the material rises and reaches the *glass transition temperature*, above which the material reacts in a manner between fluid – like and solid – like. The viscoelasticity is also evident in metals, although it is far less significant.

The viscous component of the stress in a viscoelastic material can be modelled as a dashpot. Assuming the Kelvin – Voigt model (Christensen, 1982) where the stress is given by a purely viscous damper and a purely elastic spring connected in parallel, the corresponding stress – strain relationship is

$$\sigma = E\varepsilon\left(t\right)+H\frac{d\varepsilon\left(t\right)}{dt}, \tag{4.3.1}$$

where $\varepsilon(t)$ is the strain and H is the viscoelasticity coefficient of the material. Its units are Ns/m^2. In Euler – Bernoulli beam theory, the strain is given by the transverse deflection as follows;

$$\varepsilon(x,y;t) = k(x;t)\,y = -y\frac{\partial^2\eta(x;t)}{\partial x^2}, \tag{4.3.2}$$

where $k(x;t)$ is the beam curvature, so that the viscous stress component is given by

$$\sigma(x,y;t) = -H\cdot y\frac{\partial^3\eta(x;t)}{\partial t\partial x^2}. \tag{4.3.3}$$

The bending moment due to viscoelastic forces at chordwise position x is given by

$$M(x;t) = -\int_{-d/2}^{d/2} y\sigma(x,y;t)\,dy = H\frac{\partial^3\eta(x;t)}{\partial t\partial x^2}\int_{-d/2}^{d/2} y^2 dy = H\frac{d^3}{12}\frac{\partial^3\eta(x;t)}{\partial t\partial x^2}, \tag{4.3.4}$$

Differentiating twice with respect to x, we acquire the viscoelastic loading contribution

$$q_{visco}(x;t) = \frac{\partial^3}{\partial t\partial x^2}\left(\mu\frac{\partial^2\eta(x;t)}{\partial^2 x}\right) \tag{4.3.5}$$

where $\mu = Hd^3/12$ is the viscoelastic coefficient (with units $Nms = kgm^2/s$).

The viscoelastic contribution to the bending of the plate is linear with respect to the unknown transverse deflection η, thus it can easily be treated in the frame of the present finite difference scheme (discussed in Ch. 4).

Proceeding to the external damping, we first consider the linear version. It is historically the first damping mechanism considered owing to its simplicity and straightforward implementation in a system of dynamical equations. Its main drawbacks are that it does not model many realistic situations and the fact that its estimation is not possible in any physical basis, thus empirical estimates are needed. In the case of systems with many DOFs the simplest way to construct a damping matrix is with the Rayleigh's method, which we present in the Appendix. The loading contribution of the linear external damping in given by

$$q_{L-damp-ext}\left(x;t\right)=C\cdot\frac{\partial\eta\left(x;t\right)}{\partial t}. \tag{4.3.6}$$

Apart from the linear external damping, we include in our model a quadratic damping term. It is implemented by adding the term

$$q_{Q-damp-ext}\left(x;t\right)=C_D\left|\frac{\partial\eta\left(x;t\right)}{\partial t}\right|\frac{\partial\eta\left(x;t\right)}{\partial t}. \tag{4.3.7}$$

According to this definition, the quadratic drag coefficient C_D has units $Ns^2/m^4=kg/m^3$. The term $\left|\frac{\partial\eta\left(x;t\right)}{\partial t}\right|$ ensures that this force is always a drag force. This non – linear damping term was added to the analytical model developed by Paraz et al (2016) to capture the effects of the transverse drag force induced by the fluid on a flexible heaving foil. In the latter work a suitable value reported in order for the model to fit well with experiments is $C_D=24m/c$, where *m* is the surface mass density and *c* is the chord length.

Incorporating the damping terms in our model for the hydroelastic coupling, we have

$$m\frac{\partial^2\eta\left(x;t\right)}{\partial t^2}+\frac{\partial^2}{\partial x^2}\left(D\frac{\partial^2\eta\left(x;t\right)}{\partial x^2}\right)+C\frac{\partial\eta\left(x;t\right)}{\partial t}+\frac{\partial^3}{\partial t\partial x^2}\left(\mu\frac{\partial^2\eta\left(x;t\right)}{\partial^2 x}\right)+C_D\left|\frac{\partial\eta\left(x;t\right)}{\partial t}\right|\frac{\partial\eta\left(x;t\right)}{\partial t}=$$
$$=\Delta p\left(x,\eta;t\right) \tag{4.3.8}$$

The above hydroelastic model and its coupling with hydrodynamic equations presented in the sequel is appropriate for relatively small deflections. In the case of large deflections an extended model would be based on curvilinear or discrete beam models.

4.4 System of Equations for the Hydrodynamic Coupling Problem

Having established the model for the flexible foil response under hydrodynamic loading we proceed to present the full system of equations used to study the effect of chordwise flexibility in the flapping – foil thrusters.

The no- entrance boundary condition is described by the following integral equation (2.2.11) discussed in Ch.2

$$\begin{aligned}\left(\mathbf{V}_{\mathbf{A}}-\mathbf{V}_{\infty}-\mathbf{V}_{\mathbf{G}}\right)\cdot\mathbf{n}=&-\frac{1}{2\pi}\int\limits_{\partial D_B}\frac{\gamma_B(\xi;t)}{\left|\mathbf{r}\left(\xi\,|\,\mathrm{s};\mathrm{t}\right)\right|^2}\left\{\mathbf{k}\times\mathbf{r}\left(\xi\,|\,s;t\right)\right\}\cdot\mathbf{n}d\xi+\\&-\frac{1}{2\pi}\int\limits_{\partial D_W}\frac{\gamma_W(\xi\,|\,\xi_{TE};t-t_{TE})}{\left|\mathbf{r}\left(\xi\,|\,\mathrm{s};\mathrm{t}\right)\right|^2}\left\{\mathbf{k}\times\mathbf{r}\left(\xi\,|\,s;t\right)\right\}\cdot\mathbf{n}d\xi.\end{aligned}\tag{4.4.1}$$

where $\gamma_B\left(s;t\right),\mathbf{r}\left(s;t\right)$ is the bound to the foil's mean surface (or mean camber line) vorticity, and serves as the unknown function. The LHS of Eq.(4.4.1) is the projection of the relative to the foil velocity, composed of the free stream flow $\mathbf{V}_{\infty}$, a background unsteady velocity field (gust) $\mathbf{V}_G$ and the foil's motion $\mathbf{V}_{\mathbf{A}}=\mathbf{V}_{flap}+\mathbf{V}_{res}$, where the first term is due to the rigid body motion and the second due to elastic response. The normal unit vector $\mathbf{n}$ has been defined in relation (4.2.3), including the elasticity effects.

The pressure is given by relation

$$\begin{aligned}\Delta p\left(x;t\right)=&\rho\left[\frac{d[\![\phi]\!]}{dt}+\nabla[\![\phi]\!]\cdot\left(\mathbf{V}_{\infty}+\mathbf{V}_{\mathbf{G}}-\mathbf{V}_{\mathbf{A}}\right)\right]=\\&\rho\left[\frac{d}{dt}\int_0^x\gamma_B\left(x;t\right)ds\left(x\right)+\gamma_B\left(x;t\right)\cdot\left(\mathbf{V}_{\infty}+\mathbf{V}_{\mathbf{G}}-\mathbf{V}_{\mathbf{A}}\right)\cdot\boldsymbol{\tau}\left(x;t\right)\right],\end{aligned}\tag{4.4.2}$$

where $\boldsymbol{\tau}\left(x;t\right)$ is the tangent to the foil unit vector. However, the integral $[\![\phi\left(x;t\right)]\!]=\int_0^x\gamma_B\left(x;t\right)ds\left(x\right)$ takes into account that the integration domain is not a straight line

indirectly via the $ds(x)$ differential which can be interpreted as the local infinitesimal length of the mean camber line.

Combining equations (4.4.2) and (4.3.8) we obtain

$$m\frac{\partial^2\eta(x;t)}{\partial t^2}+\frac{\partial^2}{\partial x^2}\left(D\frac{\partial^2\eta(x;t)}{\partial x^2}\right)+C\frac{\partial\eta(x;t)}{\partial t}+\frac{\partial^3}{\partial t\partial x^2}\left(\mu\frac{\partial^2\eta(x;t)}{\partial^2 x}\right)+C_D\left|\frac{\partial\eta(x;t)}{\partial t}\right|\frac{\partial\eta(x;t)}{\partial t}=$$
$$=\rho\left[\frac{d}{dt}\int_0^x\gamma_B(x;t)ds(x)+\gamma_B(x;t)\cdot(\mathbf{V}_\infty+\mathbf{V_G}-\mathbf{V_A})\cdot\boldsymbol{\tau}(x;t)\right] \tag{4.4.3}$$

The solution of the present hydroelastic coupling problem consists of the simultaneous solution of the above equation in conjunction with the no-entrance boundary condition expressed by Eq. (4.4.1).

4.5 Equations in the body-fixed frame of reference

We recall the expression for the acceleration of points in the foil's body in the inertial reference frame with respect to their coordinates on the body – fixed reference frame. We note that the body – fixed reference frame is a rotating frame, performing a vertical oscillatory motion due to the heaving as well. Considering only the rotational pitching motion, the acceleration of a point on the foil is given by (Landau & Lifschitz, 1976)

$$\mathbf{a}=\mathbf{a}_R+2\boldsymbol{\Omega}\times\mathbf{v}_R+\boldsymbol{\Omega}\times(\boldsymbol{\Omega}\times\mathbf{r})+\frac{d\boldsymbol{\Omega}}{dt}\times\mathbf{r}\,, \tag{4.4.3}$$

where

- $\mathbf{a}_R$ is the acceleration of the points in the rotating reference frame (due to only the elastic deformation of the foil)
- $-2\boldsymbol{\Omega}\times\mathbf{v}_R$ is the Coriolis acceleration
- $-\boldsymbol{\Omega}\times(\boldsymbol{\Omega}\times\mathbf{r})$ is the centrifugal acceleration

- $-\frac{d\boldsymbol{\Omega}}{dt}\times\mathbf{r}$ is the Euler force
- $\mathbf{r}$ is the position vector in the rotating reference frame
- $\boldsymbol{\Omega}$ is the angular velocity of the rotational reference frame

In the case of a foil performing pitching motion around its leading edge where $x'=0$, the position vector of points on its surface subject to elastic deformation transverse to the mean camber line in the rotating frame is defined as

$$\mathbf{r}\left(x';t\right)=\left[x',\eta'\left(x';t\right),0\right]^{T}=x'\cdot\hat{\mathbf{i}}+\eta'\left(x';t\right)\cdot\hat{\mathbf{j}}+0\cdot\hat{\mathbf{k}}, \tag{4.4.4}$$

where $\hat{\mathbf{i}},\hat{\mathbf{j}},\hat{\mathbf{k}}$ are the unit vectors in the rotational frame according to the right – hand rule, therefore $\hat{\mathbf{k}}=\hat{\mathbf{i}}\times\hat{\mathbf{j}}$. We note that in our case $\eta'\left(x';t\right)$ is due to elastic deformation only.

The angular velocity is defined as

$$\boldsymbol{\Omega}=0\cdot\hat{\mathbf{i}}+0\cdot\hat{\mathbf{j}}+\dot{\theta}\left(t\right)\cdot\hat{\mathbf{k}}. \tag{4.4.5}$$

The velocity of the points on the foil's surface in the rotational frame is

$$\mathbf{v}_{R}\left(x';t\right)=0\cdot\hat{\mathbf{i}}+\dot{\eta}'\left(x';t\right)\cdot\hat{\mathbf{j}}+0\cdot\hat{\mathbf{k}}, \tag{4.4.6}$$

due to the foil's deformation as a thin plate only. Performing the vector algebra, the accelerations defined are;

$$\mathbf{a}_{R}=0\cdot\hat{\mathbf{i}}+\ddot{\eta}'\left(x';t\right)\cdot\hat{\mathbf{j}}+0\cdot\hat{\mathbf{k}}, \tag{4.4.7}$$

$$-\boldsymbol{\Omega}\times\left(\boldsymbol{\Omega}\times\mathbf{r}\right)=x'\cdot\dot{\theta}^{2}\left(t\right)\hat{\mathbf{i}}-\eta'\left(x';t\right)\dot{\theta}^{2}\left(t\right)\hat{\mathbf{j}}, \tag{4.4.8}$$

$$-2\boldsymbol{\Omega}\times\mathbf{v}_{R}=2\dot{\eta}'\left(x';t\right)\dot{\theta}\left(t\right)\hat{\mathbf{i}}, \tag{4.4.9}$$

$$-\frac{d\boldsymbol{\Omega}}{dt}\times\mathbf{r}=\dot{\eta}'\left(x';t\right)\cdot\ddot{\theta}\left(t\right)\cdot\hat{\mathbf{i}}-x'\ddot{\theta}\left(t\right)\cdot\hat{\mathbf{j}}. \tag{4.4.10}$$

Substituting to Eq.(4.4.3), we have

$$\mathbf{a}(x';t)=\left[-2\eta'(x';t)\cdot\dot{\theta}(t)-x'\dot{\theta}^2(t)-\eta'(x';t)\ddot{\theta}(t)\right]\cdot\hat{\mathbf{i}}+ \\ +\left[\ddot{\eta}'(x';t)+\eta'(x';t)\cdot\dot{\theta}^2(t)+x'\cdot\ddot{\theta}\right]\cdot\hat{\mathbf{j}} \tag{4.4.11}$$

The acceleration of the point on the foil due to its heaving motion is

$$\mathbf{a}_h(t)=0\cdot\mathbf{i}_{IN}+\ddot{h}(t)\cdot\mathbf{j}_{IN}, \tag{4.4.12}$$

where $\mathbf{i}_{IN}, \mathbf{j}_{IN}$ are the unit basis vectors of the inertial reference frame. They are immediately associated with the unit basis vectors of the rotating reference frame $\hat{\mathbf{i}}, \hat{\mathbf{j}}$ by the relation

$$\begin{bmatrix}\mathbf{i}_{IN}\\ \mathbf{j}_{IN}\end{bmatrix}=\begin{bmatrix}\cos\theta(t) & -\sin\theta(t)\\ \sin\theta(t) & \cos\theta(t)\end{bmatrix}\begin{bmatrix}\hat{\mathbf{i}}\\ \hat{\mathbf{j}}\end{bmatrix}, \tag{4.4.13}$$

which has only formal meaning; to interpret it, one has to treat the unit basis vectors involved as scalars. Substituting (4.4.13) to (4.4.12) and adding to (4.4.11), we get the expression for the inertial acceleration of the points on the flexible foil

$$\mathbf{a}(x';t)=\left[-2\eta'(x';t)\cdot\dot{\theta}(t)-x'\dot{\theta}^2(t)-\eta'(x';t)\ddot{\theta}(t)+\ddot{h}(t)\sin\theta(t)\right]\cdot\hat{\mathbf{i}}+ \\ +\left[\ddot{\eta}'(x';t)+\eta'(x';t)\cdot\dot{\theta}^2(t)+x'\cdot\ddot{\theta}+\ddot{h}(t)\cos\theta(t)\right]\cdot\hat{\mathbf{j}} \tag{4.4.14}$$

Substituting the inertial acceleration transverse to the foil's mean camber line from Eq. (4.4.14) to the PDE (4.1.5) we have.

$$\frac{\partial^2}{\partial x'^2}\left(D\frac{\partial^2\eta'(x';t)}{\partial x'^2}\right)=p(x';t)-m(\mathbf{a}+\mathbf{a}_h)\hat{\mathbf{j}}$$

which finally reduces to

$$m\frac{\partial^2\eta'(x';t)}{\partial t^2}+\frac{\partial^2}{\partial x'^2}\left(D\frac{\partial^2\eta'(x';t)}{\partial x'^2}\right)=p(x';t)-m\left(\eta'(x';t)\cdot\dot{\theta}^2(t)+x'\cdot\ddot{\theta}(t)+\ddot{h}(t)\cos\theta(t)\right) \tag{4.4.15}$$

This above model is enhanced by the incorporation of the damping terms (as in Eq.4.4.3), and after dropping the $(\cdot)'$ notation we finally have

$$m\frac{\partial^2\eta(x;t)}{\partial t^2}+\frac{\partial^2}{\partial x^2}\left(D\frac{\partial^2\eta(x;t)}{\partial x^2}\right)+C\frac{\partial\eta(x;t)}{\partial t}+\frac{\partial^3}{\partial t\partial x^2}\left(\mu\frac{\partial^2\eta(x;t)}{\partial^2 x}\right)+C_D\left|\frac{\partial\eta(x;t)}{\partial t}\right|\frac{\partial\eta(x;t)}{\partial t}=$$

$$=\rho\left[\frac{d}{dt}\int_0^x\gamma_B(x;t)\,ds(x)+\gamma_B(x;t)\cdot\left(\mathbf{V}_\infty+\mathbf{V}_\mathbf{G}-\mathbf{V}_\mathbf{A}\right)\cdot\boldsymbol{\tau}(x;t)\right]+$$

$$-m\left(\eta'(x';t)\cdot\dot{\theta}^2(t)+x'\cdot\ddot{\theta}(t)+\ddot{h}(t)\cos\theta(t)\right), \qquad (4.4.16)$$

which is the PDE to be solved, in conjunction with Eq. (4.4.1) in the present coupled hydrodynamic model.

4.6 Boundary Conditions for Flexible Foil

The foil is clamped on one end and free on the other. Usually, the clamped end coincides with the leading edge. For a fourth order PDE four boundary conditions are needed to fully define its solution. In the inertia reference frame the boundary conditions at the clamped end are those of prescribed position and inclination through the heaving and the pitching instantaneous values, respectively (see Figure 4.1). This translates to the following conditions in the inertial (steadily translating) system

$$\eta(0;t)=h(t), \qquad \frac{\partial\eta(0;t)}{\partial x}=\theta(t) \qquad (4.6.1)$$

which is equivalent to

$$\eta(0;t)=0, \qquad \frac{\partial\eta(0;t)}{\partial x}=0 \qquad (4.6.2)$$

in the body-fixed frame.

At the free trailing edge conditions of zero shear force and bending moment hold. They are associated with the deflection $\eta(x;t)$ by the relations

$$\frac{\partial}{\partial x}\left(D\frac{\partial^2\eta(x;t)}{\partial x^2}\right)\Bigg|_{x=c} + \frac{\partial^2}{\partial t\partial x}\left(\mu\frac{\partial^3\eta(x;t)}{\partial x^3}\right)\Bigg|_{x=c} = 0, \tag{4.6.3}$$

$$D\frac{\partial^2\eta(x;t)}{\partial x^2}\Bigg|_{x=c} + \mu\frac{\partial}{\partial t}\left(\frac{\partial^2\eta(x;t)}{\partial x^2}\right)\Bigg|_{x=c} = 0, \tag{4.6.4}$$

respectively.

4.7 Development of the discrete scheme

The solution of the PDE Eq. (4.4.16) is achieved by applying a finite difference scheme. First the solution domain is discretized in exactly the same way as in the hydrodynamic problem of a rigid flapping foil. Therefore we try to calculate the deflection at the collocation points of the hydrodynamic problem, described by $xcp_i, i = 1,...,N_B$ as defined in Eq. (2.4.2.2). Thus the problem of the elastic thin plate response is reduced to a multiple DOF problem. Restricting ourselves to homogenous flapping foils, the following equation holds for the corresponding deflection η_i at each collocation point:

$$m_i\ddot{\eta}_i + \left(D\cdot\eta_i^{iv}\right) + \left(C\cdot\dot{\eta}_i\right) + \mu\left(\dot{\eta^{iv}}\right) + C_D\left|\dot{\eta}_i\right|\dot{\eta}_i = \frac{1}{2}\rho U^2\Delta C_{pi} - m_i\alpha_i, \tag{4.7.1}$$

where η_i^{iv} is the corresponding value of the fourth spatial derivative and $\dot{\eta}$ is the response velocity. The term α_i is the corresponding value of the acceleration terms that manifest due to the non – inertial reference frame that the PDE is defined in.

We want to obtain the solution of the PDE (4.4.16) in the vector form $\boldsymbol{\eta} = \left[\eta_1, \eta_2, ..., \eta_{N_B}\right]^T$. To this end, we define the response velocity vector $\mathbf{u} = \left[u_1, u_2, ..., u_{N_B}\right]^T$. The spatial derivatives in (4.7.1) are approximated using the finite differences scheme explained in detail in Ch. 4.

We recast relation (4.7.1) in the following form:

$$m_i\dot{u}_i + \left(D\cdot\eta_i^{iv}\right) + \left(C\cdot u_i\right) + \mu u_i^{iv} + C_D\left|u_i\right|u_i = \frac{1}{2}\rho U^2\Delta C_{pi} - m_i\alpha_i \tag{4.7.2a}$$

$$u_i - \dot{\eta}_i = 0 \tag{4.7.2b}$$

The vectors $\boldsymbol{\eta}^{iv} = \left[\eta_1^{iv}, \eta_2^{iv}, ..., \eta_{N_B}^{iv} \right]$, $\mathbf{u}^{iv} = \left[u_1^{iv}, u_2^{iv}, ..., u_{N_B}^{iv} \right]$ are given by the expressions

$$\boldsymbol{\eta}^{iv} = \mathbf{FD}_4 \cdot \boldsymbol{\eta}, \qquad \mathbf{u}^{iv} = \mathbf{FD}_4 \cdot \mathbf{u}\,, \tag{4.7.3}$$

where $\mathbf{FD}_4$ is a matrix containing the fourth – derivative stencil in the collocation points grid. Thus we have achieved to express the derivatives involved in the discretized form of the elastic response PDE in linear terms of the deflection and response velocities vectors. We can now write the discretized PDE as a first – order system of ordinary differential equations.

$$\begin{bmatrix} \mathbf{0} & \mathbf{M} \\ \mathbf{I} & \mathbf{0} \end{bmatrix} \begin{bmatrix} \dot{\boldsymbol{\eta}} \\ \dot{\mathbf{u}} \end{bmatrix} + \begin{bmatrix} \mathbf{K} & \mathbf{C} \\ \mathbf{0} & -\mathbf{I} \end{bmatrix} \begin{bmatrix} \boldsymbol{\eta} \\ \mathbf{u} \end{bmatrix} = \begin{bmatrix} \mathbf{F} \\ \mathbf{0} \end{bmatrix}. \tag{4.7.4}$$

Each entry in the matrices of (4.6.4) is a $N_B \times N_B$ matrix. This is a system of $2N_B$ equations. More specifically, rows $i = 3, ..., N_B - 2$ are the discretized equations of motion for the inner stencil points, given by relation (4.7.2a) and the rows $i = N_B + 1, ..., 2\,\mathrm{N}_B$ are the discretized equations incorporating the response velocity into the dynamical system, relation (4.7.2b). **K, C** are the equivalent stiffness and damping matrices of the system defined in detail below.
The rows $i = 1, 2, N_B - 1, N_B$ are discretized equivalent forms of the boundary conditions; more specifically, we have for the clamped end

$$\eta_1 = 0, \left(\mathbf{FD}_1\right)_1 \cdot \boldsymbol{\eta} = 0 \tag{4.7.5a,b}$$

and for the free end

$$\begin{aligned} &\left(\mathbf{FD}_1\right)_{N_B} \cdot \left(\mathbf{D}^T \cdot \left(\mathbf{FD}_2\right)_{N_B} \cdot \boldsymbol{\eta}\right) + \boldsymbol{\mu}^T \cdot \left(\left(\mathbf{FD}_3\right)_{N_B} \cdot \mathbf{u}\right) = 0, \\ &\mathbf{D}^T \cdot \left(\left(\mathbf{FD}_2\right)_{N_B} \cdot \boldsymbol{\eta}\right) + \boldsymbol{\mu}^T \cdot \left(\left(\mathbf{FD}_2\right)_{N_B} \cdot \mathbf{u}\right) = 0 \end{aligned} \tag{4.7.7a,b}$$

The terms of the form $\left(\mathbf{FD}_m\right)_j$ in Eqs. (4.7.6) – (4.7.7) denote the j – th row and m – th order derivative stencil approximated using fourth-order finite difference scheme in the collocation points grid. We also define the flexural rigidity and viscoelastic coefficient vectors as

$$\mathbf{D} = \left[D_1, D_2, ..., D_{N_B} \right]^T, \ \boldsymbol{\mu} = \left[\mu_1, \mu_2, ..., \mu_{N_B} \right]^T, \tag{4.7.8}$$

so that the present numerical model can handle varying thickness distributions. In the sequel, the flexural rigidity and the viscoelastic coefficient will be chordwise constant.

We now shall inspect the entries of the matrices in relation (4.7.4) in more detail. We start with the matrix multiplying the $\left[\dot{\boldsymbol{\eta}}, \dot{\mathbf{u}}\right]^T$ vector. The matrix **M** is the equivalent «mass matrix» of the system. It is created as follows

$$\mathbf{M} = \underbrace{\begin{bmatrix} 0 & & & & & & 0 \\ & 0 & & & & & \\ & & m_3 & & & & \\ & & & \ddots & & & \\ & & & & m_{N_B-2} & & \\ & & & & & 0 & \\ 0 & & & & & & 0 \end{bmatrix}}_{N_B} \tag{4.7.9}$$

Note that the first and last two rows of the matrix are zero. This happens because the boundary conditions are not in any way dependent on the mass.

The **I** matrix is the $N_B \times N_B$ unit matrix. We move on to the matrix multiplying the vector $\left[\boldsymbol{\eta}, \mathbf{u}\right]^T$. The **K** entry matrix is the equivalent «stiffness matrix» of the system. It is defined as

$$\mathbf{K} = \underbrace{\begin{bmatrix} 1 & & & \dots & 0 \\ (\mathbf{FD}_1)_{21} & (\mathbf{FD}_1)_{22} & & \dots & (\mathbf{FD}_1)_{2,N_B} \\ \dots & \dots & \left(\mathbf{FD}_2\mathbf{D}_{diag}\mathbf{FD}_2\right)\Big|_{N_B-2}^{3} & \dots & \dots \\ (\mathbf{FD}_1)_{N_B-1,1} \cdot D_1 \cdot (\mathbf{FD}_2)_{N_B-1,1} & (\mathbf{FD}_1)_{N_B-1,2} \cdot D_2 \cdot (\mathbf{FD}_2)_{N_B-1,2} & & \dots & (\mathbf{FD}_1)_{N_B-1,N_B} \cdot D_{N_B} \cdot (\mathbf{FD}_2)_{N_B-1,N_B} \\ D_1 \cdot (\mathbf{FD}_2)_{N_B,1} & D_2 \cdot (\mathbf{FD}_2)_{N_B,2} & & \dots & D_{N_B} \cdot (\mathbf{FD}_2)_{N_B,N_B} \end{bmatrix}}_{N_B} \tag{4.7.10}$$

The first two lines of matrix **K** are the discretized forms of the clamped end boundary conditions, while the last two are the terms of the free end boundary conditions that multiply the deflection vector $\boldsymbol{\eta}$. The inner part of the **K** matrix is the fourth derivative stencil matrix multiplied appropriately by the flexural rigidity at the collocation points. The term $\mathbf{D}_{diag}$ is a square $N_B \times N_B$ matrix containing the flexural rigidity values in its main diagonal.

The **C** matrix is the «damping matrix» of the dynamical system. It is defined as

$$\mathbf{C} = \mathbf{RD} + \mathbf{FD}_2 \cdot \boldsymbol{\mu}_{diag} \cdot \mathbf{FD}_2 , \tag{4.7.11}$$

where $\mathbf{RD}$ is the Rayleigh damping matrix obtained as explained in more detail in Appendix. The last two rows of the **C** matrix contain the terms that multiply the response velocity vector $\mathbf{u}$, in a similar fashion with the last two rows of the stiffness matrix that contain the terms that multiply the deflection vector $\boldsymbol{\eta}$ in the free end boundary conditions. The $\boldsymbol{\mu}_{diag}$ term in Eq.(4.7.11) is a square matrix with the same properties as $\mathbf{D}_{diag}$, and contains the values of the viscoelastic coefficient in the collocation points, allowing (at least in theory) the treatment of varying stiffness profiles.

In the RHS of Eq. (4.7.4) the term $\mathbf{F}$ is the loading vector. It is defined as

$$\mathbf{F} = \mathbf{f}\left(\boldsymbol{\eta}, \mathbf{u}\,; t\right) - \mathbf{C}_D \cdot \mathrm{diag}\left(\left|\mathbf{u}\right| \cdot \mathbf{u}^T\right), \tag{4.7.12}$$

where the first term in the RHS is the hydrodynamic pressure and acceleration terms due to the body – fixed reference frame being non – inertial.

$$\mathbf{f}\left(\boldsymbol{\eta}, \mathbf{u}\,; t\right) = \rho\left[\frac{d\boldsymbol{\Phi}_B\left(t\right)}{dt} + \boldsymbol{\Gamma}_B\left(t\right) \cdot \mathbf{e}\left(t\right)\right] - \mathbf{Ma}\left(t\right) \tag{4.7.13}$$

where $\mathbf{e}\left(t\right) = \left(\mathbf{V}_\infty + \mathbf{V_G} - \mathbf{V_A}\right) \cdot \boldsymbol{\tau}\left(xcp_i; t\right)$, $\mathbf{a}\left(t\right) = \left(\mathbf{a}\left(xcp_i, t\right) + \mathbf{a}_h\left(t\right)\right) \hat{\mathbf{j}}\left(xcp_i, t\right)$ and $\boldsymbol{\Phi}_B\left(t\right) = \Phi_B\left(xcp_i, t\right)$.

The second term in the RHS of Eq.(4.7/12) is the quadratic damping term, where $\mathbf{C}_D$ is a diagonal matrix defined as follows;

$$\mathbf{C_D} = \underbrace{\begin{bmatrix} 0 & & & & & & 0 \\ & 0 & & & & & \\ & & C_D & & & & \\ & & & \ddots & & & \\ & & & & C_D & & \\ & & & & & 0 & \\ 0 & & & & & & 0 \end{bmatrix}}_{N_B} \tag{4.7.14}$$

We remark that the pressure and reference frame accelerations term $\mathbf{f}(\boldsymbol{\eta}, \mathbf{u}; t)$ is implicitly non – linear with respect to the unknown vectors $\boldsymbol{\eta}, \mathbf{u}$.

We note at this point that the mass, stiffness and damping terms should not be confused with the same matrix notation in finite element methods (FEM).

4.8 Discrete Formulation of the Fully Coupled Hydroelastic Problem

In this subsection the discrete systems of equations comprising the fully – coupled hydroelastic problem are presented in a more organized way.

After discretizing the integral equation Eq. (2.2.11) we obtain the following system of linear equations for each time instant t_n concerning the discrete bound vortices $\boldsymbol{\Gamma}_{B_n} = \boldsymbol{\Gamma}_B(t_n)$:

$$\mathbf{UV}(\boldsymbol{\eta}_n, \mathbf{u}_n) \cdot \boldsymbol{\Gamma}_{B_n} = \mathbf{UV}_W(\boldsymbol{\eta}_n, \mathbf{u}_n) \cdot \boldsymbol{\Gamma}_W + \mathbf{U}_B - \Gamma_{n-1} \cdot \mathbf{UV}_1(\boldsymbol{\eta}_n, \mathbf{u}_n) \Rightarrow$$

$$\boldsymbol{\Gamma}_{B_n} = \mathbf{UV}^{-1}(\boldsymbol{\eta}_n, \mathbf{u}_n) \cdot \left[\mathbf{UV}_W(\boldsymbol{\eta}_n, \mathbf{u}_n) \cdot \boldsymbol{\Gamma}_W + \mathbf{U}_B - \Gamma_{n-1} \cdot \mathbf{UV}_1(\boldsymbol{\eta}_n, \mathbf{u}_n)\right], \tag{4.8.1}$$

where

- $\boldsymbol{\Gamma}_{B_n} = \left[\Gamma_{B_1}, \Gamma_{B_2}, ..., \Gamma_{B_{N_B}}\right]^T$ is the vector containing the intensities of the bound discrete point vortices
- $\mathbf{UV}(\boldsymbol{\eta}_n, \mathbf{u}_n) = w_{ij}^B(\boldsymbol{\eta}_n, \mathbf{u}_n) - w_{i1}^W(\boldsymbol{\eta}_n, \mathbf{u}_n)$ (defined in Eq. 2.4.3.2)
- ΔC_{Pi} (defined in Eq. 2.4.3.2)

- $\mathbf{\Gamma}_{W_n} = \left[\Gamma_{W_1}, \Gamma_{W_2}, ..., \Gamma_{W_{N_W}} \right]^T$ is the vector containing the intensities of the trailing wake point vortices
- $\mathbf{UB} = \left[UB_1, UB_2, ..., UB_{N_B} \right]^T$ where $UB_i = \left(\mathbf{V}_{\mathbf{A}i} - \mathbf{V}_\infty - \mathbf{V}_{\mathbf{G}i} \right) \cdot \mathbf{n}_i \left(\boldsymbol{\eta}_i \right)$ with $\mathbf{n}_i \left(\boldsymbol{\eta}_i \right)$ being the unit normal vector at the i – th collocation point
- Γ_{n-1} is the circulation around the foil at the previous time instant t_{n-1}.

The elastic response of the foil as a thin deformable plate is described by the discrete system of the following first – order ODE's

$$\mathbf{A} \frac{d\mathbf{w}}{dt} + \mathbf{B}\mathbf{w} = \mathbf{Q}\left(\mathbf{w} \right), \tag{4.8.2}$$

where

- $\mathbf{A} = \begin{bmatrix} \mathbf{0} & \mathbf{M} \\ \mathbf{I} & \mathbf{0} \end{bmatrix}$, separate entries defined in Sec. 4.6
- $\mathbf{B} = \begin{bmatrix} \mathbf{K} & \mathbf{C} \\ \mathbf{0} & -\mathbf{I} \end{bmatrix}$, separate entries defined in Sec. 4.6
- $\mathbf{w} = \left[\boldsymbol{\eta}, \mathbf{u} \right]^T$
- $\mathbf{Q}\left(\mathbf{w} \right) = \begin{bmatrix} \mathbf{F} \\ \mathbf{0} \end{bmatrix}$, $\mathbf{F} = \mathbf{f}\left(\boldsymbol{\eta}, \mathbf{u}; t_n \right) - \mathbf{C}_D \cdot \mathrm{diag}\left(\left| \mathbf{u} \right| \cdot \mathbf{u}^T \right)$, separate entries defined in Sec. 4.7
- $f_i \left(\boldsymbol{\eta}, \mathbf{u}; t_n \right) = \frac{1}{2} \rho U^2 \Delta C_{Pi} - m_i \cdot a_i$, where $\mathbf{a}$ has been defined in Sec. 4.7
- $\Delta C_{Pi} \left(\boldsymbol{\eta}_n, \mathbf{u}_n; t_n \right) = \frac{2}{U^2} \left[\frac{1}{\Delta t} \sum_{j=1}^{i} \left[\Gamma_{B_j} \left(t_n \right) - \Gamma_{B_j} \left(t_{n-1} \right) \right] + \frac{\Gamma_{B_i}}{dx_i} \cdot \boldsymbol{\tau}_i \left(\boldsymbol{\eta}_n, \mathbf{u}_n \right) \cdot \left[\mathbf{b}_i \cdot \boldsymbol{\tau}_i \left(\boldsymbol{\eta}_n, \mathbf{u}_n \right) \right] \right]$

  where $\mathbf{b}_i$ is defined in Eq. (2.4.4.3)

4.9 Solution of the Hydrodynamic Coupling Problem

Having presented the formulation of a flapping foil possessing chordwise flexibility, we devise a numerical method to solve the coupled equations of the foil's dynamic response as a

flexible thin plate and the representation theorem for the bound vortex sheet strength. The equations are strongly coupled in a non – linear, implicit manner, rendering the analytical solution of the problem unachievable.

The proposed numerical solution has to take advantage of the fact that many of the terms in the system of ODE's describing the elastic response dynamics of the foil as a flexible plate are linear in nature with respect to the unknown deflection and its first time derivative. However, the non – linearities require special care.

We attempt to establish a scheme to integrate in time the system of ODE's (4.8.2) along with the discretized boundary conditions.

First we approximate the time derivatives of the unknown vector $\mathbf{w}$ at time t_n by first – order backwards differences, i.e.

$$\frac{d\mathbf{w}_n}{dt} = \frac{\mathbf{w}_n - \mathbf{w}_{n-1}}{\Delta t} \tag{4.9.1}$$

We note that explicit time integration is not possible in this problem; the mass matrix $\mathbf{M}$ is singular, thus rendering the matrix $\mathbf{A}$ in (4.8.2) singular, as well. Therefore an implicit time – integration scheme is necessary. Utilizing the Crank – Nicolson time – integration scheme for system (4.8.2) (see e.g. Strauss, 2008), we obtain

$$\mathbf{A}\cdot\left(\frac{\mathbf{w}_n - \mathbf{w}_{n-1}}{\Delta t}\right) = \frac{1}{2}\left(\mathbf{B}\cdot\mathbf{w}_n + \mathbf{Q}_n\right) + \frac{1}{2}\left(\mathbf{B}\cdot\mathbf{w}_{n-1} + \mathbf{Q}_{n-1}\right) \Rightarrow$$

$$\left(\mathbf{A} - \frac{1}{2}\Delta t\cdot\mathbf{B}\right)\cdot\mathbf{w}_n = \left(\mathbf{A} + \frac{1}{2}\Delta t\cdot\mathbf{B}\right)\mathbf{w}_{n-1} + \frac{1}{2}\Delta t\cdot\left(\mathbf{Q}_{n-1} + \mathbf{Q}_n\right) \tag{4.9.2}$$

Given the values of the deflection and response velocity $\mathbf{w}_{n-1} = \left[\boldsymbol{\eta}_{n-1}, \mathbf{u}_{n-1}\right]$ along with the loading vectors $\mathbf{Q}_{n-1}, \mathbf{Q}_n$ relation (4.9.2) constitutes a system of linear equations to be solved for the vector $\mathbf{w}_n$. The matrix that has to be inverted in order to solve the above system is now $\mathbf{A} - \frac{1}{2}\Delta t\mathbf{B}$ which is non – singular.

The difficulty of solving Eq. (4.9.2) lies in the fact that the vector $\mathbf{Q}_n$, the loading term in the current time step, is an implicitly non – linear function of the sought – after vector $\mathbf{w}_n$. This implicit non – linearity is treated by devising an iterative scheme that attempts to solve the system of equations in Eq. (4.9.2) as a linear system successively until the non – linear part of the equation is also satisfied.

Our main objective is to solve the equation in (4.9.2). Transferring all terms in the LHS, we obtain

$$\left(\mathbf{A}-\frac{1}{2}\Delta t\cdot\mathbf{B}\right)\cdot\mathbf{w}_n-\left(\mathbf{A}+\frac{1}{2}\Delta t\cdot\mathbf{B}\right)\mathbf{w}_{n-1}-\frac{1}{2}\Delta t\cdot\left(\mathbf{Q}_{n-1}+\mathbf{Q}_n\right)=0, \tag{4.9.3}$$

or, in a more abstract form

$$\mathbf{G}\left(\mathbf{w}_n\right)=0. \tag{4.9.4}$$

The time – stepping of the Crank – Nicolson scheme has been expressed as a system of non – linear equations the solution of which for each time step is the solution vector of the discretized PDE in (4.9.2). In order to solve (4.9.4) we employ the Newton – Raphson method (see e.g. Burden & Faires, 2010.). Starting with an initial guess $\mathbf{w}_n^0$ (see below) for the solution, we successively calculate better approximations via the formula

$$\mathbf{w}_n^q=\mathbf{w}_n^{q-1}-\mathbf{J}^{-1}\left(\mathbf{w}_n^{q-1}\right)\cdot\mathbf{G}\left(\mathbf{w}_n^{q-1}\right),\ q=1,2,... \tag{4.9.5}$$

The matrix $\mathbf{J}$ is the Jacobian of the function $\mathbf{G}:\mathbb{R}^{2N_B}\to\mathbb{R}^{2N_B}$. It is defined as

$$\mathbf{J}\left(\mathbf{w}\right)=\begin{bmatrix}\frac{\partial G_1}{\partial w_1} & \frac{\partial G_1}{\partial w_2} & \cdots & \frac{\partial G_1}{\partial w_{2N_B}}\\ \frac{\partial G_2}{\partial w_1} & \frac{\partial G_2}{\partial w_2} & \cdots & \frac{\partial G_2}{\partial w_{2N_B}}\\ \vdots & \ddots & & \\ \frac{\partial G_{2N_B}}{\partial w_1} & \frac{\partial G_{2N_B}}{\partial w_2} & \cdots & \frac{\partial G_{2N_B}}{\partial w_{2N_B}}\end{bmatrix} \tag{4.9.6}$$

where $\mathbf{G}\left(\mathbf{w}\right)=\left[G_1\left(\mathbf{w}\right),G_2\left(\mathbf{w}\right),...,G_{2N_B}\left(\mathbf{w}\right)\right]^T$. The calculation of the Jacobian matrix requires knowledge of the partial derivatives of the scalar components $G_i\left(\mathbf{w}\right),i=1,...,2N_B$ of the function $\mathbf{G}\left(\mathbf{w}\right)$. This is not possible, however, since we do not have knowledge of the

explicit dependence of $\mathbf{G}(\mathbf{w})$ on the vector $\mathbf{w}$. Thus we resort to numerical approximation of the partial derivatives. Using the central differences scheme, we calculate

$$\frac{\partial G_i}{\partial w_j} \approx \frac{G_i\left(w_j + h_j\right) - G_i\left(w_j - h_j\right)}{2h_j}, \tag{4.9.7}$$

where h_j is sufficiently small. In practice h_j is selected as a small percentage of $|w_j|$. Therefore, by defining a perturbation vector $\mathbf{h}_n^q = \left[h_1^q, h_2^q, ..., h_{2N_B}^q \right]^T$ we have

$$\mathbf{J}\left(\mathbf{w}_n^q\right) \approx \frac{\mathbf{G}\left(\mathbf{w}_n^q + \mathbf{h}_n^q\right) - \mathbf{G}\left(\mathbf{w}_n^q - \mathbf{h}_n^q\right)}{2\mathbf{h}_n^q} \tag{4.9.8}$$

The approximation of the partial derivatives (4.9.7) involved in the definition of the Jacobian matrix requires successive implementations of the DVM (in a predictor-corrector scheme). We shall first consider perturbations in the values of the deflection vector $\boldsymbol{\eta}_n$, assuming we have fixed the time step. We execute a loop where the DVM is implemented assuming that $\mathbf{w} = \mathbf{w}_n^{q-1}$, except for the fact that $\eta_{n_j} = \eta_{(n-1)_j} + h_j$, $j = 1,..., N_B$. The DVM results enable us to calculate the corresponding value of the function we want to lead to zero, $\mathbf{G}\left(w_{n_j}^{q-1}{}_{(+)}\right)$, where the (+) subscript denotes that the calculation has been implemented for positive perturbation. In a similar fashion, we calculate $\mathbf{G}\left(w_{n_j}^{q-1}{}_{(-)}\right)$. Thus we can immediately approximate the j – th column of the Jacobian matrix. The same procedure holds for perturbations in the velocity portion of the $\mathbf{w}$ vector. When the Jacobian matrix is calculated we calculate the next approximation of the solution through the formula in relation (4.9.5) and recalculate the hydrodynamic data. If the set convergence criteria are met, the iteration is completed, else we continue to find the next approximation. In most cases examined a number of 7-10 iterations were found enough for convergence.

In total, each step of the general iterative scheme requires $4 \cdot N_B$ implementations of the DVM, which makes the solution of the coupled hydroelastic problem far more computationally expensive than that of the hydrodynamic problem. We can partly alleviate this increased computational effort by noting that many of the hydrodynamic data remain

unchanged when the DVM is executed for perturbations of the deflection and response velocity vectors. For example, when the transverse position of collocation points is perturbed, the velocities induced from the wake point vortices do not have to be re – calculated for the rest of the collocation points. In the case of perturbing the elastic response velocities of the collocation points, only the no – entrance boundary condition is modified, which greatly facilitates the implementation of the Jacobian matrix calculation.

The iterative method we have presented requires an approximation of the unknown loading vector $\mathbf{Q}_n$ at each time step. This is rendered feasible by the following procedure; first, when the hydroelastic coupling method proceeds to a new time step, the DVM is implemented by assuming $\mathbf{w}_n^0 = \mathbf{w}_{n-1}$. The solution of the hydrodynamic problem gives a first approximation for the loading vector, $\mathbf{Q}_n^0$. Then an implicit time integration scheme is applied to approximate the solution vector, thus $\mathbf{w}_n^1$ is obtained. Starting with this vector we perform the iterative procedure based on the above Crank – Nicolson time – integration scheme.

To summarize, the solution of the hydroelastic coupling discretized problem consists of the following steps;

- For $t_0 = 0$ set $\mathbf{w}_0^0 = \mathbf{0}$
- At each time step $t_n, n > 0$ set $\mathbf{w}_n^0 = \mathbf{w}_{n-1}$. Given the vector as input to the DVM, along with the prescribed rigid – body kinematics and the hydrodynamic data from previous time steps a first approximation of the loading $\mathbf{Q}_n^0$ is acquired. Perform an implicit time – integration step to obtain a better approximation for the solution vector, $\mathbf{w}_n^1$. With $\mathbf{w}_n^1$ as input, solve the hydrodynamic problem again and acquire the loading (pressure), wake effects and self – induced velocities. Establish the convergence criterion. If it is met, terminate the time step solution. Otherwise proceed to calculation of partial derivatives.
- When the partial derivatives are calculated, use the Jacobian matrix to obtain the next approximation of the solution vector $\mathbf{w}_n^q, q > 1$. For each approximation calculate the hydrodynamic results with the DVM. If the procedure does not converge, use each approximation to obtain the next one.
- When the vector $\mathbf{w}_n^{m_n}$ satisfies the convergence criterion, calculate the corresponding hydrodynamic data and exit the iterative procedure.

- Set $\mathbf{w}_n = \mathbf{w}_n^{m_n}$ and proceed to the next time step.

The flowchart of the described iterative procedure is shown diagrammatically in Figure 4.2.

The way we have set up our numerical model, the solution is essentially the deflection and response velocity distribution over the foil's mean camber line. The hydrodynamic data (vorticity, pressure, forces) are, for all intents and purposes, intermediate steps that are required by the PDE describing the foil's response as a thin, flexible plate. However, they are what is most interesting to us from a performance point of view.

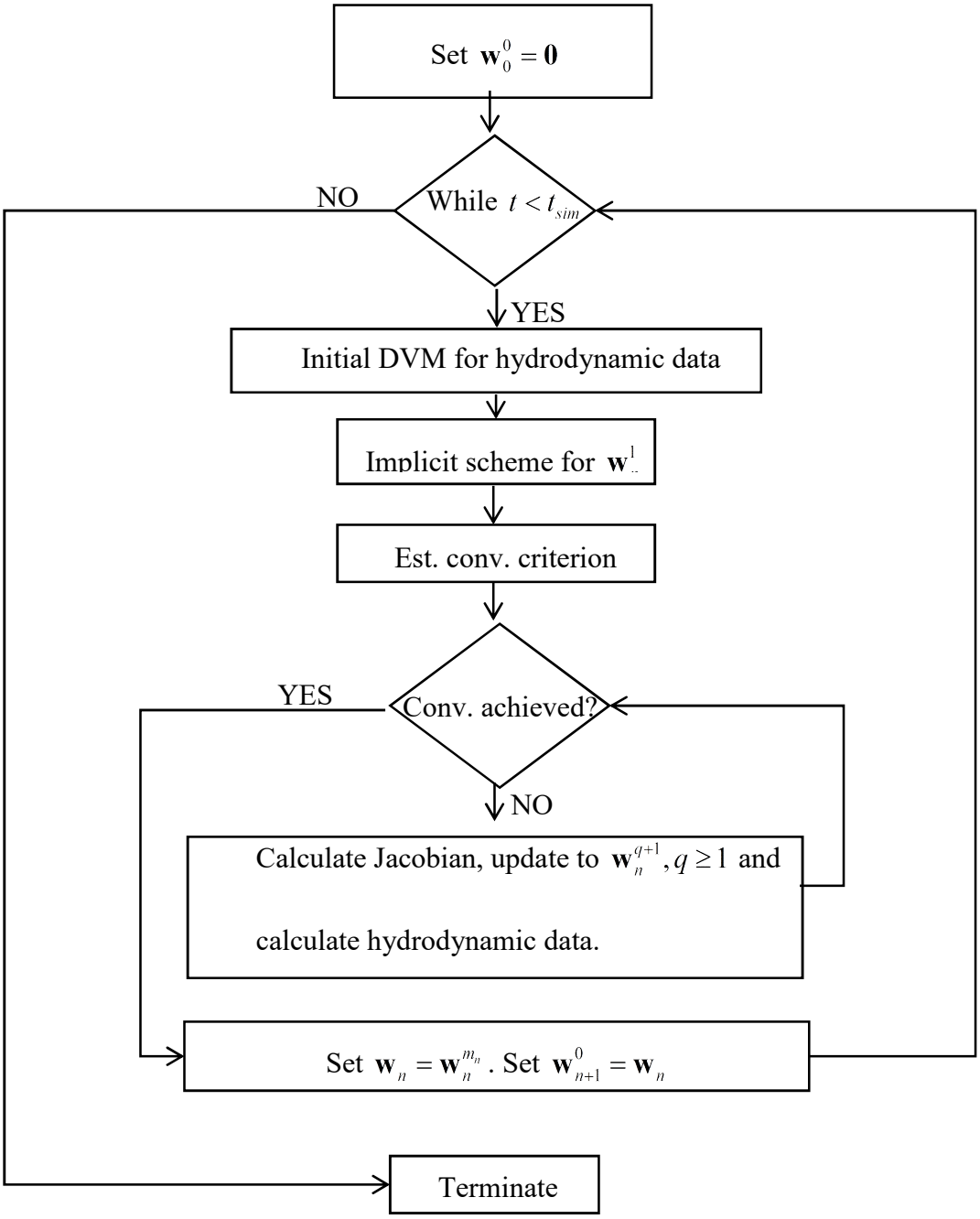

Figure 4.2: Flowchart of hydroelastic coupling solution algorithm

4.10 Numerical Study of Chordwise Flexibility in Flapping Foil Thrusters

The numerical model that treats the coupled problem of a foil performing unsteady motion with chordwise flexibility will be applied to various motion scenarios in an effort to understand the effects of flexibility on the thrust and efficiency of the system.

We deem the study of a heaving – only case a good starting point to this end. In a relatively recent work Paraz et al (2016) studied both experimentally and theoretically the performance of a heaving flexible foil in uniform free – stream velocity. In Table 4.1 the basic data are given.

Table 4.1: Foil and flow parameters – heaving flexible foil

Quantity	Units	Value
Chord length	m	0.12
Free – stream velocity	m/s	0.0612
Flexural rigidity	Nm	0.027
Surface mass density	kg/m^2	4.8
Resonance frequency	rad/s	4.71
Heaving amplitude h_0/c	-	0.035, 0.085, 0.12
Visc. Damping coefficient	Nms	$0.13\cdot10^{-5}$
Quadr. Damp. Coefficient	kg/m^3	960

The resonance frequency has been stated by Paraz et al (2016) to characterize the system of the foil *and* the surrounding fluid, hence it does not coincide with the values proposed by standard elasticity theories, e.g. Euler – Bernoulli. We will present the main points of the theoretical analysis by the previous authors, maintaining their notation.

The problem of the heaving flexible foil is characterized by the following non – dimensional quantities

- Length scale; $c/2 = \mathcal{C}$ (half – chord length)
- Time scale; $\mathcal{C}^2\sqrt{m/D}$ where m is the surface mass distribution and D is the flexural rigidity
- Pressure; $\rho D/m\mathcal{C}^2$
- Frequency; $\left[\mathcal{C}^2\sqrt{m/D}\right]^{-1}$

- Force; $\rho D / m\mathcal{C}$
- Velocity; $\left[\mathcal{C}\sqrt{m/D}\right]^{-1}$

Note that the non – dimensional quantities are depended on the geometric and elastic properties of the foil.

Concerning the resonance frequency, Paraz et al (2016) have concluded that in non – dimensional terms it is equal to

$$\omega_0 = 0.226 \tag{4.10.1}$$

According to Table 4.1, the non – dimensional characteristic frequency $\left[\mathcal{C}^2\sqrt{M/B}\right]^{-1}$ = 20.83rad/s. Multiplying with ω_0 we get the resonance frequency, 4.71 rad/s. This is a result that applies to the coupling of the heaving foil with the surrounding fluid, and is an added mass effect (Newman, 1977). For comparison purposes, the first resonance frequency of the same foil in vacuum is easily found to be equal to 18.31 rad/s. This is an expected result by virtue of the added mass effects associated with oscillations inside water.

We perform runs for three heaving amplitudes; $h_0/c = 0.035, 0.085, 0.12$. The non-dimensional frequency ω/ω_0 is varied in the interval $[0.4, 8]$. The simulation parameters chosen are TSR = 0.35, λ = 3. Results are presented in figure 4.3 for four quantities;

- Trailing edge amplitude / Leading edge amplitude $\alpha_{TE} / \alpha_{LE}$
- Phase lag of trailing edge with respect to leading edge
- Thrust coefficient $f_T = \dfrac{Tm\mathcal{C}}{\rho D}$
- Froude efficiency $\eta = \dfrac{P_{out}}{P_{in}}$

In the upper left figure the trailing edge amplitude is compared to the leading edge amplitude (which is none other than the heaving motion amplitude). The frequency response of the foil's deflection substantially changes when the heaving amplitude is varied. We see

that the maximum value of the response is actually a decreasing function of the heaving amplitude. This is a trademark of non – linear response. The maximum response for each heaving amplitude occurs around $\omega/\omega_0 = 1$, sliding slightly to the left as the heaving amplitude increases. A second resonance frequency is evident in the parameter range tested, although the response amplitude is substantially smaller than that of the first resonance. The sliding of the maximum response is more intense in this second resonance regime. For $h_0/c = 0.035$ the experimental results of Paraz et al (2015) are presented with white – faced squares. The present method displays great agreement with the experimental results. We note here that the experimental results were obtained by authors for stationary heaving foil. However, Paraz et al (2015, Fig.5c) have reported that the trailing edge response is not significantly affected by the forward speed , which agrees with our results.

In the upper – right figure the phase lag of the trailing edge with respect to the heaving amplitude is presented. It is remarkable that the three curves essentially collapse to one. Moreover, the phase lag value around the first resonance frequency is around 90^o, a result expected from the basic theory of linear harmonic oscillators. However, we do not observe a certain pattern for the second resonance.

In the lower left figure results concerning the thrust coefficient are presented. The thrust coefficient defined above is further divided by $\alpha_{LE}{}^2\omega^2$, a characteristic non – dimensional velocity squared. It is maximized for frequencies around the resonance and decreases with increasing heaving amplitude, following the same trend as the trailing edge response. The fact that these quantities are closely related has been stated by many authors. A second peak is observed around the second resonance. In the usual definition of the thrust coefficient, the frequency response is increasing, as we have already seen in Ch. 3. However the added flexibility significantly affects the frequency response of the thrust coefficient. In Figure 4.4 the thrust coefficient and Froude efficiency are shown for $h_0/c = 0.035$, this time utilizing the fluid characteristic force . $0.5\rho U^2 c$. For comparison purposes, we assume that the leading edge suction force is as predicted by the leading edge suction parameter without any losses (see Ch. 2, Sec. 9). This causes the thrust coefficient for the rigid case to scale like the Strouhal number squared, as it has been repeatedly reported by many authors (e.g. Lighthill, 1975)

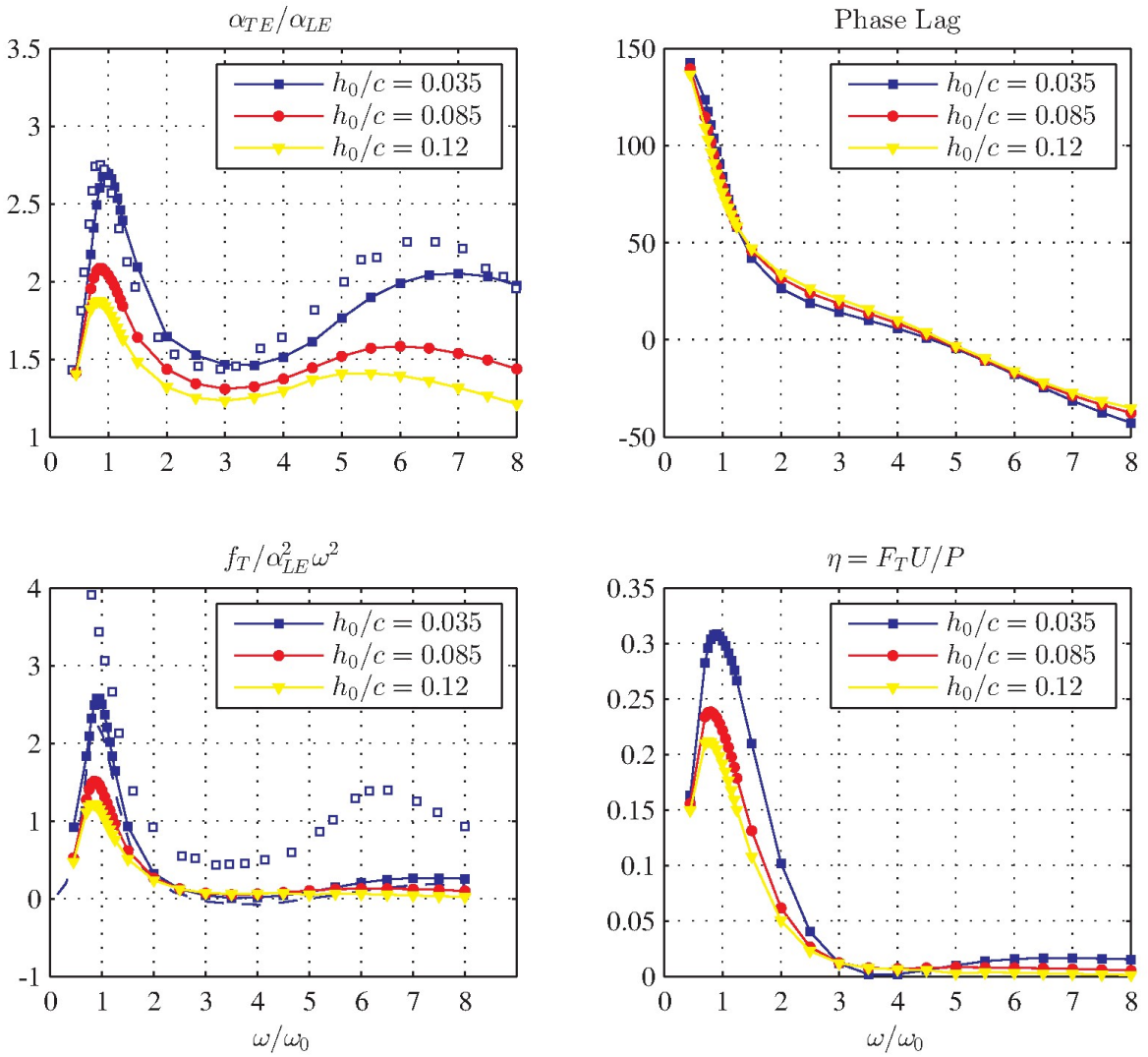

Figure 4.3: Results for heaving flexible foil. In the upper and lower left figures the experimental results of Paraz et al (2015) for are shown in white – faced squares. The theoretical results for the thrust coefficient are shown in dashed lines in the

Contrary to what we have observed in rigid flapping foils, the thrust coefficient in a heaving flexible foil is not monotonically increasing with the excitation frequency, or equivalently the Strouhal number. In fact for frequencies not significantly larger than the resonance frequency the thrust coefficient rapidly drops before rising again as the frequency approaches the second resonance. This substantially different behaviour is a result of the thrust mechanism for a heaving foil; when considering the case of a rigid flapping foil, the only thrust – producing mechanism is the leading edge suction. Adding chordwise flexibility, the pressure forces acting on the foil have a component aligned with the travelling direction, hence producing thrust. Note here that the efficiency of the flexible panel near the first resonance is very close to that predicted by assuming losses due to the leading edge singularity in Fig. 4.3, indicating that the deviation between the corresponding efficiency for the rigid panel is

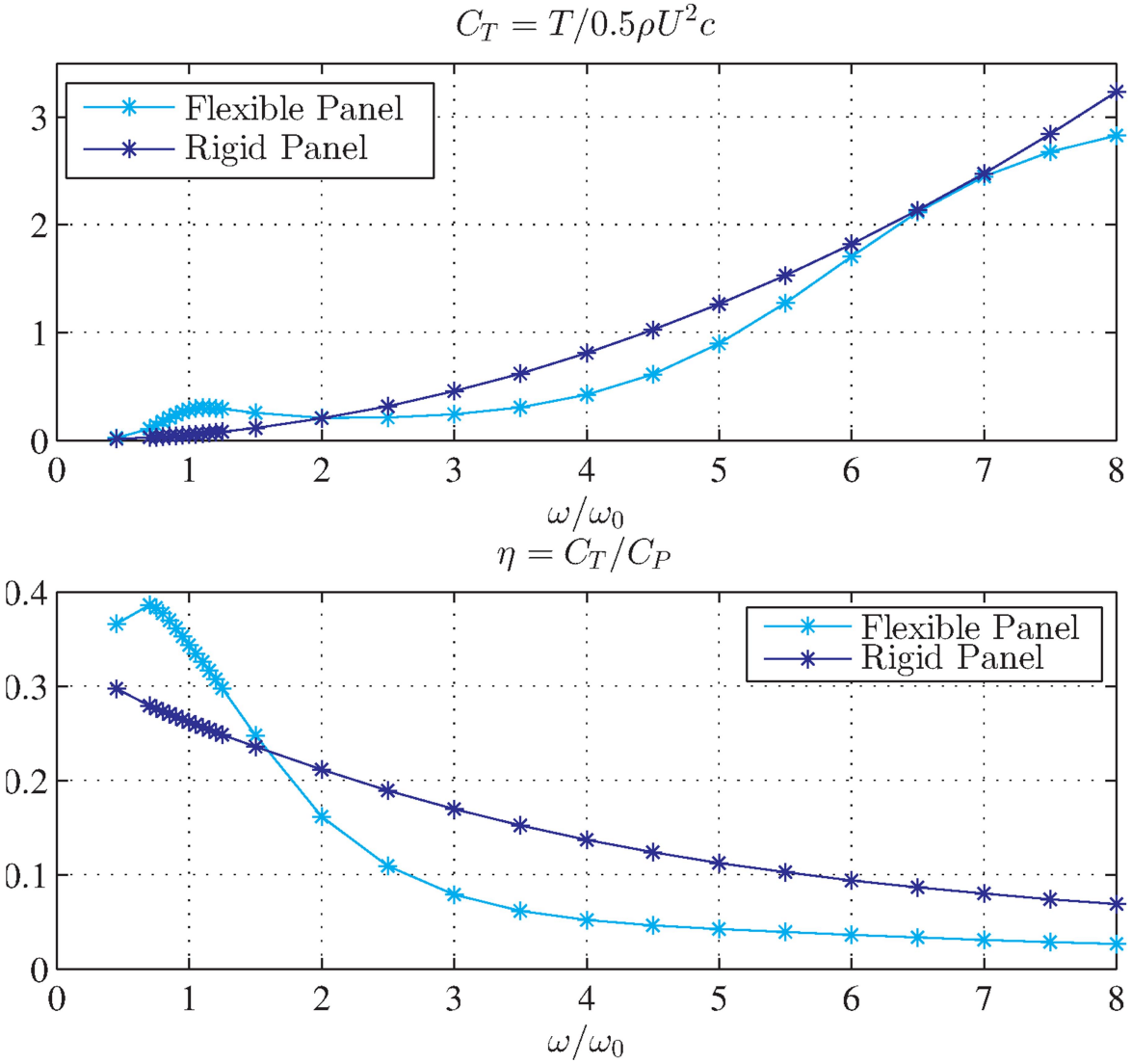

Figure 4.4: Thrust coefficient for $h_0/c = 0.035$. Comparison between flexible panel (cyan curve) and rigid panel (blue curve). Note that for comparison purposes, the presented results assume full attainability of the leading edge suction force in both the flexible and rigid panel case

dominated by the elastic deformation. For larger values of the excitation frequency the effective angle of attack is large enough to trigger the leading edge separation effect, hence the increased efficiency and thrust force displayed by the rigid panel in Fig. 4.4 is only theoretical. The Strouhal number at the first resonance is close to 0.1, hence the effective angle of attack is $\approx 18^o$, meaning that the leading edge separation effect has already started to occur.

Returning to Figure 4.3, dashed lines display the thrust coefficient results of the numerical model devised by Paraz et al (2016), for $h_0/c = 0.035$. We note that the agreement is very good. White – faced squares display the experimental results obtained by the authors.

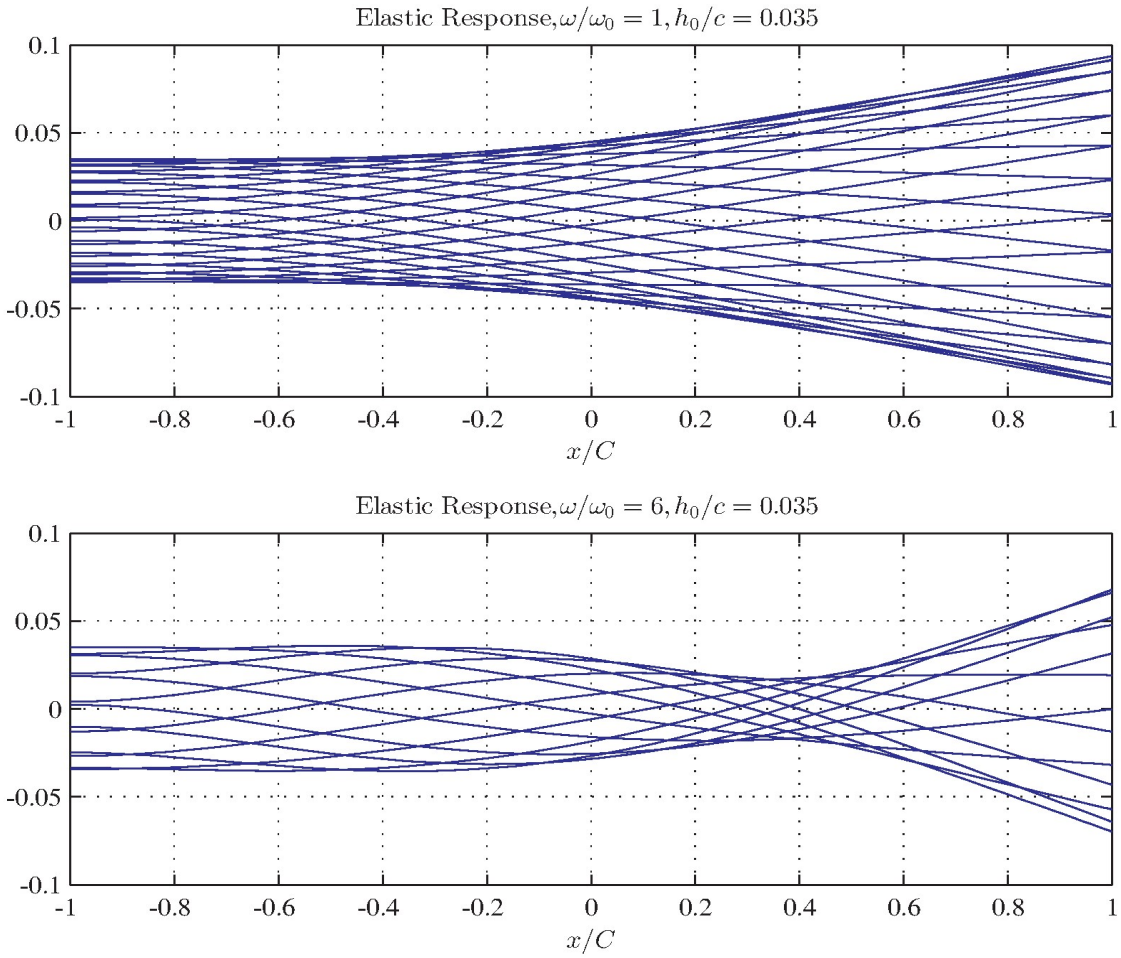

Figure 4.5: Envelope of the foil deflection in the inertia reference frame

The agreement of our numerical model is only qualitative in this case, a fact that also applies to the authors' theoretical model. This is probably attributed to us ignoring any viscous resistive forces in the calculation of thrust; we only consider reactive, i.e. stemming from potential flow pressure forces.

In the lower right figure of Figure 4.3, the Froude efficiency curves are displayed. The trend remains the same; the efficiency is maximized around the first resonant frequency. Corresponding values of the maximum achieved efficiency are 0.31 for $h_0/c = 0.035$, 0.24 for $h_0/c = 0.085$ and 0.21 for $h_0/c = 0.12$. Once again, increasing the excitation amplitude reduces the quantity of interest, in this case the Froude efficiency. In Fig. 4.5 we present the deflection time history for the last period of the heaving motion in the form of successive plots of the chordwise deflection at discrete times. The heaving amplitude is $h_0/c = 0.035$. The results are presented for two values of the non – dimensional frequency, around the first and second resonance. The results agree well with those predicted by Paraz et al (2016).

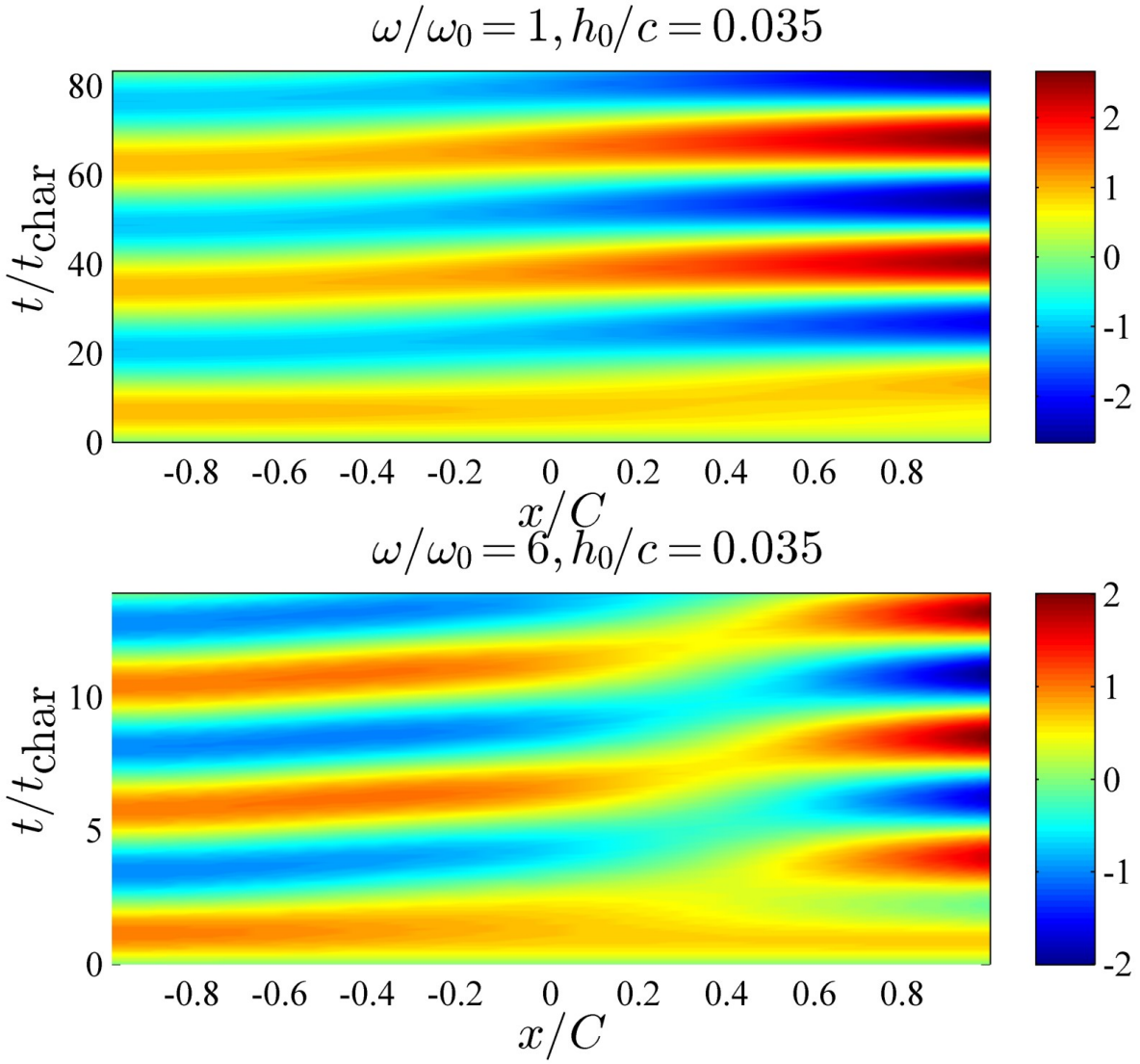

Figure 4.6: Contour plots of the elastic plate deflection around the first two resonant frequencies, for $h_0 / c = 0.035$.

In the region of the second resonance frequency, the response displays a neck at around 2/3 of the chord, due to the second eigenmode excitation. In Fig. 4.6 contour plots are presented for the deflection of the panel near the first two resonant frequencies, again for $h_0 / c = 0.035$. These plots reveal the phase lag between the leading and trailing edge transverse motion. More specifically, this lag is larger for the second resonance. This can easily be explained as follows: Assuming that the Euler – Bernoulli beam theory holds (which constitutes a good approximation in our case), the resulting dispersion relation dictates that the transverse wave speed is proportional to the square root of the response frequency (Elmore & Heald, 1969). Thus, increasing the Strouhal number, the ratio of the

time it takes for he transverse waves to travel along the chord length over the oscillation period is increasing.

The numerical simulations performed for a heaving flexible foil point to a single fact; that the frequency that optimizes the output of a flexible flapping foil thruster, whether we are interested in thrust or efficiency, is close to the resonance frequency of the combined system of foil and surrounding fluid.

We attempt to validate further the hydroelastic coupling model with comparing with the experimental results of Barranyk et al (2012). The foil considered was made of PDMS material that performed simultaneous heaving and pitching motions (in flapping mode). Three cases were studied in total, each with varying stiffness. The stiffness modification in the experimental process was achieved by using a composite foil with rigid forward part and flexible rear part. In each case a different length ratio was used; 15% for the most flexible case (meaning that only the forward 1/6 of the chord is rigid), 50% for the intermediate flexibility case and 100% for the absolutely rigid case.

To simulate the rear flexible part, we make an adjustment in the hydroelastic coupling method. The clamped end in moved downstream to the chordwise point where the rigid front part is connected with the flexible rear part. Thus the boundaries of the hydrodynamic and elastic response problems do not coincide. However nothing changes concerning the coupled solution.

The systematic runs parameters are given in the next table

Table 4.2: Foil and flow parameters – flapping flexible foil

Quantity	Units	Value
Chord length	m	0.20
Free – stream velocity	m/s	0.22
Flexural rigidity	Nm	1.22
Surface mass density	kg/m^2	19.2
Resonance frequency	rad/s	Inf, 26.6, 14.1[1]
Heaving amplitude h_0/c	-	0.4
Pitch amplitude	Deg.	8
Visc. Damping coefficient	Nms	$4.84 \cdot 10^{-5}$
Quadr. Damp. Coefficient	kg/m^3	2304
Strouhal number	St	0.25 – 0.45
Flapping frequency	ω	2.16 – 3.89

[1] For 100%, 50% and 15% rigidity ratio, respectively, according to Barranyk et al (2012)

The Young modulus of the PDMS material is calculated from the authors' information about the structural response of the foils in the fluid, and is found to be close to 3.25 MPa. The thickness of the foil is equal to 1.6 cm. The Strouhal number varies in the interval $[0.25, 0.45]$ where Barranyk et al (2012) reported positive thrust. For smaller values of St the efficiencies reported were negative, something that is not predicted by the present method, probably a product of viscous effects that have not been included in our coupled model. The phase lag between heaving and pitching motion is set to 90^{o}, while the foil pitches about its leading edge. The forward rigid part of the foil acts only on the hydrodynamic response of the foil, hence the leading edge is a boundary for the vorticity distribution only.

In Figure 4.7 we present the results obtained from the present method for the parameter set in table 4.2. In the upper left the results for the thrust coefficient are displayed. As the Strouhal number increases, the thrust coefficient of the 15% rigid foil is consistently larger than that of the 50% and 100% rigid foils. The thrust coefficient of the 50% rigid foil effectively displays improved performance over the 100% rigid one only for the larger Strouhal values tested. We note that the thrust curves obtained are monotonically increasing for all the values of the Strouhal number. This indicates that the resonance frequency of both the 15% and 50% foils is larger than the flapping frequency values considered in this study. This has been, at least qualitatively, predicted by the values of the resonance frequency we have given in table 4.2, which have been obtained by the linear theoretical model of Paraz et al.

The Froude efficiency curves are displayed in the upper right figure. The effect of chordwise flexibility is dramatic in the propulsive efficiency; For the 50% and 100% rigid foils the efficiency reaches a minimum around 11% - 12%, while the 15% rigid case the minimum is close to 17%. Moreover, the efficiency curve for the 15% rigid foil seems to flatten for the largest frequencies tested. Based on the observations made for the heaving flexible foil, we can assume the behaviour of the 15% rigid foil efficiency curve for the subsequent Strouhal numbers. As the flapping frequency approaches the resonance frequency of the foil and surrounding fluid, the curve possibly becomes increasing again. The local peak that will manifest will probably correspond to a relatively small value of efficiency, however. This is because the structural resonance frequency and the optimal flapping frequency, reported in Strouhal numbers between 0.25 and 0.40, are not adequately close to have simultaneously positive effects in the flapping foil thruster considered.

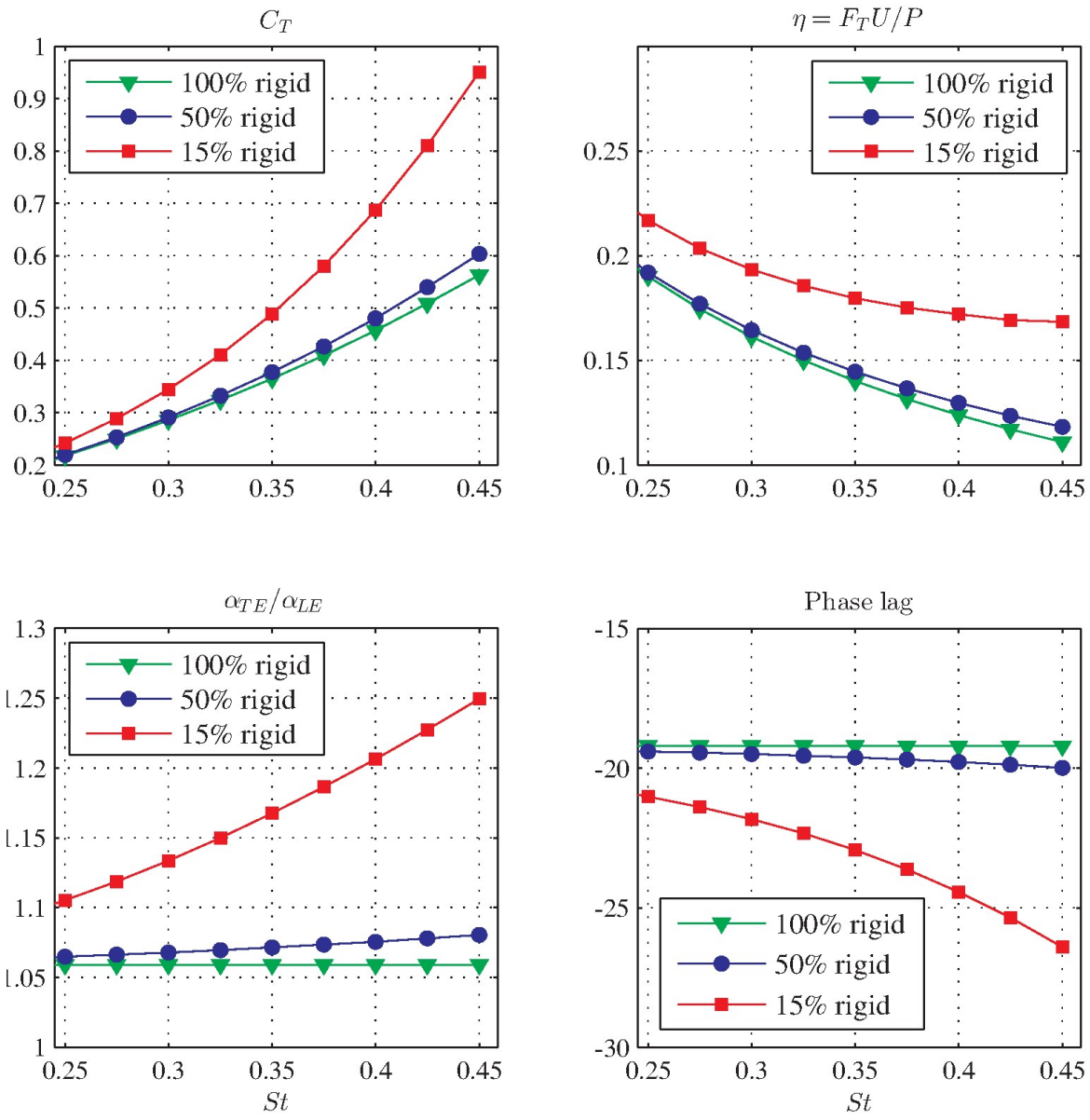

.

Figure 4.7: Systematic results for thrust coefficient (upper left), propulsive efficiency (upper right), trailing to leading edge amplitude ratio (lower left) and phase lag of trailing edge amplitude (lower right). Flapping foil with $h_0 / c = 0.4, \theta_0 = 8^o$ and varying rigid to flexible chord –length ratio

In the lower left plot of Fig. 4.7 the trailing to leading edge response amplitude is presented. The observation that increasing thrust is associated with large trailing edge amplitudes is validated here. The 50% rigid foil shows no significant trailing edge response; its amplitude is mainly a product of the prescribed kinematics. The 15% rigid foil however displays large trailing edge amplitudes, owing to its structural response. These results are consistent with basic momentum consideration in the theory of propellers, where the thrust of

the propulsion device scales like the area swept by it. The increased trailing edge response amplitude of the 15% rigid foil acts as an effective increase in the Strouhal number.

The phase lag of the trailing edge response with respect to the leading edge excitation is presented in the lower right plot of Fig. 4.7. Once again, the 50% rigid foil shows insignificant variations with respect to the 100% rigid foil. The 15% rigid foil shows substantially varying phase lag, which can assume to reach values close to 90^o for flapping frequencies close to its structural resonance.

At this point we note that agreement of the presented method with the experimental data of Barranyk et al (2012) is not expected. First, 3D flow effects are certainly evident in the experimental setup, due to the very low aspect ratio involved (AR = 0.5). Second, the plate the aforementioned authors used was relatively thick, with a sharp leading edge, so it is expected that leading edge vortex shedding significantly affects the flow. Finally, the effective angles of attack attained as the Strouhal number increases are very large. Interestingly, the fact that the thrust coefficient of the most flexible foil is larger than the rigid case is owed to the large values attained by the effective angle of attack (more specifically, for St = 0.45, $a_{\max} \approx 47^o$, leading to significantly deteriorated flow around the plate. The overall trend is that in the case of flapping foils flexibility reduces the thrust coefficient, but increases thrust.

In Fig. 4.8 direct comparison between the presented method results and experimental data of Barranyk et al (2012) is shown for the thrust coefficient and the propulsive efficiency. The experiments of the aforementioned authors display peaks in the propulsive efficiency that are not captured by the present method. They occur at Strouhal numbers St = 0.3 for the most flexible case (15% rigid) and around St = 0.25 – 0.27 for the 100% and 50% rigid plates, respectively. However, the limiting value of the propulsive efficiency seems to be predicted correctly by the present method. The thrust coefficient in the experimental data displays the trend that we have already discussed, although all three curves are consistently below the thrust curves predicted by our model. Apart from the 3D flow effects that we certainly expect to significantly alter the flow around the plates in the experiments, we also expect strong leading edge – trailing edge vortex interactions, which is indicated in velocity plots by Barranyk et al (2012), probably a result of the moderately large thickness and abrupt leading edge geometry of the plates in the experiments.

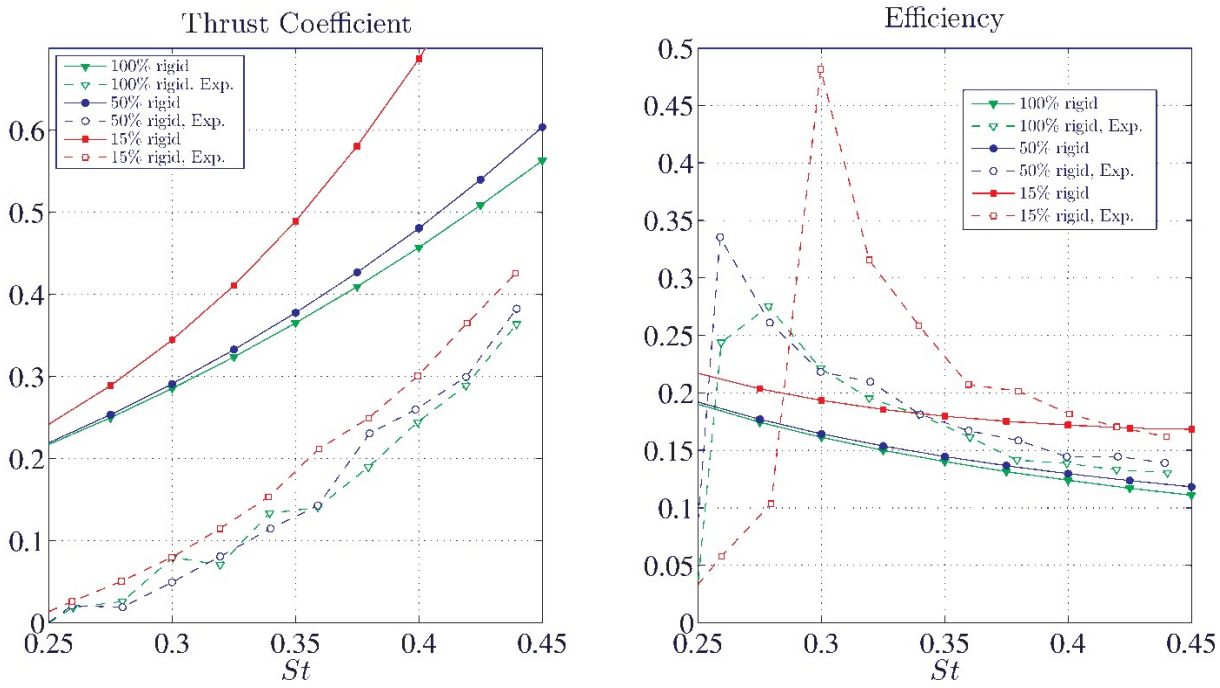

Figure 4.8: Comparison between the present method and experimental results of Barranyk et al (2012).

. We conclude that, comparing our results with the aforementioned authors', we can only hope to reproduce the general trend: increase of both thrust and efficiency.

5. Conclusions – Suggestions for future work

A hydroelastic coupling model has been developed that successfully solves the problem of a thin symmetrical foil, modelled as a flat plate, in unsteady flow with chordwise flexibility. We saw that the high efficiency of flapping foil thrusters is enhanced by addition of chordwise flexibility. Generally, for the same kinematic parameters, proper flexibility addition leads to increased efficiency at the expense of thrust. However, increasing the flapping frequency we can achieve the thrust of the rigid case with improved efficiency.

The present model allows for additions and modifications. The thickness effects can be incorporated by applying the methodology in this thesis in a BEM solver, which is straightforward at this point. The hydrodynamics part of the method can be enhanced by modelling effects such as leading edge separation. The trailing wake can be updated so as to be freely deformed by the vortex interactions. As for the elasticity part of the solution, curvilinear beam models are required to obtain more accurate solutions in cases of large deformation.

Suggestions for future work foremostly include extensions of the present method to 3D in both the hydrodynamics and elasticity part. This would allow the study of the spanwise wing deformations under hydrodynamic loading, a significant part of aquatic animals' propulsion. It would be very interesting to apply the present method to other systems than propulsion, e.g. wave energy extraction in renewable energy applications or auxiliary propulsion in ships, with the wing placed under the hull fore. The effect of chordwise flexibility is largely unknown is such applications, not to mention the spanwise flexibility. In the case of auxiliary propulsion where the ship responds to random sea excitations, it would be very interesting to implement an optimum control method based on the present numerical model.

6. References

Adhikari S., Phani A.S. 2007. Rayleigh's classical damping revisited. *International Conference on Civil Engineering in the New Millennium: Opportunities and Challenges*, *Howrah, India, January 2007.*

Alben S. 2008. Optimal flexibility of a flapping appendage in an inviscid fluid. *J. Fluid Mech. (2008), vol. 614, pp. 355–380*

Alben S., Witt C., Baker T.V., Anderson E. & Lauder G.V. 2012. Dynamics of freely swimming flexible foils. *Physics of fluids 24, 051901 (2012)*

Anderson J.M., Streitlien K., Barrett D.S. & Triantafyllou M.S. 1998. Oscillating foils of high propulsive efficiency. *J. Fluid Mech. (1998), vol. 360, pp. 41–72*

Barranyk O., Buckham B.J. & Oshkai P. 2012. On performance of an oscillating plate underwater propulsion system with variable chordwise flexibility at different depths of submergence. *Journal of Fluids and Structures 28 (2012) 152–166*

Belibassakis K.A., Filippas E.S. 2014. Ship propulsion in waves by actively controlled flapping foils. *Applied Ocean Research 52 (2015) 1–11*

Belibassakis K.A., Politis G.K. 2013. Hydrodynamic performance of flapping wings for augmenting ship propulsion in waves. *Ocean Engineering 72 (2013) 227–240*

Belibassakis K.A., Politis G.K., Triantafyllou M.S. 1997. Application of the VLM to the propulsive performance of a pair of oscillating wing-tails. *Proc. 8th Inter. Conference on*

Bisplingshoff R.L., Ashley H. and Halfman R.L. 1983. *Aeroelasticity.* Dover Publications, Inc. (published 1996)

Bose N. 1992. A time – domain panel method for analysis of foils in unsteady motion as oscillating propulsors. *11th Australasian Fluid Mechanics Conference*

Burden R.L., Faires J.D. 2010. *Numerical Analysis, 9th Ed.* Brooks/Cole

Christensen R.M. 1982. *Theory of Viscoelasticity, 2nd Ed.* Academic Press,Inc.

Cleaver D.J., Gursul I., Calderon D.E. & Wang Z. 2014. Thrust enhancement due to flexible trailing-edge of plunging foils. *Journal of Fluids and Structures 51 (2014) 401–412*

Clough R.W., Penzien J. 1995. *Dynamics of Structures, 3rd Ed.* Computers & Structures, Inc.

Connel B. 2006. *Numerical Investigation of the Flow – Body Interaction of Thin Flexible Foils and Ambient Flow.* Submitted to the Dept. of Mech. Eng. in partial fulfilment for the requirements for the degree of Doctor of Philosophy in Ocean Engineering at MIT, June 2006.

De Sousa F., Allen J.J. 2011. Thrust efficiency of harmonically oscillating flexible flat plates. *J. Fluid Mech. (2011), vol. 674, pp. 43–66*

Dewey P.A., Boschitsch B.M., Moored K.W., Stone H.A. & Smits A.J. 2013. Scaling laws for the thrust production of flexible pitching panels. *J. Fluid Mech. (2013), vol. 732, pp. 29–46.*

Dickinson M.H., 1994. The effect of wing rotation on unsteady aerodynamic performance at low Reynolds numbers. *J. Exp. Biol., 192, 179-206*

Ellington C.P., C. Vanderberg, A. Wilmott & A. Thomas, 1996. Leading edge vortices in insect flight. *Nature, 384, 626-630.*

Elmore W.C., Heald M.A. 1969. *Physics of Waves*. McGraw – Hill, Inc.

Filippas E.S., Belibassakis K.A. 2014. Hydrodynamic analysis of flapping-foil thrusters operating beneath the free surface and in waves. *Engineering Analysis with Boundary Elements 41 (2014) 47–59*

Filippas E.S., Belibassakis K.A. 2014. Hydrodynamic analysis of flapping-foil thrusters operating beneath the free surface and in waves. *Engineering Analysis with Boundary Elements 41 (2014) 47–59*

G.I. Taylor 1951. Analysis of the Swimming of Microscopic Organisms. *Proc. Roy. Soc., A,* 209: 447-61 (1951)

Garrick I.E. 1936. Propulsion of a flapping and oscillating airfoil. *NACA Report No. 567, 1936.*

Gopalkrishnan R., Triantafyllou M.S. & Triantafyllou G.S. 1994. Active Vorticity Control in a Shear Flow Using a Flapping Foil. *J. Fluid. Mech. (1994) Vol. 274, pp. 1 – 21*

Graff K.F. 1975. *Wave Motion in Elastic Solids.* Dover Publications, Inc., New York

Gursul I., C. Ho, 1992. High aerodynamic loads on an airfoil submerged in an unsteady stream. *AIAA J., 30, 1117-1119.*

Heathcote S., Gursul I. 2007. Flexible Flapping Airfoil Propulsion at Low Reynolds Numbers. *AIAA journal Vol. 45, No. 5*

Heathcote S., Martin D. & Gursul I. 2004. Flexible Flapping Airfoil Propulsion at Zero Freestream Velocity. *AIAA journal vol. 42, no. 11*

Heathcote S., Wang Z. & Gursul I. 2008. Effect of spanwise flexibility on flapping wing propulsion. *Journal of Fluids and Structures 24 (2008) 183–199*

James R.M. 1972. On the Remarkable Accuracy of the Vortex Lattice Method. *Computer Methods in Applied Mechanics and Engineering Vol. 1, p. 59 – 79*

Kancharala A.K., Philen M.K. 2016. Optimal chordwise stiffness profiles of self-propelled flapping fins. *Bioinspir. Biomim.11(2016)056016*

Katz J., Weihs D. 1978. Hydrodynamic propulsion by large amplitude oscillation of an airfoil with chordwise flexibility. *J. Fluid Mech. (1978), vol. 88, pad 3, pp. 486497*

Katz, J. & Plotkin, A. 1991. *Low – Speed Aerodynamics*. McGraw – Hill

Kerwin J.E. 2001. *Lecture Notes – Hydrofoils and Propellers.* MIT

Kier T.M. 2005. Comparison of Unsteady Aerodynamic Modelling Methodologies with respect to Flight Loads Analysis *Proc. of AIAA Atmospheric Flight Mechanics Conference, August 2005.*

Koochesfahani M.M. 1989. Vortical Patterns in the Wake of an Oscillating Airfoil. *AIAA Journal vol. 27, no. 9, september 1989, p. 1200 – 1205*

La Mantia M., Dabnichki P. 2009. Unsteady panel method for flapping foil. *Engineering Analysis with Boundary Elements 33 (2009) 572–580*

La Mantia M., Dabnichki P. 2011. Influence of the wake model on the thrust of oscillating foil. *Engineering Analysis with Boundary Elements 35 (2011) 404–414*

La Mantia M., Dabnichki P. 2012. Added mass effect on flapping foil. *Engineering Analysis with Boundary Elements 36 (2012) 579–590*

Landau L.D., Lifschitz E.M. 1976. *Course of Theoretical Physics, Vol. 1: Mechanics. 3rd Ed.* Elsevier Ltd.

Lighthill J. 1975. *Mathematical Biofluiddynamics.* Society for Industrial and Applied Mathematics.

Lighthill, M. J. 1969. Hydromechanics of aquatic animal propulsion. *Ann. Rev. Fluid Mech., 1 413-446.*

Lighthill, M. J. 1970 Aquatic animal propulsion of high hydromechanical efficiency. *J. Fluid Mech., 44, 265-301.*

Lindsey, C.C. 1978. Form, function, and locomotory habits in fish, p. 1-100. *Fish physiology. Vol. II. Academic Press, New York.*

Luo H., Yin B. & Doyle J.F. 2010. A 3D computational study of the flow-structure interaction in flapping flight. *48th AIAA Aerospace Sciences Meeting Including the New Horizons Forum and Aerospace Exposition 4 - 7 January 2010, Orlando, Florida*

Maxworthy T., 1979. Experiments on the Weis-Fogh mechanism of lift generation by insects in hovering flight. Part I. Dynamics of the fling. *J. Fluid Mech., 93, 47-63.*

Michelin S., Llewellyn Smith S.G. 2009. Resonance and propulsion performance of a heaving flexible wing. *Physics of fluids 21, 071902 (2009)*

Moran J. 1984. *An Introduction to Theoretical and Computational Aerodynamics.* John Wiley & Sons, Inc.

Newman, J.N. 1977. *Marine Hydrodynamics.* MIT Press

Pan Y., Dong X., Zhu Q., Yue D.K.P. 2012. Boundary-element method for the prediction of performance of flapping foils with leading-edge separation. *J. Fluid Mech. (2012), vol. 698, pp. 446–467*

Paraz F., Eloy C. & Schouveiler L. 2015. Experimental study of the response of a flexible plate to a harmonic forcing in a flow. *C. R. Mecanique, 342, 532–538 (2014).*

Paraz F., Schouveiler L. & Eloy C. 2016. Thrust generation by a heaving flexible foil: Resonance, nonlinearities, and optimality. *Physics of Fluids 28(1):011903 January 2016*

Politis G.K. 2005. *The boundary element method for 3-d fluid flow problems*. Lecture notes

Politis G.K. 2011. Application of a BEM time stepping algorithm in understanding complex unsteady propulsion hydrodynamic phenomena. *Ocean Engineering 38 (2011) 699–711*

Politis G.K., Tsarsitalidis V. 2009. Simulating Biomimetic (flapping foil) Flows for Comprehension, Reverse Engineering and Design. *First International Symposium on Marine Propulsors*

Politis G.K., Tsarsitalidis V. 2014. Flapping wing propulsor design: An approach based on systematic 3D-BEM simulations. *Ocean Engineering 84 (2014) 98–123*

Prandtl L.1924. Uber die Entstehung von Wirbeln in einer idealen Flussigkeit. *Vortrage zur Hydro- und Aerodynamik*, Berlin, 1924. p. 25.

Prempraneerach P., Hover FS. & Triantafyllou M.S. 2013. The effect of chordwise flexibility on the thrust and efficiency of a flapping foil. *Proceedings of the 13 th International Symposium on Unmanned Untethered Submersible Technology: Special session on bioengineering research related to autonomous underwater vehicles*, New Hampshire

Quinn D.B., Lauder G.V. & Smits A.J. 2014. Scaling the propulsive performance of heaving flexible panels. *J. Fluid Mech. (2014), vol. 738, pp. 250–267*

Quinn D.B., Lauder G.V. & Smits A.J. 2015. Maximizing the efficiency of a flexible propulsor using experimental optimization. *J. Fluid Mech. (2015), vol. 767, pp. 430–448*

Rayleigh, L. 1877. *Theory of Sound.* Dover Publications, New York, 1945 (re-issue, second edition)

Read D.A., Hover F.S. & Triantafyllou M.S. 2003. Forces on oscillating foils for propulsion and maneuvering. *Journal of Fluids and Structures 17 (2003) 163–183*

Richards A.J., Oshkai P. 2015. Effect of the stiffness, inertia and oscillation kinematics on the thrust generation and efficiency of an oscillating-foil propulsion system. *Journal of Fluids and Structures 57 (2015) 357–374*

Rozhdestvensky K.V., Ryzhov V. A. 2003. Aerohydrodynamics of flapping-wing propulsors. *Progress in Aerospace Sciences 39 (2003) 585–633*

Sfakiotakis M, Lane D.M. & Davies B.C. Review of Fish Swimming Modes for Aquatic Locomotion 1999. *IEEE journal of oceanic engineering, vol. 24, no. 2, april 1999*

Sparenberg, J.A. 2002. Survey of the mathematical theory of fish locomotion, *Journal of Engineering Mathematics 44: 395–448, 2002.*

Strauss W.A. 2008. *Partial Differential Equations. An Introduction.* John Wiley & Sons, Ltd.

Triantafyllou G.S., M.S. Triantafyllou, & M.A. Grosenbaugh. 1993. Optimal Thrust Development in Oscillating Foils withApplication to Fish Propulsion. *J. Fluids Struct., 7, 205-224.*

Triantafyllou G.S., M.S. Triantafyllou, & M.A. Grosenbaugh. 1993. Optimal Thrust Development in Oscillating Foils withApplication to Fish Propulsion. *J. Fluids Struct., 7, 205-224.*

Triantafyllou M.S., Techet A.H., Hover F.S. 2003. *Review of Experimental Work in Biomimetic Foils*

Triantafyllou M.S., Triantaafyllou M.S. & Gopalkrishnan R. 1991. Wake mechanics for Thrust Generation in Oscillating Foils. *Phys. Fluids. A 3 (12), December 1991*

Tuncer I.H., Platzer M.F. 2000. Computational Study of Flapping Airfoil Aerodynamics. *Journal of Aircraft, 37, 514-520*

Videv T.A., Doi Y. & Mori K. 1993. Numerical Study of Flow and Thrust Produced by Heaving and Combined Oscillations of 2D Hydrofoil. *Journal of The Society of Naval Architects of Japan, Vol. 174, p. 55 – 70*

Wu T.Y. 1961. Swimming of a Waving Plate. *J. Fluid Mech. Vol. 10, pp. 321 – 344.*

Wu T.Y. 1971. Hydromechanics of swimming propulsion. *J. Fluid Mech., vol. 46, part 2, p.337-355*

Yamaguchi H., Bose N. 1994. Oscillating Foils for Marine Propulsion. *Proceedings of the Fourth International Offshore and Polar Engineering Conference*

Zhang X., Zhou C. 2010. Numerical investigation on the propulsive efficiency of flapping airfoil with different up-down plunge models. *27th international congress of the aeronautical sciences*

Zhu Q. 2007. Numerical Simulation of a Flapping Foil with Chordwise or Spanwise Flexibility. *AIAA Journal Vol. 45, No. 10, October 2007*

Appendix A: Finite Difference Scheme

We present here details about various aspects of the numerical solution of the hydroelastic coupling problem of a flexible thin plate performing unsteady motion in unbounded fluid.
In our model a non – uniform grid of collocation points has been utilized, as explained thoroughly in Ch. 2. The solution of the coupling problem requires the numerical evaluation of space derivatives, most notably the biharmonic operators, ∇^4 and $\nabla^2 D \nabla^2$. Due to the fact that the grid is non – uniform, we cannot resort to expressions of the finite difference stencils from the literature for the approximation of the derivatives involved. Thus, we developed a systematic scheme based on Taylor expansion that provides us with the stencil coefficients.

Assume a stencil around a central point, which shall be called x_i. The stencil extends from the point x_{i-l} to the point x_{i+r} such that $x_{i-l} < x_i < x_{i+r}$ and $l, r \in \mathbb{N}$. For simplicity, the point x_i will be repeatedly referred to as "central point", even in the case when $l \neq r$. Invoking the Taylor formula around the central point for a function $u(x)$, we have

$$u\left(x_{i+j}\right) = u_{i+j} = u_i + \left.\frac{\partial u}{\partial x}\right|_{x_i} \Delta x_j + \left.\frac{1}{2!}\frac{\partial^2 u}{\partial x^2}\right|_{x_i} \left(\Delta x_j\right)^2 + \left.\frac{1}{3!}\frac{\partial^3 u}{\partial x^3}\right|_{x_i} \left(\Delta x_j\right)^3 + \left.\frac{1}{4!}\frac{\partial^4 u}{\partial x^4}\right|_{x_i} \left(\Delta x_j\right)^4 + \ldots \quad \text{(A.1)}$$

for $j = -l, \ldots r$, where $\Delta x_j = x_j - x_i$. Repeating for all j's and taking a linear combination of the resulting expressions, we obtain

$$\begin{aligned} \sum_{j=-l, j\neq 0}^{j=r} a_j u_{i+j} = \left(\sum_{j=-l, j\neq 0}^{j=r} a_j \right) u_i + \left.\frac{\partial u}{\partial x}\right|_{x_i} \sum_{j=-l, j\neq 0}^{j=r} a_j \left(\Delta x_j\right) + \left.\frac{1}{2!}\frac{\partial^2 u}{\partial x^2}\right|_{x_i} \sum_{j=-l, j\neq 0}^{j=r} a_j \left(\Delta x_j\right)^2 + \\ + \left.\frac{1}{3!}\frac{\partial^3 u}{\partial x^3}\right|_{x_i} \sum_{j=-l, j\neq 0}^{j=r} a_j \left(\Delta x_j\right)^3 + \left.\frac{1}{4!}\frac{\partial^4 u}{\partial x^4}\right|_{x_i} \sum_{j=-l, j\neq 0}^{j=r} a_j \left(\Delta x_j\right)^4 + \ldots \end{aligned} \quad \text{(A.2)}$$

where a_j, $j = -l, \ldots r$ are unknown coefficients. Setting $(1/k!) \cdot \sum_{j=-l, j\neq 0}^{r} a_j \left(\Delta x_j\right)^k = b_k$ in Eq.(A.2), we obtain

$$\sum_{j=-l, j\neq 0}^{j=r} a_j u_{i+j} - b_0 u_i = b_1 \left.\frac{\partial u}{\partial x}\right|_{x_i} + b_2 \left.\frac{\partial^2 u}{\partial x^2}\right|_{x_i} + b_3 \left.\frac{\partial^3 u}{\partial x^3}\right|_{x_i} + b_4 \left.\frac{\partial^4 u}{\partial x^4}\right|_{x_i} + b_5 \left.\frac{\partial^5 u}{\partial x^5}\right|_{x_i} + \ldots \quad \text{(A.3)}$$

Suppose now that we want to approximate the first derivative with 4th – order accuracy. Setting $b_1 = 1,\ b_2 = b_3 = b_4 = 0$ in Eq.(A.3), we have

$$\left.\frac{\partial u}{\partial x}\right|_{x_i} = \sum_{j=-l,j\neq 0}^{j=r} a_j u_{i+j} - b_0 u_i - b_5 \left.\frac{\partial^5 u}{\partial x^5}\right|_{x_i} = \sum_{j=-l,j\neq 0}^{j=r} a_j u_{i+j} - b_0 u_i - \left.\frac{1}{5!}\frac{\partial^5 u}{\partial x^5}\right|_{x_i} \sum_{j=-l,j\neq 0}^{j=r} a_j \left(\Delta x_j\right)^5 + \ldots =$$

$$= \sum_{j=-l,j\neq 0}^{j=r} a_j u_{i+j} - b_0 u_i + O\left(\left[\max\left(\Delta x_j\right)^5\right]\Big|_{j=-l,j\neq 0}^{j=r}\right), \tag{A.4}$$

so the approximation is indeed 4th order accurate, with the relevant scale being $\max\left(\Delta x_j\right),\ j = -l,...,r$. Note that the latter approximation required a set of four linear equations to be solved: $b_1 = 1,\ b_2 = b_3 = b_4 = 0$. Therefore, for this case, l=r= 2 and the set of four linear equations gives the values of $a_j,\ j = 1,2,3,4$, Generally, we can easily see that for p – th order approximation of the k – th derivative, the following must hold: l+r = k+p-1.

To validate the proposed scheme, we try to reproduce stencils for uniform grids, which can be found easily in the literature. Consider the aforementioned case for the approximation of the first derivative with fourth degree of accuracy in a uniform grid with Δx = 0.1. The result is known to be equal to

$$\frac{\left(1/12,-2/3,0,2/3,-1/12\right)}{0.1} = \left(5/6,-20/3,0,20/3,-5/6\right) \tag{A.5}$$

To obtain the coefficients numerically, we set $b_1 = 1,\ b_2 = b_3 = b_4 = 0$. This translates to the following set of equations:

$$\begin{bmatrix} 1 & 1 & 1 & 1 & 1 \\ \Delta x_{-2} & \Delta x_{-1} & \Delta x_0 & \Delta x_1 & \Delta x_2 \\ \left(\Delta x_{-2}\right)^2 & \left(\Delta x_{-1}\right)^2 & \left(\Delta x_0\right)^2 & \left(\Delta x_1\right)^2 & \left(\Delta x_2\right)^2 \\ \left(\Delta x_{-2}\right)^3 & \left(\Delta x_{-1}\right)^3 & \left(\Delta x_0\right)^3 & \left(\Delta x_1\right)^3 & \left(\Delta x_2\right)^3 \\ \left(\Delta x_{-2}\right)^4 & \left(\Delta x_{-1}\right)^4 & \left(\Delta x_0\right)^4 & \left(\Delta x_1\right)^4 & \left(\Delta x_2\right)^4 \end{bmatrix} \cdot \begin{bmatrix} a_{-2} \\ a_{-1} \\ a_0 \\ a_1 \\ a_2 \end{bmatrix} = \begin{bmatrix} 0 \\ 1 \\ 0 \\ 0 \\ 0 \end{bmatrix} \Rightarrow$$

$$\Rightarrow \begin{bmatrix} 1 & 1 & 1 & 1 & 1 \\ -0.2 & -0.1 & 0 & 0.1 & 0.2 \\ 0.04 & 0.01 & 0 & 0.01 & 0.04 \\ -0.008 & -0.001 & 0 & 0.001 & 0.008 \\ 0.0016 & 0.0001 & 0 & 0.0001 & 0.0016 \end{bmatrix} \cdot \begin{bmatrix} a_{-2} \\ a_{-1} \\ a_0 \\ a_1 \\ a_2 \end{bmatrix} = \begin{bmatrix} 0 \\ 1 \\ 0 \\ 0 \\ 0 \end{bmatrix} \tag{A.6}$$

The solution to the system of linear equations in Eq.(A.6) is $\left[0.8333, -6.667, 0, 6.667, -0.8333\right]$, which is essentially the same as the result in Eq.(A.5). Notice that the coefficient of the central point $a_0 = -b_0 = -\sum_{j=-l, j\neq 0}^{r} a_j$ is incorporated in the system of equations Eq.(A.6) as the first equation.

Appendix B: Euler – Bernoulli Beam Eigenmodes and Approximation Error

In this section we calculate the first eigenmodes of an Euler – Bernoulli beam in vacuum. The calculations are performed numerically via the finite difference scheme presented in Appendix A.

The equation that described the free vibration of an Euler – Bernoulli beam lying on the [0,*L*] interval is (Graff 1975, Clough & Penzien 1995)

$$EI\frac{\partial^4 w}{\partial x^4}+m\frac{\partial^2 w}{\partial t^2}=0 \tag{B.1}$$

where $D=EI$ is the bending stiffness of the material and *m* is the linear mass distribution. Assuming solution of the form $w(x;t)=W(x)T(t)$, the eigenmodes are obtained as solutions of the following boundary value problem:

$$W^{iv}+\beta^4 W=0,\ \beta^4=\frac{m\omega^2}{EI} \tag{B.2}$$

subject to the following boundary conditions (in the case of cantilever beam which are the same in the case of the flapping foil)

$$W(0)=0,\ W'(0)=0 \text{ (clamped end)} \tag{B.3a}$$

$$W''(L)=0,\ W^{iii}(L)=0 \text{ (free end)} \tag{B.3b}$$

The solution to (B.2) is of the form

$$W(x)=C_1\cos(\beta x)+C_2\sin(\beta x)+C_3\cosh(\beta x)+C_4\sinh(\beta x) \tag{B.4}$$

Differentiating Eq.(B.4) and applying the BC's (B.3a,b) we obtain the eigenvalues of the BVP

$$\beta_1 L = 1.8751,\ \beta_2 L = 4.6941,\ \beta_3 L = 7.8539, \ldots,\ \beta_n L \to \frac{(2n-1)\pi}{2}, n \to \infty \tag{B.5}$$

which are the solutions to the dispersion relation $\cos(\beta L)\cdot\cosh(\beta L)+1=0$.

and, by virtue of (B.2), we have for the eigenfrequencies

$$\omega_n = \frac{\beta_n^{\,2}}{L^2}\sqrt{\frac{EI}{m}} \tag{B.6}$$

We now consider a cantilever beam with length $L = 0.12\,m$, linear mass distribution $m = 4.8\ kg/m^2$ and bending rigidity $EI = 0.027\ Nm^2$. These values correspond to the first example of Chapter 4.
The resonance frequencies are

$$\omega_1 = 18.313\ rad/s,\ 114.76\ rad/s,\ 321.27\ rad/s \tag{B.7}$$

We now attempt to calculate the resonance frequencies and the eigenmodes of this cantilever beam numerically via the finite difference scheme developed. We discretize Eq.(B.1) as follows:

$$\mathbf{M}\frac{d^2\mathbf{w}}{dt^2} + \mathbf{D}\cdot\mathbf{w} = \mathbf{0}, \mathbf{w} = \left[w_1, w_2, \ldots, w_N\right]^T \tag{B.8}$$

where **M** is a diagonal matrix with $M_{ii} = m,\ M_{ij} = 0, i \neq j$ with zero elements in the first and last two lines. These rows represent the boundary conditions, which are independent of the mass distribution. The matrix **D** contains in each inner row the fourth – derivative stencil in the chosen grid $\mathbf{x} = \left[x_1, x_2, \ldots, x_N\right]^T$. The first and last two rows of **D** contain the discretized form of the LHS's of BC's (B.3a,b). We choose second order of accuracy.

Assuming harmonic oscillations, i.e.

$$\mathbf{w}(t) = \mathbf{w}_0 \cdot \mathrm{e}^{i\omega t} \Rightarrow \frac{d^2\mathbf{w}(t)}{dt^2} = -\omega^2 \mathbf{w}_0 \cdot e^{i\omega t} \tag{B.9}$$

and substituting the above Eq. in (B.8), we obtain

$$\left(-\omega^2 \mathbf{M} + \mathbf{D}\right) \cdot \mathbf{w}_0 = 0 \tag{B.10}$$

Since we are looking for non – trivial solutions of Eq.(B.10), we set

$$\det\left(-\omega^2 \mathbf{M} + \mathbf{D}\right) = 0 \tag{B.11}$$

The above relation constitutes an equation to be solved numerically for the resonance frequency ω. To display the capabilities of the proposed finite differences scheme, we employ a non – uniform grid, generated by cosine spacing. The number of collocation points is set equal to 100 and the order of accuracy of the finite difference scheme is set to 4. In Fig. B1 the resulting eigenmodes are displayed compared to the ones predicted by the analytic theory.

The results are almost identical to those predicted by the analytic theory. The resonance frequencies are predicted remarkably well, with errors relative to the theoretical predictions being 0.16%, 0.0003% and 0.078% for the first, second and third resonance frequencies, respectively. Notice that the cosine spacing causes the collocation points grid to become much more dense near the boundaries than it is in the interior of the solution domain.

It is important to study the convergence characteristics of the finite difference scheme developed. To this end we consider the same cantilever beam as before in static load. The equation describing the beam deflection is

$$EI \frac{\partial^4 w}{\partial x^4} = q \tag{B.12}$$

Choosing the static load as $q = -10\ N/m$, we have

$$0.027 \cdot \frac{\partial^4 w}{\partial x^4} = -75 \tag{B.13}$$

Integrating Eq.(B.13) and applying BC's Eqs.(B.3a,b) we obtain the analytic description of the beam's deflection

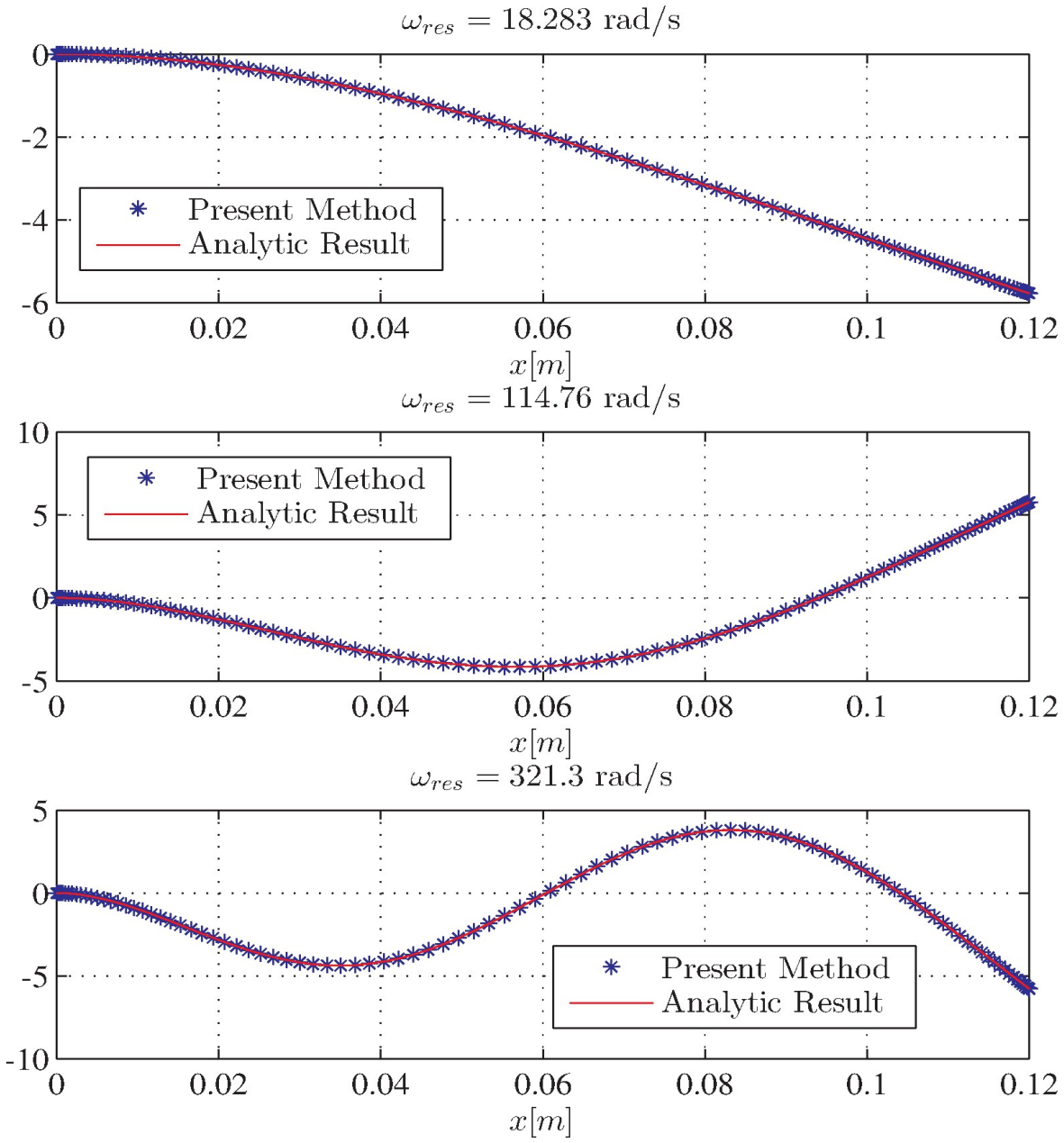

Figure B1: Eigenmodes of Euler Bernoulli beam. Length: 0.12 m, linear mass distribution: 4.8 kg/m^2, bending rigidity: EI = 0.027 Nm^2.

$$w_{an}(x) = -\frac{q}{24EI}x^2\left(x^2 - 4Lx + 6L^2\right) = -15.43x^2\left(x^2 - 0.48x + 0.0864\right)\ [m] \tag{B.14}$$

We calculate the deflection numerically as the solution to a system of linear equations analogous to Eq.(B.10) where now $\mathbf{M}=\mathbf{0}$. In Fig. B2 we display the approximation error for second order of accuracy approximation of the fourth derivative operator in (B.12). The error of each approximation, $w(x;h)$, is calculated with respect to the analytic expression in Eq.(B.14) by means of the L_2 norm as follows:

$$e=\left\|w(x;h)-w_{an}(x)\right\|=\int_0^L\left(w(x;h)-w_{an}(x)\right)^2\,dx \tag{B.15}$$

where h is the maximum distance between collocation points in the grid.

The second order approximation for uniform grid displays fourth order rate of convergence. The results are even more remarkable for the non – uniform, cosine spaced grid, where it seems that the second order approximation has actually convergence rate higher than 6. This can be explained by the fact that when non – uniform grids are utilized, the discretization parameter h is taken as the largest distance in the grid. The cosine spacing

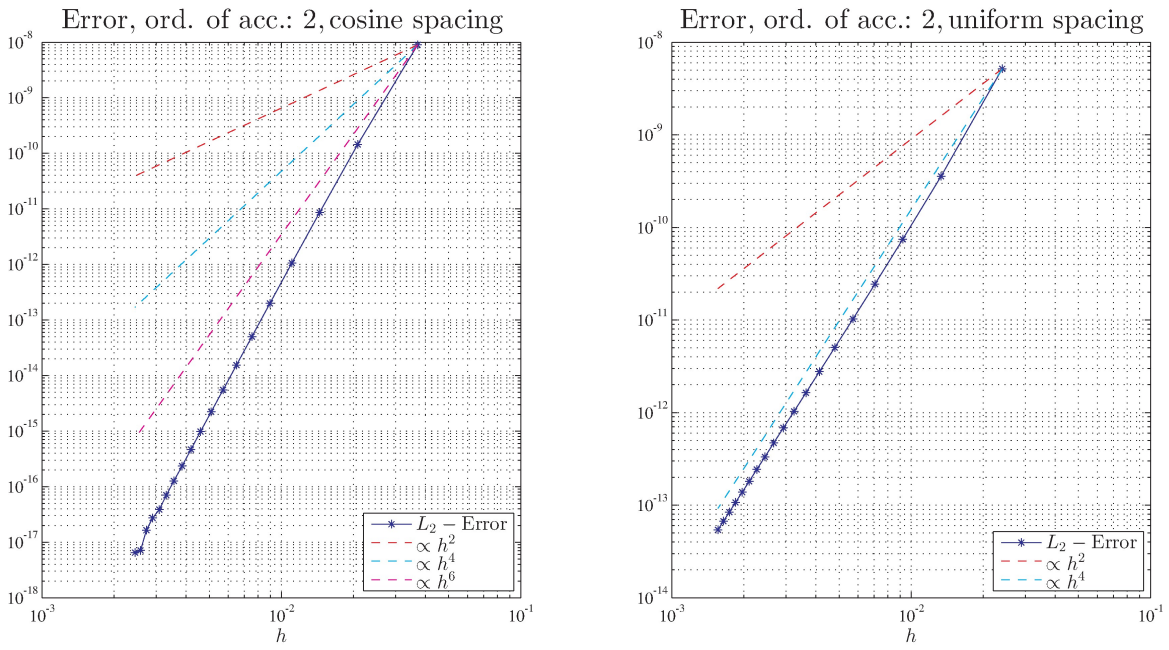

Figure B2: Approximation error for cantilever beam in static loading. Left column: cosine spacing. Right column: Uniform spacing

scheme used here causes the points to gather near the boundaries, which apparently leads to higher convergence rate. After all, the term “n-th order of accuracy approximation” has no clear meaning when non – uniform grids are utilized. In this work we call the approximation

order as we would if the same number of left and right points (with respect to the central point) were utilized for the setup of a finite differences scheme in a uniform grid.

The fourth order approximation leads to errors below machine precision $\approx 10^{-16}$ for the largest of the discretization parameters tested in this case. It also has lost its fourth order rate of convergence due to numerical instabilities at this point. However, its negligible error makes it appealing for applications where the computational effort is large, e.g. the hydroelastic coupling of a flexible thin flat plate with unsteady flow.

Appendix C: Rayleigh Damping

The Rayleigh damping is the first attempt to artificially incorporate damping in a system with many degrees of freedom. In matrix form, it is written as

$$\mathbf{M}\ddot{\mathbf{x}} + \mathbf{C}\dot{\mathbf{x}} + \mathbf{K}\mathbf{x} = \mathbf{F}(t) \tag{C.1}$$

where **M** is the mass matrix and **K** is the stiffness matrix of the system. The matrix **C** is the damping matrix. It generally cannot be known on any physical basis. Rayleigh (1877) proposed the following expression:

$$\mathbf{C} = a\mathbf{M} + \beta\mathbf{K}\,, \tag{C.2}$$

where a, β are scalar coefficients. It can be shown that when linear damping is added to a system with many degrees of freedom it continues to possess normal modes (Adhikari, 2007). The damping ratio ζ for every natural frequency of the system in Eq.(C.1) is given by the expression

$$\zeta_i = \frac{a}{2\omega_i} + \frac{\beta\omega_i}{2} \tag{C.3}$$

A typical plot of this function is given in Fig. C1.

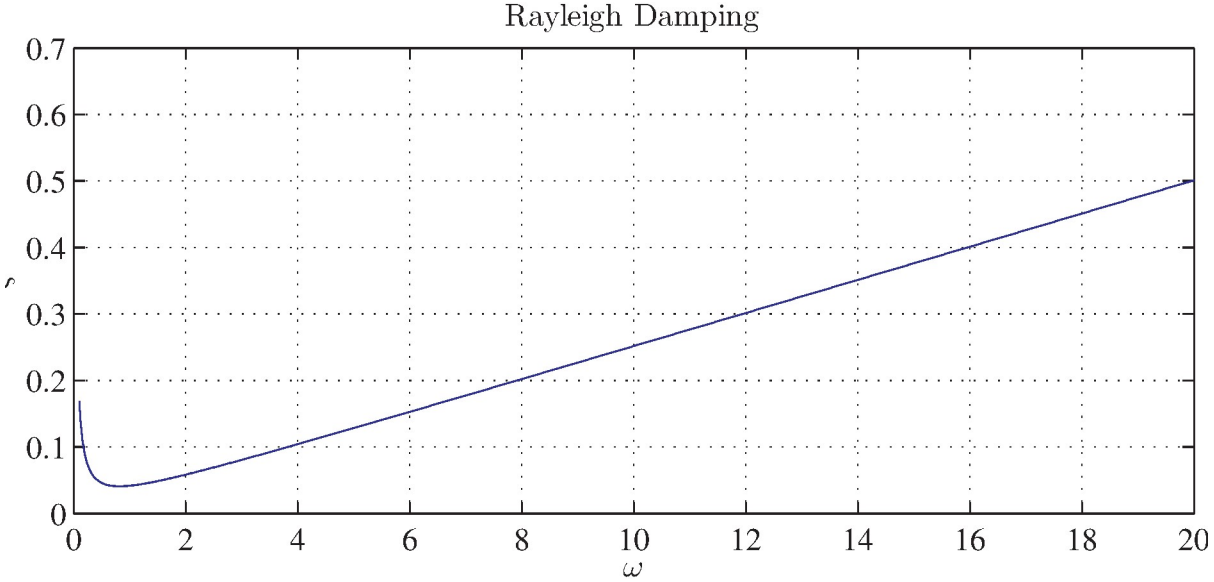

Figure C1: Rayleigh damping: Distribution of damping ratio

Note that the first term in Eq.(C.3) is negligible to the second term. This is the reason Rayleigh's damping is often called "proportional damping".

However, it is not clear how to choose the coefficients a, β in order to acquire an acceptable damping ratio distribution across the eigenfrequencies involved in the MDIF problem one wants to solve. Chowdhury & Dasgupta (2003) proposed an algorithm that leads to the proper selection of the coefficients, based on knowledge of the resonance frequencies of the system.

Eq.(C.1) describe a problem with many degrees of freedom. In this thesis we want to solve the problem of a cantilever beam, which after discretization is reduced to such a many – degrees – of – freedom problem. However, our resulting system of ODE's is not in the form of Eq.(C.1). It is actually written as (see Ch. 4, Eq.(4.7.4))

$$\begin{bmatrix} \mathbf{0} & \mathbf{M} \\ \mathbf{I} & \mathbf{0} \end{bmatrix} \begin{bmatrix} \dot{\boldsymbol{\eta}} \\ \dot{\mathbf{u}} \end{bmatrix} + \begin{bmatrix} \mathbf{K} & \mathbf{C} \\ \mathbf{0} & -\mathbf{I} \end{bmatrix} \begin{bmatrix} \boldsymbol{\eta} \\ \mathbf{u} \end{bmatrix} = \begin{bmatrix} \mathbf{F} \\ \mathbf{0} \end{bmatrix} \tag{C.4}$$

as a system of first order in time ODE's. Note that terms analogous to $\ddot{\mathbf{x}}$ do not exist in this formulation. However, we find that the matrices **M**, **K** in Eq.(C.4) are equivalent to the classical mass and stiffness matrices in FEM formulation.

We shall continue to validate the algorithm of Chowdjury & Dasgupta (2003). that generates the Rayleigh damping matrix. We again consider a cantilever beam with length $L = 0.12\ m,$ bending stiffness $EI = 0.027\ Nm^2$ and linear mass distribution $m = 4.8\ kg/m^2$. To test the validity of the Rayleigh damping, we set the beam in free vibration with initial conditions. Knowing the first resonance frequency of the beam from Eq.(B.7), we setup the Rayleigh damping matrix so that it corresponds to $\zeta = 1$ to this frequency. The damping of another mode of the beam needs to be specified, so we set the damping at the second mode $\zeta = 1.5$. The number of collocation points is set to 20, while the order of accuracy of the finite difference scheme is set to 4. The free end deflection and velocity are shown in Fig. C2

.

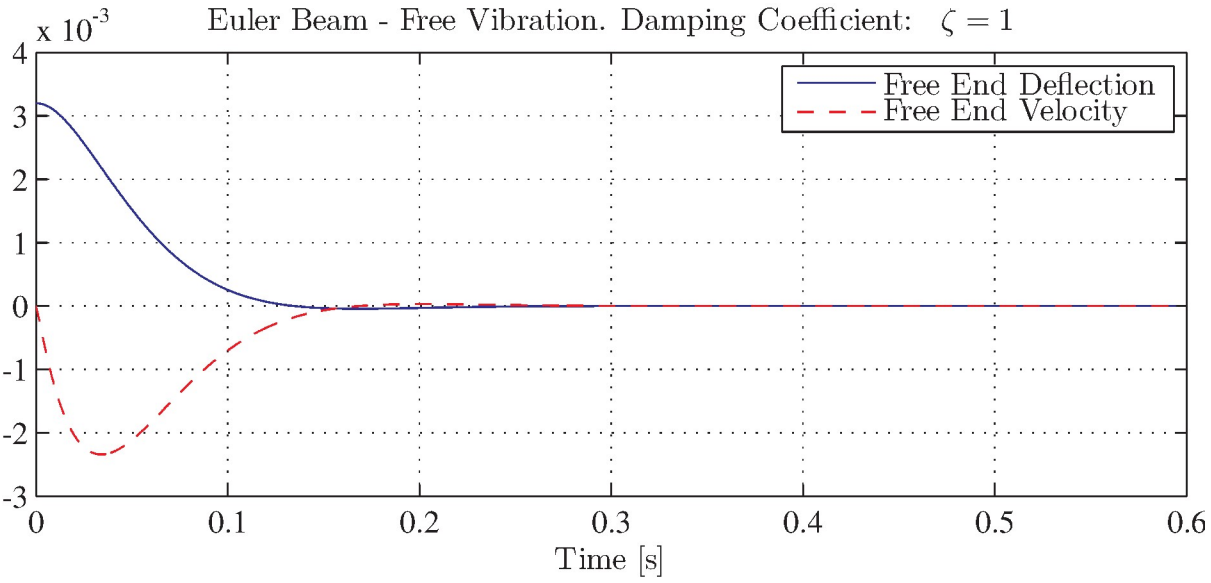

Figure C2: Free vibration of Euler – Bernoulli beam.

We note that the free – end deflection and transverse velocity time history is not oscillatory, which is expected for the case of critical damping. The coefficients that generate the corresponding Rayleigh damping matrix are $a = 29.28, \beta = 0.0219$. Indeed, for the first resonance frequency of the beam, $\omega_1 = 18.313\ rad/s$, we have

$$\frac{a}{2\omega_1} + \frac{\beta\omega_1}{2} = \frac{29.28}{2\times 18.313} + \frac{0.0219\times 18.313}{2} = 1 \qquad \text{(C.5)}$$